Quantum information with superconducting circuits

Benjamin Huard

To cite this version:

Benjamin Huard. Quantum information with superconducting circuits. Mesoscopic Systems and Quantum Hall Effect [cond-mat.mes-hall]. Ecole Normale Supérieure de Paris - ENS Paris, 2014. tel-01011096

HAL Id: tel-01011096

https://theses.hal.science/tel-01011096v1

Submitted on 26 Jun 2014

Département de Physique
École Normale Supérieure

Mémoire d'habilitation à diriger des recherches

Benjamin Huard

Circuits supraconducteurs pour l'information quantique

---

qui sera défendue le 16 juin 2014
devant le jury composé de :

M.	**Olivier Buisson**	Rapporteur
M.	**David DiVincenzo**	Rapporteur
M.	**Jean-Michel Raimond**	Examinateur
M.	**Jakob Reichel**	Examinateur
M.	**Andreas Wallraff**	Rapporteur

Acknowledgements

I would like to thank here all the people I had the luck to interact with since I'm a physicist and who contributed directly or not to the work presented in this manuscript. I have fond memories of my time in the Quantronics group at Saclay, where it was a great pleasure to work everyday with such a talented, friendly and upright set of people. My advisor, Hugues Pothier, and the rest of the group are a constant source of inspiration for any scientist, and I cannot thank them enough for welcoming me in their group at the beginning of my academic life. I'd like to thank the quantronics group for their continuing support and fruitful interactions. After my PhD work on mesoscopic transport with metals and superconductors, David Goldhaber-Gordon offered me to start a new project on graphene at Stanford University, which had very recently been successfully fabricated, and I thank him. The two years I've been at Stanford would not have been the same without the inventive and hard working students and postdocs I've had the luck to work with. I'd like to especially thank Nimrod Stander for his friendly and competent team work during those two years and Joey Sulpizio for the time we've spent together discussing all sorts of ideas and projects.

In late 2007, I learned that Michel Devoret was going to start a new lab in Paris and would be able to recruit a young physicist to work with him. This was extremely attractive to me for three reasons. First, Michel had left Saclay for Yale right before my PhD studies started, so that I did not know him but had heard from all sources what an outstanding physicist he is. Second, during my time at Saclay, there was a charming melody of superconducting circuits in the air, but I never had the opportunity to dig into it. And finally, after spending two years working on graphene transport, where I was thrilled to demonstrate Klein tunneling but frustrated by the irreproducibility in the fabrication, I wanted to work on physical systems with a better level of control. I was very lucky to start our lab at Ecole Normale Supérieure of Paris with Michel in 2008. We quickly became friend and I cannot quantify how much he brought me on scientific and personal levels. I want to thank him for all the friendship, support, opportunities and enlightenment he provided me since that year. Besides, our collaboration allowed me to perform something very unusual in France for a young researcher: starting a lab from scratch with good funding resources. I'm glad we can keep strong links now that he is back at Yale full-time.

I'd like to thank also the young physicists I've had the great luck to work with in Paris, and who made our experiments possible. Let us proceed by order of arrival in the group. François Nguyen, our first post-doc, spent a year ordering and installing lab equipments, and we've appreciated his smart choices ever since. I want to especially thank Nicolas Roch for the few years we've spent together in the lab. He managed to accelerate the fabrication of our first dilution refrigerator, which was no small feat, contributed immensely to the startup of the lab and brought a lot of dynamism and good spirit to the team. His enthusiasm for science was communicative and it was great to work with him. Emmanuel Flurin and Philippe Campagne-Ibarcq are our first two PhD students and they are both outstanding. Emmanuel is a complete physicist, with terrific insight and broad physics culture. It is a rare opportunity to work with such a bright student in all aspects of experimental and theoretical research. Philippe is extremely motivated and managed experimental feats that few could have performed. He is very fast and hard working, but also a generous, fun and unique character. I want to thank both of them for giving such a great initial impulse to our team. In 2011, François Mallet joined us as a permanent member and I'd like to thank him for so smoothly integrating the group. He has quickly embraced all the subjects we were working on and I'm glad we have the chance to work together now. I also want to thank Jean-Damien Pillet who performed a challenging fabrication of devices and shared his love of toy models to understand the behavior of these devices. Landry Bretheau joined us as a post-doc last year and I want to thank him for his friendly and talkative character. It is very refreshing to work with someone who never hides what he thinks and makes no compromise in a scientific discussion. We all appreciate his communicative love of science and his efficiency in exploring an experiment in depth, both theoretically and experimentally. We were also very fortunate to host Vladimir Manucharyan for a few months before he started his own lab at the Joint Quantum Institute. I'd like to thank him for the enlightening discussions we had continuously and for his friendship. Danijela Markovic joined the group earlier this year. She's been great to work with, highly motivated and I can't wait for the amazing experiments we'll perform together. Thanks also to all the students who spent a few months working with us over the years.

Starting an experimental lab is a time consuming task, and it was fantastic to get the help of many people at Ecole Normale Supérieure. Pascal Morfin helped us with all the installation of the lab and with the design of the pieces in the fridge together with Jack Olejnik. David Darson helped us choose and program the FGPA board used in the quantum feedback experiment, which would not have been possible without him. Jean-Charles Dumont helped us write our interfacing program. Didier Courtiade and his team managed close to impossible installations of the dilution fridges hanging from the ceiling and drilled huge holes in the walls among other crucial services and advices. I want to thank Anne Matignon, Fabienne Renia and Annie Sfez for dealing with the huge number of administrative tasks we face. Thanks also to Michael Rosticher and the rest of people working in the clean room facilities at Salle Blanche Paris Centre for their dedication to making the clean room work. I want also to thank the directors of Laboratoire Pierre Aigrain, Claude Delalande and Jean-Marc Berroir, but also the directors of the Physics depart-

ment, Jean-Michel Raimond and Werner Krauth for their strong support. Thanks also to the electrician team, electronics team, machine shop people, design engineers, computer and network services and all the other technical services for their tremendous help during these last years. It is great to work in the ENS environment and I'm very fortunate to interact with many physicists at various stages of their careers. Among them, I'd like to especially thank Takis Kontos for his friendly support and for sharing with us many ideas, instruments and RF components. I enjoyed a lot interacting with his students, and I'd like to especially thank Matthieu Delbecq, Jérémie Viennot and Matthieu Dartiailh. Thanks also to Aleksandra Walczak for sharing the organization of the Physics colloquium with me with such a great efficiency and good will.

I'd like to thank my close collaborators outside of ENS for their friendship and stimulating discussions. The Quantic Team with Mazyar Mirrahimi and Pierre Rouchon is a great environment to do research and I'm delighted we can work together. Thanks also to Alexia Auffèves, with whom I'm very happy to explore the emerging field of thermodynamics of quantum information. Thanks to the Yale groups of Michel Devoret and Rob Schoelkopf for welcoming me during a few months back in 2009, I particularly enjoyed my time there working with Flavius Schakert on a daily basis. I'd like also to thank Patrick Pari, Philippe Forget and Matthieu de Combarieu for their help in building our first dilution refrigerator. Finally, I'd like to thank the committee members for nicely accepting this position, and for their help with the manuscript.

The work presented in this manuscript was supported by the Emergences program of Ville de Paris, the Agence Nationale pour la Recherche, CNRS, Ecole Normale Supérieure, College de France, Paris Science Lettres and the Direction Générale de l'Armement.

And as a last word, thanks to Karin and Bethsabée for sharing their lives with a physicist.

Introduction

Applications of quantum mechanics can now be found everywhere. Computers, cell phones and light emitting diodes would not be there without the quantum description of solids. Internet and its fiber optics communications, DVDs and eye surgery rely on laser physics. Metrology and the Global Positioning System (GPS) depend on atomic clocks. With so many applications already, it may seem surprising that quantum mechanics still appears counterintuitive to many. Arguably, this may be due to a missing convenient language, and it seems to me that the current perspective of quantum information makes it much clearer. We are the fortunate witnesses and actors of the second wave of applications of quantum mechanics, which directly benefits from this new point of view. Several physical systems are indeed good candidates to encode and manipulate quantum information directly. Trapped ions, superconducting circuits, atoms, photons, spins, mechanical resonators, quantum dots and other systems all currently face the same challenge: their coherence time needs to be extended, in particular by error correction, for applications to appear. Several hundreds of groups worldwide are currently tackling these issues. The quantum machines based on these systems are still to be found, and it sure is hard to predict what will come out of them. But the already envisioned quantum computers, communications and simulators are certainly fascinating enough to pursue this enterprise.

In this manuscript, I present my contribution to the rise of superconducting circuits as the basis of quantum information systems. The macroscopic variables of electrical circuits, such as voltages and currents, obey quantum mechanics as long as they are protected enough from their environment. Since the first qubits based on a superconducting circuit were realized 15 years ago [1], their coherence time has already increased by 5 orders of magnitude [2] thanks to a better control of the electromagnetic environment of the Josephson junctions. We have performed experiments on these remarkable systems, which illustrate some of the most non-classical aspects of quantum information.

Quantum information differs from classical information by the purification postulate only [3], which states that the ignorance about a part is always compatible with the maximal knowledge of the whole. Several consequences of this postulate contradict classical wisdom and are worth exploring.

- Quantum variables fluctuate even at zero temperature. These zero point fluctuations imply lower bounds on the noise added by a detector. In chapter 1, we explore the quantum limits on amplification for propagating microwave signals, and show a concrete superconducting circuit, the Josephson mixer, able to reach this limit.

- Contrarily to classical information, quantum information can be stored in a spatially delocalized manner thanks to entanglement. In chapter 2, we demonstrate the first circuit able to entangle two propagating microwave modes at different frequencies and on separate transmission lines. We also present a device able to store a microwave field that is entangled with a propagating one.

- Measurement of a quantum system results in an inherent back action, with no classical equivalent. In chapter 3, we present how to correct for decoherence by measurement feedback on a superconducting qubit, in order to stabilize a desired quantum trajectory. This experiment makes clear the central role of measurement back action in quantum feedback, and thus in quantum error correction.

- Weak measurements provide partial information on a system. Because quantum measurement have an inherent back action, one needs to modify the classical Bayes rule predicting the probability of finding a given outcome assuming some outcome in the future. In chapter 4, we show an experiment where the fluorescence emitted by a qubit is recorded in time, which can be viewed as a weak measurement of the qubit. The influence of past and future information is explored.

Contents

1 Amplifiers for microwave quantum optics 9
- 1.1 Linear amplifiers . . . 9
  - 1.1.1 Scattering relations . . . 10
  - 1.1.2 Quantum limit on linear amplification . . . 10
- 1.2 Microwave amplifiers based on superconducting circuits . . . 13
  - 1.2.1 Degenerate amplifiers . . . 15
  - 1.2.2 Non-degenerate amplifiers . . . 15
  - 1.2.3 Nonlinear amplifiers . . . 15
- 1.3 Josephson mixer . . . 16
  - 1.3.1 Josephson ring . . . 16
  - 1.3.2 Coupling the ring to resonators . . . 17
- 1.4 Characteristics of the Josephson mixer as an amplifier . . . 19
  - 1.4.1 Gain vs bandwidth tradeoff . . . 19
  - 1.4.2 Participation ratio and design guidelines . . . 21
  - 1.4.3 Dynamical range . . . 22
  - 1.4.4 Flux tunability . . . 23
  - 1.4.5 How close to the quantum limit is it? . . . 24

2 Generating entanglement between microwave fields 25
- 2.1 Josephson mixer as an entanglement detector . . . 26
  - 2.1.1 Destructing coherent fields with a Josephson mixer . . . 26
  - 2.1.2 Entanglement witness . . . 27
- 2.2 Quantum node for entanglement and storage of microwave radiation . . . 30
  - 2.2.1 Time control of the coupling to a cavity . . . 30
  - 2.2.2 Storage and retrieval . . . 34
  - 2.2.3 Entanglement between the node and a communication channel . . . 35

3 Controlling a quantum system by feedback 37
- 3.1 Stabilizing a quantum trajectory by measurement feedback . . . 38
  - 3.1.1 Experimental constraints . . . 38

3.1.2 Cooling down a qubit by measurement based feedback 39
3.1.3 Stabilizing Rabi and Ramsey oscillations 39
3.2 Autonomous feedback 42
3.3 What's next? 43

4 Quantum measurement with past and future information 44
4.1 Superconducting circuits: a testbed for quantum measurement theory . . . 45
4.2 Fluorescence of a superconducting qubit 46
4.3 Past and future information 47
4.3.1 Past information 47
4.3.2 Future information 48
4.3.3 Past and future information 49

A Some results on linear amplifiers 65
A.1 Representing mode states 65
A.2 Quantum limit 68
A.2.1 Noise added on mode quadratures 68
A.2.2 Degradation of the signal to noise ratio 68
A.2.3 Quantifying the degradation of the signal to noise ratio in practice . 70
A.3 Quantifying the degradation of the signal to noise ratio in practice 70
A.4 Reflection coefficient on the Josephson mixer 72

Chapter 1

Amplifiers for microwave quantum optics

The decoherence of a quantum system results from the measurements performed by its environment [4]. In most experiments so far, only a tiny fraction of these measurements produce outcomes that are accessible to the observer. If the observer is able to extract more information than the rest of the environment, it becomes possible to record the evolution of a quantum system on a single realization and not only averaged traces. Many quantum systems couple well to microwave signals [5, 6, 7, 2], and can therefore be measured using microwave modes as a probe. Yet, several orders of magnitude divide the tiny power of quantum microwave signals and the detection threshold of usual measuring apparatus. Linear amplifiers are used to fill that gap.

In the last decade, the community of superconducting circuits has provided a strong push towards improving the efficiency of microwave amplifiers, so that most of the information extracted on these quantum systems can now be recorded. In this section, we present the limitations imposed by quantum mechanics on the efficiency of linear amplifiers. Then, we will show how we managed to reach up to 80% efficiency with concrete circuits.

1.1 Linear amplifiers

Propagating microwaves on transmission lines are described as modes of finite bandwidth $\Delta\omega_a$ [8]. Let us consider a mode centered on frequency ω_a which is described by a ladder operator $\hat{a}_{in}$. The mode quadratures[1] are defined as

$$\hat{X}_{a_{in}} = \mathrm{Re}(\hat{a}_{in}) = \frac{\hat{a}_{in} + \hat{a}_{in}^\dagger}{2} \text{ and } \hat{Y}_{a_{in}} = \hat{X}_{-ia_{in}} = \mathrm{Im}(\hat{a}_{in}) = \frac{\hat{a}_{in} - \hat{a}_{in}^\dagger}{2i}. \tag{1.1}$$

---

[1] Many notations and definitions can be found in the literature, where the quadratures can be defined as $\sqrt{2}$ or 2 times our definition. We use the notations X and Y in order to avoid confusion with distributions P, W and Q. In the literature, X is often called P or I and Y is often called P or Q.

1.1.1 Scattering relations

It is tempting to define a linear amplifier of power gain G as an amplifier that transforms $\hat{a}_{in}$ into an amplified version of another mode operator $\hat{a}_{out}$ such as $\hat{a}_{out} = \sqrt{G}\hat{a}_{in}$. However, this equality does not hold except for $G = 1$ as can be seen from the commutation relations

$$[\hat{a}_{out}, \hat{a}^{\dagger}_{out}] = [\hat{a}_{in}, \hat{a}^{\dagger}_{in}] = 1. \tag{1.2}$$

An extra mode operator $\hat{b}_{in}$, called the idler, which commutes with $\hat{a}_{in}$, is then introduced so that the following relation holds for all gains G and input state:

$$\hat{a}_{out} = \sqrt{G}\hat{a}_{in} + \sqrt{G-1}\hat{b}^{\dagger}_{in}. \tag{1.3}$$

With this operating principle[2], the commutation relations (1.2) are valid for all gain G. Linear amplifiers come in two main flavors depending on the choice of $\hat{b}_{in}$.

- **Phase-preserving amplifiers**

  This kind of amplifiers correspond to an identical gain $\sqrt{G}$ on both quadratures

  $$\langle\hat{a}_{out}\rangle = \sqrt{G}\langle\hat{a}_{in}\rangle. \tag{1.4}$$

  It is the case when $\hat{b}_{in}$ verifies $\langle\hat{b}_{in}\rangle = 0$ and $[\hat{b}_{in}, \hat{a}^{\dagger}_{in}] = 0$.

- **Phase-sensitive amplifiers**

  This kind of device amplify one quadrature but attenuate the other. The output mode hence obeys

  $$\hat{a}_{out} = \sqrt{G_s}\hat{X}_{e^{-i\varphi}a_{in}} + \frac{i}{\sqrt{G_s}}\hat{Y}_{e^{-i\varphi}a_{in}}, \tag{1.5}$$

  for a certain phase φ. For instance, if $\varphi = 0$, it corresponds to $\hat{b}_{in} = \hat{a}_{in}$. In this case, $\sqrt{G_s} = \sqrt{G} + \sqrt{G-1}$.

1.1.2 Quantum limit on linear amplification

In 1962, Haus and Mullen [10] discovered the minimal noise that a linear amplifier has to add, and this limit was later reformulated by Caves [11] in 1982. To put it simply, the extra mode necessary to phase-preserving amplifiers adds the equivalent of half a photon of noise at the input in the case of large gains. On the contrary, phase-sensitive amplifiers

---

[2] It is possible to perform noiseless phase-preserving amplification if one is willing to post-select the experiments on a control observable [9]. In this case, a coherent state $|\gamma\rangle$ is transformed into $|\sqrt{G}\gamma\rangle$ each time a control observable is measured in a particular state. The improvement in signal to noise ratio is then balanced by a lower success rate. Up to now, the implementations of this kind of amplifiers use photodetectors as a way to measure the presence of a control photon. It would be very interesting to build the equivalent in the microwave domain, where photodetectors are an ongoing project for the community.

do not have to add any noise. This quantum limit is formally expressed by a lower bound on the sum of both output quadrature variances[3]

$$\frac{\langle \Delta X^2_{a_{out}} \rangle + \langle \Delta Y^2_{a_{out}} \rangle}{G} \underset{G\to\infty}{\gtrsim} \langle \Delta X^2_{a_{in}} \rangle + \langle \Delta Y^2_{a_{in}} \rangle + \frac{1}{2} \tag{1.7}$$

for a phase-preserving amplifier. The minimum is reached for $\hat{b}_{in}$ in the vacuum.

This half quantum of added noise does not reveal properly the limitations of linear amplifiers as measurement apparatuses. In fact, both kinds of amplifiers can be non-information degrading when measuring the physical quantity they are matched to. In order to illustrate this point, let us consider the case of homodyne and heterodyne detection.

Homodyne measurement

Homodyne measurement consists in measuring only one quadrature $X_{e^{i\theta}a_{in}}$ of the field a_{in}. In the microwave domain, it can be done by first mixing the field a_{out} with a powerful tone at frequency ω_a and phase θ. Then, by measuring the average value of the output voltage using a proper low-pass filter (typically averaged over $2\pi/\Delta\omega_a$), one gets an outcome proportional to $X_{e^{i\theta}a_{in}}$. We then define the signal to noise ratio of a homodyne measurement as SNR $\equiv \frac{\langle X\rangle^2}{\mathrm{Var}(X)}$. As we already noticed, a phase sensitive amplifier is perfectly suited to homodyne detection as it does not add any noise while amplifying the homodyne signal. For a phase preserving amplifier, one finds in the large gain limit that (see Appendix)

$$\mathrm{SNR}_{out} = \frac{\mathrm{SNR}_{in}}{1 + \frac{\langle \Delta X^2_{b_{in}} \rangle}{\langle \Delta X^2_{a_{in}} \rangle}}. \tag{1.8}$$

The least possible degradation would then be obtained for a squeezed idler mode, but perfect efficiency is reached only asymptotically on the squeezing parameter of idler.

Heterodyne measurement

Heterodyne measurement consists in measuring simultaneously both quadratures $X_{a_{in}}$ and $Y_{a_{in}}$. It can be done by first mixing the field a_{out} with a powerful tone at frequency $\omega_a + \omega_h$, where ω_h is larger than the propagating mode bandwidth $\Delta\omega_a$ but smaller than the bandwidth of the detector. It is then possible to record the resulting signal and numerically demodulate it at frequency ω_h in order to extract its quadratures $X_{a_{in}}$ and $Y_{a_{in}}$. A phase sensitive amplifier is useless for that kind of measurement since it attenuates one quadrature.

---

[3]

$$\langle \Delta X^2_{a_{out}} \rangle \equiv \left\langle \left(\frac{\hat{a}_{out} + \hat{a}^\dagger_{out}}{2} \right)^2 \right\rangle - \left\langle \frac{\hat{a}_{out} + \hat{a}^\dagger_{out}}{2} \right\rangle^2 . \tag{1.6}$$

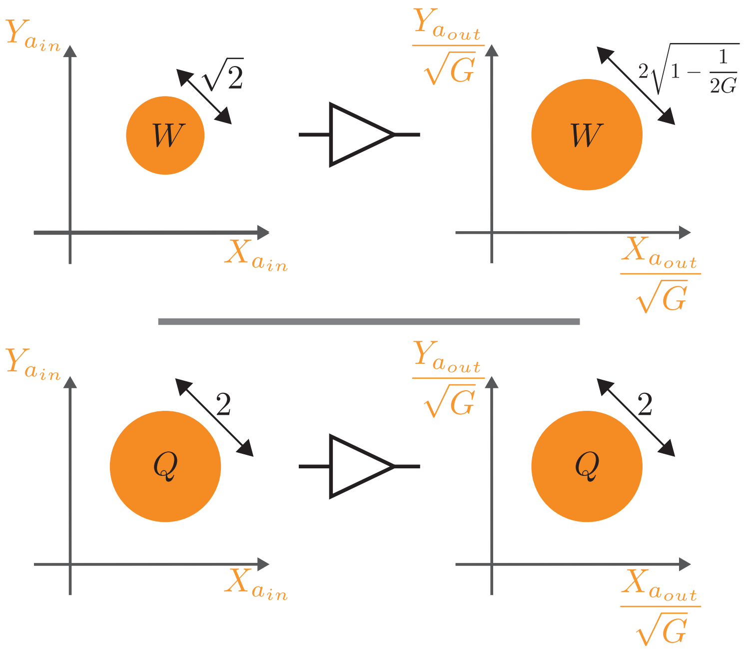

Figure 1.1: In the quadrature phase-space, a disk represents the area where the distribution is larger than its maximum divided by e. Top row: Wigner functions of a coherent state before (left) and after (right) amplification by a quantum-limited phase-preserving amplifier with the vacuum state at the idler input. Bottom row: Husumi Q functions of the same states. The signal to noise ratio is degraded for homodyne measurement (SNR related to the Wigner function) but not for heterodyne measurement (SNR related to the Q function).

In order to understand the degradation in signal to noise ratio for a heterodyne measurement, let us consider the distribution probability $\mathcal{P}(x, y)$ to measure both quadratures in x and y. This distribution is in fact the Husumi Q distribution (see Fig. A.3) [12, 13, 14, 15].

$$\mathcal{P}(x, y) = Q(x + iy). \tag{1.9}$$

The proper signal to noise ratio to consider is therefore $\mathrm{SNR} \equiv \frac{|\langle X+iY\rangle|^2}{\mathrm{Var}_Q}$, where Var_Q is the variance of the Q distribution. If one uses a phase-preserving amplifier with the idler in the unsqueezed vacuum state (Fig. 1.1), the variance of the Husumi Q function $\mathrm{Var}_Q(a_{out}) = \int_{\mathbf{C}} Q_{out}(\alpha)\Delta\alpha^2 \mathrm{d}\alpha$ at the output is

$$\mathrm{Var}_Q(a_{out}) = G\mathrm{Var}_Q(a_{in}) + (G-1)\left(\mathrm{Var}_Q(b_{in}) - 1\right) = G\mathrm{Var}_Q(a_{in}). \tag{1.10}$$

Therefore, the noise of heterodyne measurement scales as the signal itself, by the gain of the amplifier. It is thus physically possible not to degrade the signal to noise ratio of a heterodyne measurement using a phase preserving amplifier. This property translates quantitatively in the possibility to keep a qubit in a pure state during a weak heterodyne measurement of the field in a circuit-QED architecture, as was shown in Ref. [16] last year.

1.2 Microwave amplifiers based on superconducting circuits

In this section, we briefly describe several implementations of linear microwave amplifiers operating close to the quantum limit. One of them, the Josephson mixer, is a multipurpose tool for microwave quantum optics and will be described in detail. When referring to microwave frequencies, we actually mean the 2 to 20 GHz range. Within this range, the vacuum state can be prepared by simply cooling down the fields at dilution refrigerator temperatures ($\hbar\omega/k_B > 100\text{ mK} \gg T_{\text{dil}}$) and the wavelength is larger than 10 mm, which makes the wave propagation more tolerant to small imperfections in the measurement setup and gives access to high precision apparatus unavailable at larger frequencies.

Superconducting circuits offer an easy way to perform quantum operations on microwave fields. Indeed, they are nearly lossless conductors[4], have a gap larger than microwave photon energies and their tunnel junctions — the Josephson junctions — are nonlinear element. With the recent development of circuit-Quantum ElectroDynamics (circuit-QED), where superconducting circuits are coupled to microwave resonators, the need for quantum limited microwave amplifiers has been pressing. Building up on the earlier efforts of Yurke and coworkers [20] in the late 1980's, the community has developed several kinds of low noise parametric amplifiers based on Josephson circuits.

Caves and coworkers have shown recently that any phase-preserving linear amplifier behaves like a parametric amplifier with an idler mode in a given state [21]. A parametric amplifier couples the signal mode $\hat{a}_{in}$ to an idler mode $\hat{b}_{in}$ via a pump $\hat{p}$ at frequency $\omega_p = \omega_a + \omega_b$. The coupling term in the Hamiltonian reads $i\hbar\chi_{abp}(\hat{a}^\dagger\hat{b}^\dagger\hat{p} - \hat{a}\hat{b}\hat{p}^\dagger)$. In the stiff pump regime, $\hat{p}$ can be replaced by a scalar number so that, in the interaction picture, one gets the parametric down-conversion Hamiltonian [22]

$$H_{\text{pd}} = i\hbar\chi_{ab}(\hat{a}^\dagger\hat{b}^\dagger e^{i\varphi} - \hat{a}\hat{b}e^{-i\varphi}), \tag{1.11}$$

where $\chi_{ab}e^{i\varphi} = \chi_{abp}\langle\hat{p}e^{i\omega_p t}\rangle$. This Hamiltonian can be integrated during the interaction time τ_i in order to give the evolution operator, also called two-mode squeezing operator

$$S = e^{re^{i\varphi}\hat{a}^\dagger\hat{b}^\dagger - re^{-i\varphi}\hat{a}\hat{b}}, \tag{1.12}$$

where $re^{i\varphi} = \chi_{ab}\tau_i e^{i\varphi}$ is called the complex squeezing parameter. The scattering relations

---

[4] At nonzero frequency, a superconductor has an inductive behavior. An oscillating current hence induces an electric field which accelerates quasiparticles, a source of power dissipation [17, 18]. Yet, in most circuits, this dissipation is negligible compared to other parasitic sources of loss such as defects in the dielectric medium [19].

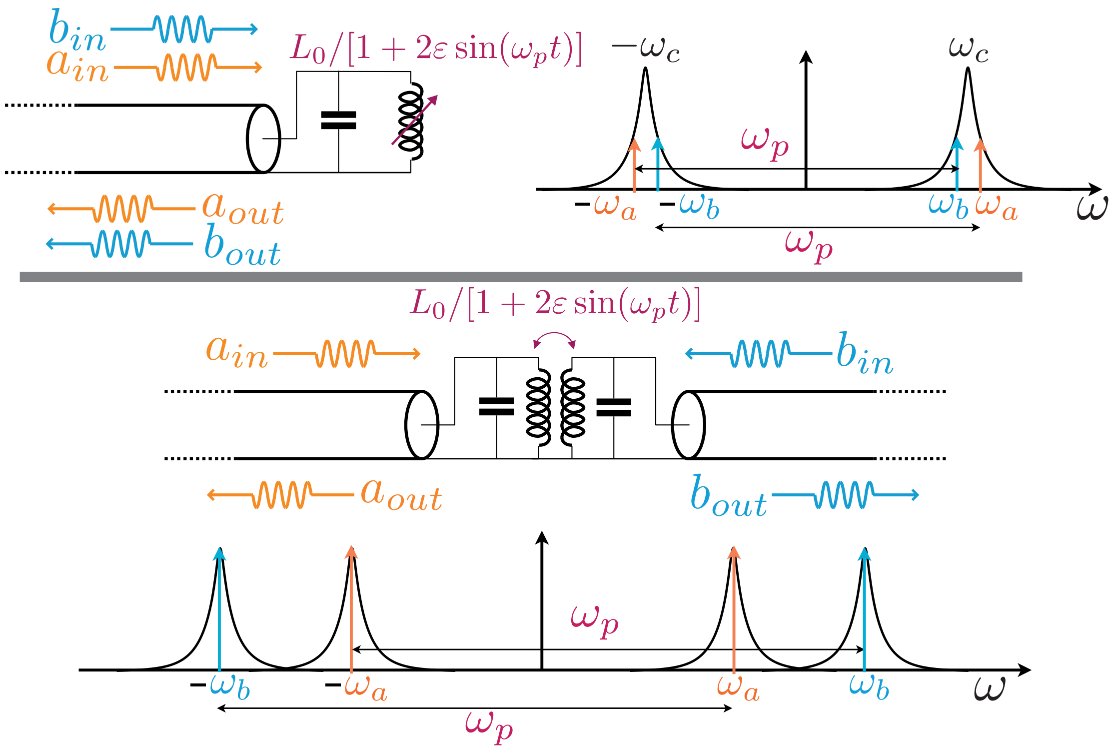

Figure 1.2: Top: Degenerate amplifier. The pumped SQUID array can be modeled as an inductance oscillating at frequency $\omega_p = \omega_a + \omega_b$. In the degenerate case, both signal a and idler b modes share a single resonance bandwidth. Besides, they evolve on the same physical transmission line. Bottom: Non-degenerate amplifier. In this case, signal and idler modes are localized on different resonators. They can be non-degenerate in space and/or frequency, with arbitrarily separated mode frequencies.

of a non-degenerate amplifier hence read as Eq. (1.3)

$$\begin{aligned} \hat{a}_{out} &= S^\dagger \hat{a}_{in} S = & \cosh(r)\hat{a}_{in} + e^{i\varphi_P}\sinh(r)\hat{b}^\dagger_{in} \\ \hat{b}^\dagger_{out} &= S^\dagger \hat{b}^\dagger_{in} S = & \cosh(r)\hat{b}^\dagger_{in} + e^{-i\varphi_P}\sinh(r)\hat{a}_{in} \end{aligned} . \tag{1.13}$$

Experimentally, several kinds of parametric amplifiers were implemented as discussed below. A possible distinction between them consists in the fact that signal and idler modes share a single resonator (degenerate) or not (non-degenerate) as detailed on Fig. 1.2.

1.2.1 Degenerate amplifiers

Josephson parametric amplifiers consist in a serial array of at least one SQUID contributing to the inductance of a superconducting LC resonator [20, 23, 24, 25, 26, 27]. In most realizations, the resonance mode is the fundamental mode of a $\lambda/4$ resonator terminated by the array of SQUIDs on one side and capacitively coupled to the input/output port on the other. Single Josephson junctions could be used instead of SQUIDs at the expense of frequency tunability. The Hamiltonian of the circuit is up to fourth order given by

$$H_{\mathrm{deg}} = \hbar\omega_c \hat{c}^\dagger \hat{c} + \hbar\chi \hat{c}^\dagger \hat{c}^\dagger \hat{c}\hat{c}. \tag{1.14}$$

Let us now define modes $\hat{a}$ and $\hat{b}$ with frequencies $\omega_a = \omega_c - \delta\omega$ and $\omega_b = \omega_c + \delta\omega$ so that the detuning $\delta\omega$ is smaller than the resonator bandwidth but larger than the bandwidth of modes $\hat{a}$ and $\hat{b}$. The amplifier operates by sending a pump microwave tone at ω_c. In this case, one indeed finds the phase-preserving scattering relations Eq. (1.13). It is also possible to realize a phase sensitive amplifier in the limit where $\delta\omega = 0$, i.e. $\hat{a} = \hat{b}$. There, the scattering relations Eq. (1.5) are verified.

Note that degenerate microwave amplifiers can be realized differently than Josephson parametric amplifier. For instance, one may use a weak link instead of the SQUID [28] or even the nonlinearities of the superconducting film itself [29, 30]. It is also possible to use a Josephson Parametric amplifier by pumping its flux at twice the signal frequency [31]. A different class of amplifiers based on SQUIDs amplify the oscillating magnetic flux threading them [32, 33, 34, 35] and were used at high-frequencies already in the late 1990's.

1.2.2 Non-degenerate amplifiers

Non-degenerate amplifiers correspond to the case where modes $\hat{a}$ and $\hat{b}$ do not share a single resonator. They avoid any overlap in space and/or frequency. Such an amplifier based on superconducting circuits was first proposed and realized by Bergeal and coworkers in 2008 [36, 37]. It is called the Josephson mixer and based on a ring of four Josephson junctions coupling two resonators and a microwave pump tone. As we have shown in Ref. [38], its behavior can be modeled by the simplified circuit shown at the bottom of Fig. 1.2. We will describe this circuit in detail in the next section.

Let us note that another non-degenerate parametric amplifier was proposed by Kamal and coworkers in 2009 [39]. It is based on a single junction or SQUID pumped by two tones.

1.2.3 Nonlinear amplifiers

There also exists superconducting circuits that amplify a signal in a non-linear way. They are well suited to amplify binary responses like in the measurement of a qubit state. They are based on the bifurcation of a nonlinear oscillator [40, 41, 42, 43, 44]. Close to threshold, a tiny variation of the signal can lead to the jump into a different state of the oscillator.

1.3 Josephson mixer

1.3.1 Josephson ring

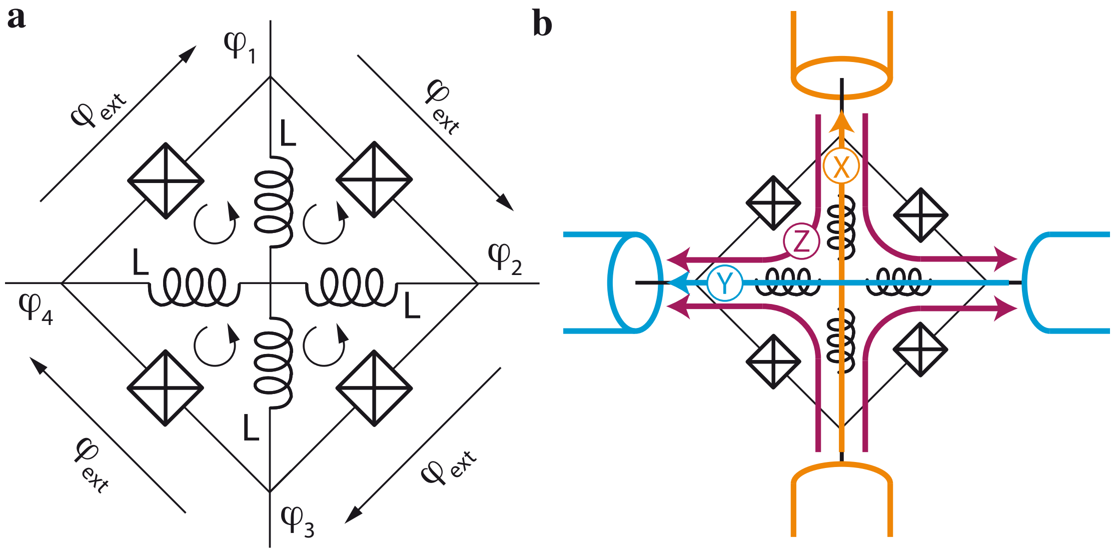

Figure 1.3: **a)** Device schematic: four linear inductances L cross-link a ring of four Josephson junctions. Each sub-loop is biased by a magnetic flux $\varphi_{ext}\varphi_0$. For $L < L_J^0/4$, the current through the inductances is zero and the external flux phase-biases the junctions to φ_{ext} on average. **b**. The device is embedded at the intersection of four transmission lines and couples to spatial modes X, Y and Z represented as arrows.

First, let us describe the core of the mixer which is a ring of four identical Josephson junctions. Actually, as we have shown in Ref. [45], it is more convenient to consider additional linear inductances cross-linking the ring like the pokes of a wheel as shown in Fig. 1.3. One can then define the normal mode[5] phase degrees of freedom of the ring (see Fig. 1.3) by $\varphi_X = \varphi_1 - \varphi_3$, $\varphi_Y = \varphi_4 - \varphi_2$ and $\varphi_Z = \varphi_2 + \varphi_4 - \varphi_1 - \varphi_3$. The Hamiltonian of the ring then reads

$$\begin{aligned} H \;=\; & -4E_J \sin(\varphi_X)\sin(\varphi_Y)\sin(\varphi_Z)\sin(\varphi_{ext}) \\ & -4E_J \cos(\varphi_X)\cos(\varphi_Y)\cos(\varphi_Z)\cos(\varphi_{ext}) \;, \\ & +\tfrac{1}{2}E_L/2\left({\varphi_X}^2 + {\varphi_Y}^2 + {\varphi_Z}^2/2\right) \end{aligned} \tag{1.15}$$

---

[5] The four currents exiting the ring are related to the four node phases by an inductance matrix. Diagonalizing this matrix leads to finding the normal mode phase combinations.

which can be approximated for small variations by

$$\begin{array}{rcl} H & \approx & -\frac{1}{2}E_J\sin\left(\varphi_{ext}\right)\varphi_X\varphi_Y\varphi_Z \\ & & +\frac{1}{2}\left(E_L/2+E_J\cos\varphi_{ext}\right)\left({\varphi_X}^2+{\varphi_Y}^2\right)+\frac{1}{2}\left(E_L/4+E_J\cos\varphi_{ext}\right){\varphi_Z}^2 \end{array} . \tag{1.16}$$

Here, $E_L = {\varphi_0}^2/L$ is the energy associated with each of the inductances L, and $E_J = \varphi_0^2/L_J^0 = \varphi_0 I_0$ is the Josephson energy of each tunnel junction (I_0 being their critical current). We also define the reduced flux quantum $\varphi_0 = \hbar/2e$ and the dimensionless flux $\varphi_{ext} = \Phi_{ext}/4\varphi_0$ threading each of the nominally identical 4 loops of the device. The first term of the Hamiltonian is a pure 3-wave mixing term, while the two others are quadratic terms determining the effective inductance of modes X, Y and Z: $L_{X,Y,Z}^{-1} = {\varphi_0}^{-2}\partial^2 H/\partial\varphi_{X,Y,Z}^2$. The value $\varphi_{ext} = \pi/2$ maximizes the strength of the mixing term.

1.3.2 Coupling the ring to resonators

In order to use the 3-wave mixing term of the Josephson ring, one has to couple X, Y and Z to microwave modes $\hat{a}$, $\hat{b}$ and $\hat{p}$. This is done by connecting the ring to open microwave resonators as shown in Fig. 1.4. Several possible designs [37, 46, 47] can realize this coupling. One common feature of these circuits is the non-resonant behavior of the $\hat{p}$ mode, which will allow us to consider it as a classical variable (stiff pump regime). In these designs, X is proportional to a quadrature of $\hat{a}$ and so are related Y to $\hat{b}$ and Z to $\hat{p}$. For the geometry of Fig. 1.4, it can be shown that

$$\hat{X} = (\hat{a}+\hat{a}^\dagger)\frac{\omega_a^{res}L_a^{ring}}{\sqrt{Z_a h/e^2}}\sqrt{4\pi} \text{ and } \hat{Y} = (\hat{b}+\hat{b}^\dagger)\frac{\omega_b^{res}L_b^{ring}}{\sqrt{Z_b h/e^2}}\sqrt{4\pi}, \tag{1.17}$$

where Z_i is the characteristic impedance of mode i, L_i^{ring} is the effective inductance relating the current and flux of mode i and ω_i^{res} is the resonance frequency of mode i. The 3-wave mixing term can now be written in terms of the mode operators

$$H_{mix} = i\hbar\chi_{abp}(\hat{a}+\hat{a}^\dagger)(\hat{b}+\hat{b}^\dagger)(\hat{p}-\hat{p}^\dagger). \tag{1.18}$$

Two important cases can be distinguished by the rotating wave approximation depending on the pump frequency ω_p.

- **Sum mode:** if $\omega_p = \omega_a + \omega_b$, then the mixing Hamiltonian can be approximated to be $H_{mix} = i\hbar\chi_{abp}(\hat{a}^\dagger\hat{b}^\dagger\hat{p} - \hat{a}\hat{b}\hat{p}^\dagger)$, which we have shown above leads to the parametric-down conversion Hamiltonian (1.11)

  $$H_{\mathrm{pd}} = i\hbar\chi_{ab}(\hat{a}^\dagger\hat{b}^\dagger e^{i\varphi} - \hat{a}\hat{b}e^{-i\varphi}). \tag{1.19}$$

  This is therefore the phase-preserving parametric amplification regime. We have used this regime in order to perform near quantum limited amplification (see below), parametric oscillation and the generation and witnessing of entangled pairs of microwave radiation (section 2).

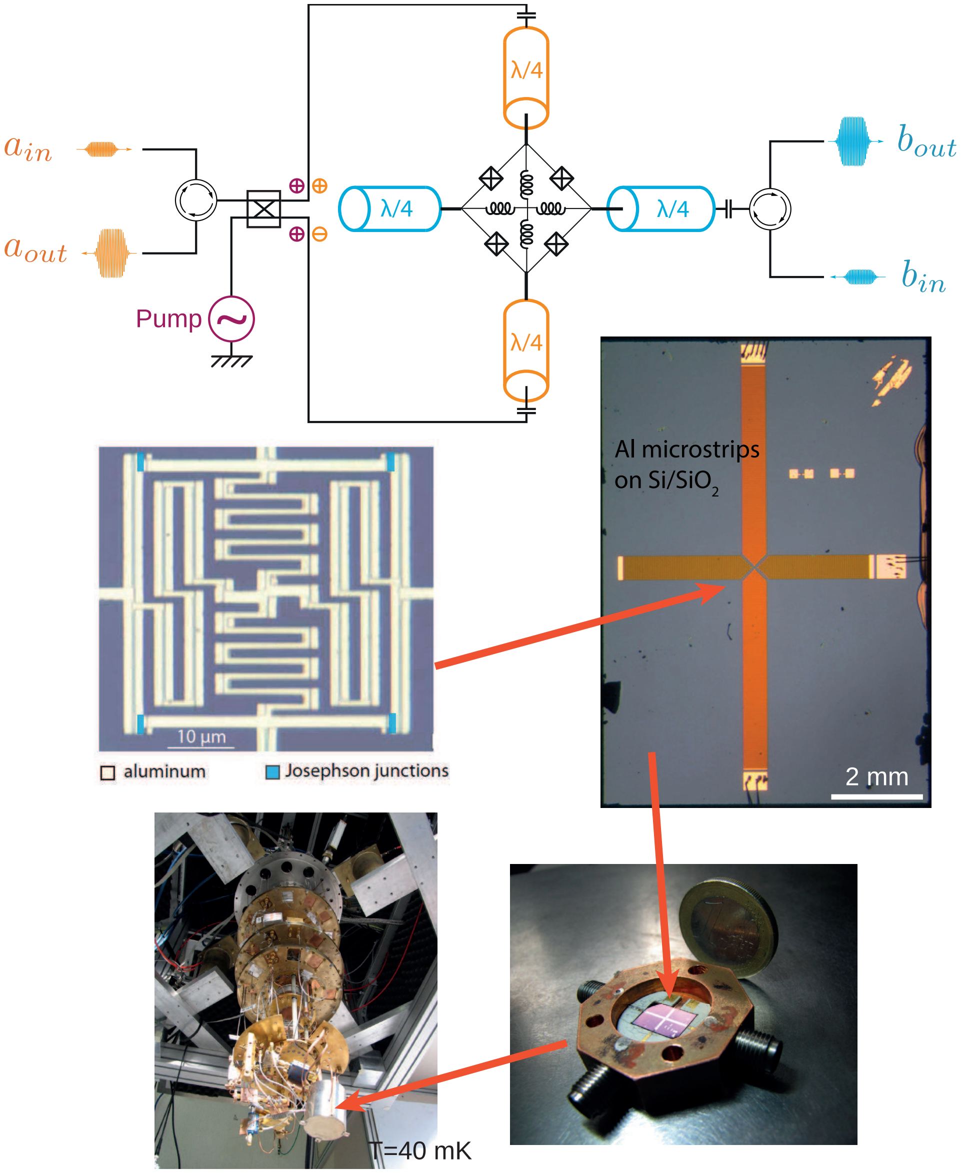

Figure 1.4: Top: Schematics of the Josephson mixer. The ring is placed at the crossing of two $\lambda/2$ resonators of frequency ω_a and ω_b. Mode b, whose quadrature is proportional to Y, is single ended and its input and output signals are spatially separated by a commercial circulator. Mode a, whose quadrature is proportional to X, is connected to a 180°-hybrid coupler so as to address the Z and X modes of the ring via two separate ports. The input and output signals on a are also separated by a circulator. Bottom: Physical implementation of the Josephson mixer corresponding to the one reported in Ref. [45]. The whole circuit is made in one step of electronic lithography followed by evaporation of Aluminum on an oxidized silicon chip. The Josephson junctions are artificially colored in blue on the picture. The resonators are made using microstrip geometry and the circuit is shielded and anchored at the base temperature of a dilution refrigerator.

- **Difference mode:** if $\omega_p = \omega_a - \omega_b$, then the mixing Hamiltonian can be approximated to be $H_{mix} = i\hbar\chi_{abp}(\hat{a}^\dagger\hat{b}\hat{p} - \hat{a}\hat{b}^\dagger\hat{p}^\dagger)$. This is the frequency conversion regime which has recently been explored experimentally in Ref. [48]. We have used this mode in order to realize a quantum memory for microwave signals as described in section 2.2.

1.4 Characteristics of the Josephson mixer as an amplifier

The performances of a phase preserving microwave amplifier are characterized by five parameters:

- the power gain G is the ratio of the output power to the input power.
- the dynamical bandwidth $\Delta\omega$ sets the scale of the shortest temporal features that can be amplified without distortion.
- the frequency tunability $\omega_{\mathrm{max}} - \omega_{\mathrm{min}}$ corresponds to the spectrum of continuous tones that can be amplified. Note that, slow varying parameters can be tuned so as to cover this full spectrum so that $\Delta\omega \leq \omega_{\mathrm{max}} - \omega_{\mathrm{min}}$.
- the efficiency η (equivalently added noise $\mathcal{A}$, noise temperature T_N or noise factor F as described in section A.3) describe by how much the amplifier misses the quantum limit.
- the compression point P_{1dB} gives the amount of input power beyond which the amplifier power gain decreases by 1 dB.

1.4.1 Gain vs bandwidth tradeoff

Resonators a and b are coupled to two transmission lines at a characteristic rate κ_a and κ_b. The reflection coefficient at the mixer input port then reads [36]

$$r_a = \frac{1 + C + i(\delta\omega_a + \delta\omega_b) - \delta\omega_a\delta\omega_b}{1 - C - i(\delta\omega_a - \delta\omega_b) + \delta\omega_a\delta\omega_b} \tag{1.20}$$

where the cooperativity is

$$C = \frac{4\chi_{abp}^2|p|^2}{\kappa_a\kappa_b}, \tag{1.21}$$

and $\delta\omega_{a,b}$ are dimensionless detunings between the probe frequency and the resonance frequency, which is shifted by the Kerr termsThe magnitude of this reflection coefficient for a typical device is shown in Fig. 1.5. The power gain G of the amplifier is defined by $|r_a|^2$ at resonance for small intra resonator fields. Hence, for $C < 1$ (below threshold)

$$G = \left(\frac{1 + C}{1 - C}\right)^2. \tag{1.22}$$

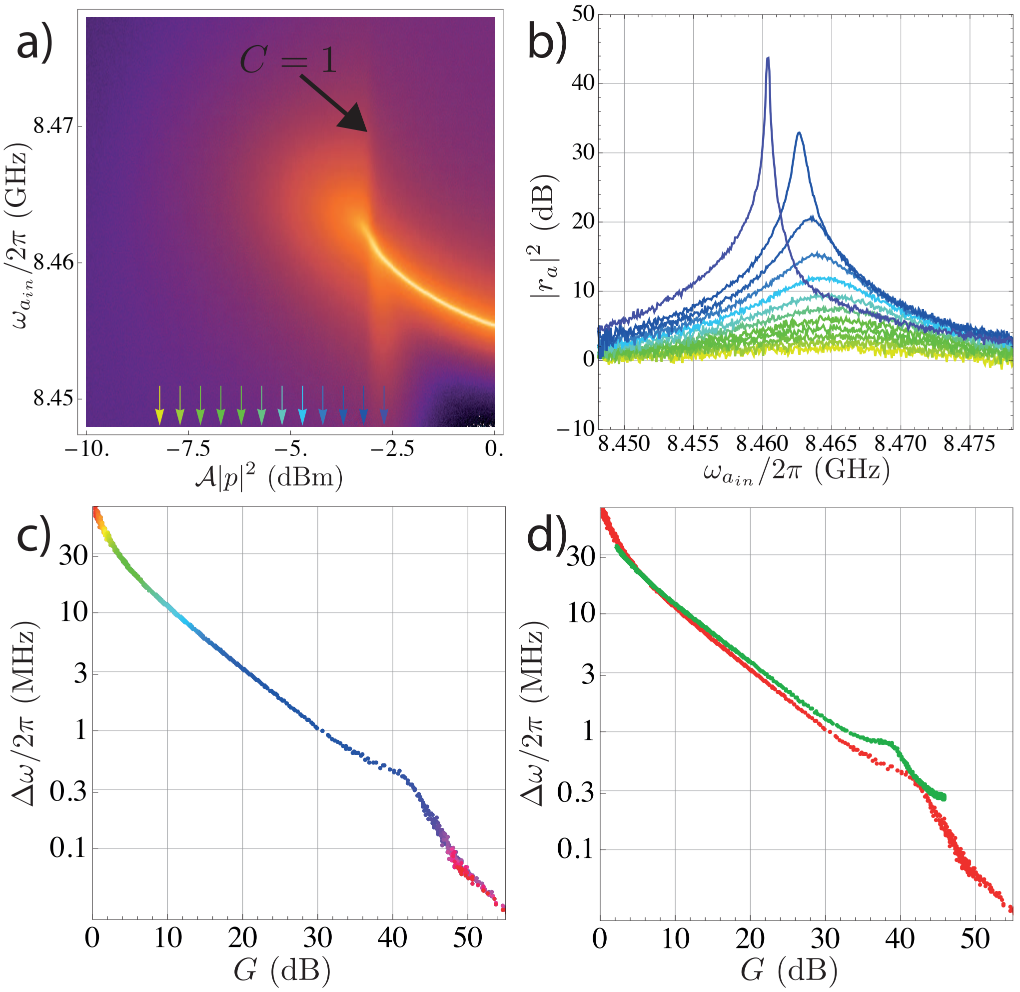

Figure 1.5: **a)** Magnitude of the reflection coefficient $|r_a|^2$ represented as a function of the pump power (measured at the level of the generator, with about $\mathcal{A}^{-1} \approx 60 - 70$ dB of power attenuation) and as a function of the input frequency $\omega_{a_{in}}$. The pump frequency is $\omega_p/2\pi = 14.071$ GHz. **b)** Cuts of the density plot in a) taken at pump powers indicated by the colored arrows. **c)** Bandwidth of the amplifier as a function of gain. The dot colors correspond to the pump powers pointed by color arrows in a). **d)** Same as c) for the red curve and similar curve for mode b plotted in green.

The bandwidth of the amplifier $\Delta\omega_a$, from which we define the input/output mode bandwidth, is defined by the frequency interval over which $|r_a|^2$ is larger than $G/2$.

$$|r_a(\delta\omega_a = -\delta\omega_b)|^2 \geq \frac{G}{2} \text{ for } |\delta\omega_a| \leq \frac{\Delta\omega_a}{2}. \tag{1.23}$$

For large gains, as we describe in Ref. [38],

$$\Delta\omega_a\sqrt{G} \approx 2\left(\frac{1}{\kappa_a} + \frac{1}{\kappa_b}\right)^{-1} \leq 2\text{min}(\kappa_a, \kappa_b). \tag{1.24}$$

Thus, we find that the bandwidth of the amplifier is limited by the smallest coupling rate between resonators and transmission lines. On Fig. 1.5, one can check how well this law is reproduced.

1.4.2 Participation ratio and design guidelines

From the above description, it seems that in order to maximize the bandwidth of the amplifier, one simply needs to maximize the coupling rate of the resonators to their transmission lines $\kappa_{a,b}$. Let us now see why these rates are limited.

An essential parameter of the amplifier is the participation ratio ζ of the Josephson junctions [49]. It quantifies the fraction of energy stored in the Josephson junctions compared to the total circuit energy. In case of the Josephson mixer, the participation ratios of the junctions to each resonator are (see supplementary material of Ref. [50])

$$\zeta_{a,b} = \frac{2}{|\tan(\varphi_{ext})|}\frac{1}{\omega_{a,b}}\left|\frac{\partial\omega_{a,b}}{\partial\varphi}\right|, \tag{1.25}$$

where φ is the phase difference across the junction and $\omega_{a,b}$ the resonator frequency of mode a (b) [51].

As was shown in Ref. [36], the cooperativity is related to the pump current I_p going into the pump mode by

$$C = \frac{\zeta_a Q_a \zeta_b Q_b}{\Xi}\frac{I_p}{I_0}, \tag{1.26}$$

where Ξ is a number of order 1, I_0 the critical current of the Josephson junctions and $Q_{a,b} = \omega_{a,b}/\kappa_{a,b}$ is the quality factor of resonator a (resp. b). In order for the amplifier to operate with a reasonable gain, one needs to reach $C \approx 1$ while ensuring the condition $I_p < I_0$. One then arrives at the important design criterion that limits the bandwidth of the mixer

$$\zeta_a Q_a \zeta_b Q_b > \Xi. \tag{1.27}$$

1.4.3 Dynamical range

Another characteristics of an amplifier is the dynamical range, expressed as the maximal power $P_{1\mathrm{dB}}$ one can provide at the input without losing more than 1 dB of gain. The dynamical range may be limited by pump depletion or by the Kerr terms shifting the resonance frequency of the resonators while the pump and signal are increased [46, 47]. The dynamical range of a typical amplifier is shown in Fig. 1.7b. A detailed study of dynamical range limitations in the case of degenerate parametric amplifiers can be found in Ref. [52].

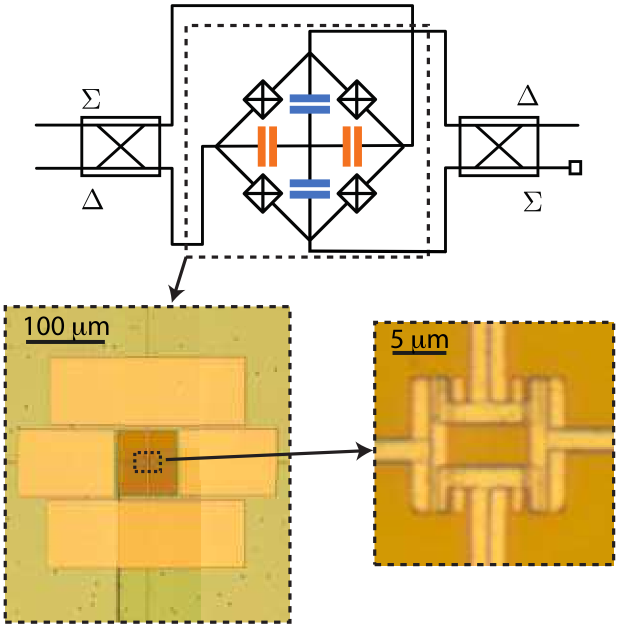

Figure 1.6: Top: Schematic of the experimental setup. Normal Modes are addressed in reflection through two 180^o hybrid couplers. Bottom: Optical microscope image of the device showing the capacitors (Al/SiN/Al) and the Josephson junction ring.

Given the various constraints on dynamical range and bandwidth, the optimal design for the Josephson mixer consists in maximizing the participation ratio by minimizing the inductance of the resonators. We have designed and measured such an amplifier, in which the resonators are made of the Josephson ring and lumped capacitors (Fig. 1.6). In this device, we have demonstrated a dynamical range of $P_{1\mathrm{dB}} = -104$ dBm for a gain of 20 dB with a dynamical bandwidth of 50 MHz, which is an order of magnitude better than the device shown in Fig. 1.4 in all respects.

1.4.4 Flux tunability

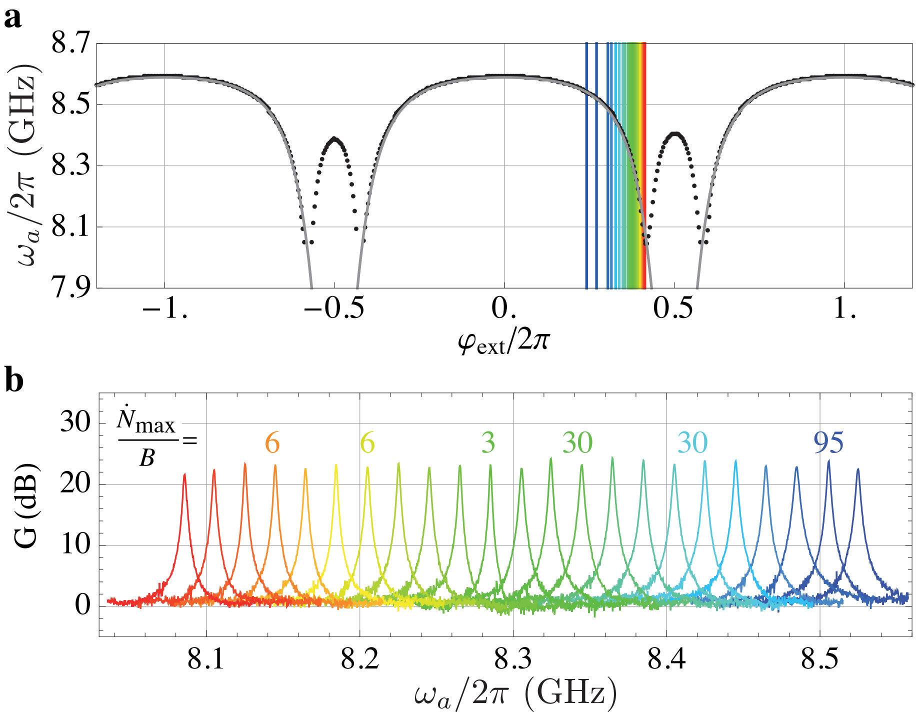

Figure 1.7: **a**. Dots: Measured resonance frequency ω_a of the signal mode as a function of flux applied to the ring modulator without pump. Solid line: fit of ω_a with $\omega_a^0/2\pi =$ 8.82 GHz, $L = 49$ pH, $E_J = \varphi_0 \times 1.9$ μA and including the known stray inductance around the loop $4L_S = 200$ pH see [45]. **b**. Reflection gain measured on the signal port as a function of frequency for various values of the flux indicated by the color lines in **a**. Pump parameters are optimized for each curve. The numbers on top represent the 1 dB compression point (maximum input power) expressed in input photon rate per dynamical bandwidth for six different working frequencies coded by color.

Adding the central inductances to the ring of Josephson junctions (Fig. 1.3) allows to tune the frequencies $\omega_{a,b}$ by changing the magnetic flux without fear of instabilities in the ring's working point. On Fig. 1.7a, we show the measured resonance frequency as a function of flux. The resonance frequency is determined from the dependence of the reflection coefficient on probe frequency. With this sample, we hence get about 500 MHz of tunability through the flux. The measurement is also perfectly described by a simple model. Besides, as the pump power is increased, the reflection gain increases and can reach more than 30 dB. On Fig. 1.7b, the pump frequency and power have been optimized for each flux so as to reach about 20-25 dB of gain.

1.4.5 How close to the quantum limit is it?

We used several ways to probe the efficiency of the Josephson mixer as an amplifier. One way consists in measuring the output noise for a variable and well determined noise at its input. We generated this noise using either a voltage biased tunnel junction [45] or a temperature controlled load [53]. The other way consists in measuring directly the Q distribution at the output while the input Q function is that of a known coherent state. In order to determine the coherent state at the input we used the measurement induced dephasing rate of a qubit state due to this field [54].

Technique	Demonstrated efficiency	Likely dominant imperfection
Amplifying the noise of a tunnel junction [45]	$\eta > 0.3$	Impedance mismatch between the junction and the 50 Ω transmission lines because of a parasitic capacitive coupling
Amplifying the noise of a heated load impedance [53]	$\eta > 0.7$	Losses between the noise source and the amplifier input, where there were a switch, circulators, a hybrid coupler and several cables.
Amplifying a coherent state calibrated using measurement induced dephasing of a qubit [54]	$\eta > 0.8$	Losses between the cavity of the qubit and the amplifier input, where there were two circulators and a hybrid coupler.

Table 1.1: Summary of the measurement degradation observed using various techniques in different samples made using the microstrip geometry shown in Fig. 1.4.

Note that the currently most efficient commercially available amplifiers [55] based on High-Electron-Mobility Transistors are about 30 times less efficient than the Josephson amplifiers in the experiments. Part of it comes from the inefficiency of the device itself but most of it comes from the several dB of unwanted attenuation between the sample at base temperature and the amplifier on the 4 K stage of the dilution refrigerator. However, what they lack in efficiency is compensated by their impressive dynamical bandwidth of a few octaves.

Chapter 2

Generating entanglement between microwave fields

Entanglement is a purely quantum resource, which is essential to the speed up of computation and communication by quantum information. For two qubits, the maximally entangled states are the Bell states of the form $(|00\rangle + |11\rangle)/\sqrt{2}$. Their entanglement is maximal in the sense that dismissing the information about one qubit of the pair (tracing it out) results in a maximally entropic state for the other qubit. Instead of using qubit registers, it is possible to use continuous variables to encode quantum information [56]. In this paradigm, the maximally entangled states are revised. Considering two modes a and b described by harmonic oscillators, the maximally entangled state for an average photon number N in each mode is the two-mode squeezed state and reads

$$|\mathrm{Sq}(N)\rangle = \cosh(r)^{-1} \sum \tanh(r)^n \, |n\rangle_a \, |n\rangle_b \,, \tag{2.1}$$

where $N = \sinh(r)^2$. When both modes are spatially separated, this state describes an Einstein-Podolsky-Rosen (EPR) pair, named after the famous eponymous thought experiment.

While these states are routinely generated in the optical domain, they had remained elusive in the microwave domain. Earlier attempts by Yurke and coworkers in 1988 [57] showed how to generate single mode squeezed states in the microwave domain using superconducting circuits. However, the field needed the strong advances in microwave engineering and nanofabrication that occurred during the following 20 years in order to push forward these techniques. In 2008, the Boulder group presented a degenerate amplifier able to produce single mode squeezed states less than 10 dB below vacuum fluctuations [24, 58]. Using two sidebands of degenerate parametric amplifiers, one can then produce two-mode squeezed states [27, 59]. In order to produce an EPR pair, delocalized on two transmission lines, one needs to go a step further.

One route consists in sending a single-mode squeezed vacuum state and an unsqueezed

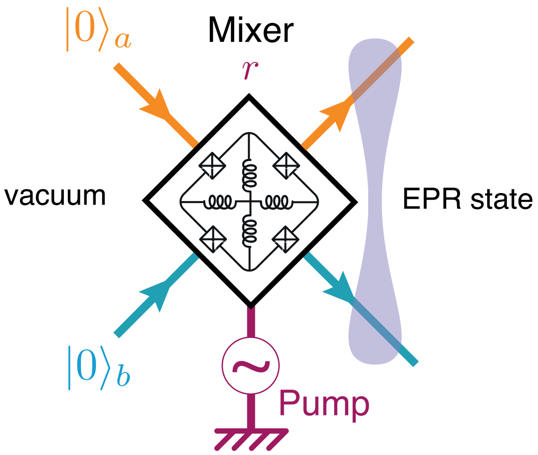

Figure 2.1: Scheme of the production of an EPR pair using a Josephson mixer.

vacuum state towards a beam-splitter. This strategy was demonstrated after our work in Ref. [60]. We chose instead to use a non-degenerate amplifier, which is the Josephson mixer described in section 1.3. By applying a pump signal to this mixer (which we call the "entangler") while starting from the vacuum state, a two-mode squeezed state is produced at its output (Fig. 2.1). Using Eq. (1.12), it is straightforward to show that

$$S\,|0\rangle_a\,|0\rangle_b = |\mathrm{Sq}(N)\rangle. \tag{2.2}$$

There are several ways to demonstrate entanglement between two modes. A straightforward method consists in performing simultaneous heterodyne measurements of the two modes and checking whether or not the cross-correlations between modes are larger than classically allowed [27, 15, 60]. We have used this technique for demonstrating entanglement between a quantum memory and a transmission channel (see section 2.2.3). Here, we have used yet another method, which consisted in building a quantum circuit able to witness entanglement. Therefore our experiment not only demonstrates entanglement between two remote microwave fields at different frequencies, but also demonstrates how it can be used as a resource in a quantum circuit.

2.1 Josephson mixer as an entanglement detector

2.1.1 Destructing coherent fields with a Josephson mixer

The key ingredient of this quantum circuit is the use of another Josephson mixer (which we call the "analyzer") to recombine the two modes which are supposedly entangled (Fig. 2.2).

From the scattering relations Eq. (1.13), one gets for large analyzer gain $\cosh^2(r_A)$

$$\hat{a}_{out,A} \approx \cosh(r_A)(\hat{a}_{in,A} + e^{i\varphi_{P,A}}\hat{b}^\dagger_{in,A}) \tag{2.3}$$

where $\varphi_{P,A}$ is the phase of the pump. Therefore, when properly choosing the coherent fields incoming on a and b ports such that $\langle\hat{a}_{in,A}\rangle = -e^{i\varphi_{P,A}}\langle\hat{b}_{in,A}\rangle^*$, destructive interferences between incoming fields cancel the output field on a. This effect was advertised in Ref. [61] as an anti laser. Instead of generating two such coherent fields using two microwave generators, we can generate them using another Josephson mixer (the "entangler" in Fig. 2.2a). By sending a coherent field at the input $b_{in,E}$ of the entangler, it outputs two signals that depend on the entangler pump phase $\varphi_{P,E}$ as

$$\langle\hat{a}_{out,E}\rangle \approx e^{i\varphi_{P,E}}\cosh(r_E)\langle\hat{b}_{in,E}\rangle^* \text{ and } \langle\hat{b}_{out,E}\rangle = \cosh(r_E)\langle\hat{b}_{in,E}\rangle, \tag{2.4}$$

where we have used the large gain approximation $\cosh(r_E) \approx \sinh(r_E)$. When these two signals are sent at the input of the analyzer, one gets an outgoing amplitude on the a mode of the analyzer given by

$$\langle\hat{a}_{out,A}\rangle \approx \quad \cosh(r_E)\cosh(r_A)e^{i\varphi_{P,E}}\langle\hat{b}_{in,E}\rangle^* \underbrace{\left(1 + e^{i\Delta\varphi}\right)}_{\text{interfere}}, \tag{2.5}$$

with $\Delta\varphi = \varphi_{P,A} - \varphi_{P,E}$ the phase difference between both pumps. When the two pump signals are opposite, the analyzer indeed suppresses all the incoming signals[1].

In Fig. 2.2b is shown the measured amplitude $|\langle\hat{a}_{out,A}\rangle|^2$ (normalized by $|\langle\hat{b}_{in,E}\rangle|^2$) as a function of phase difference $\Delta\varphi$ for various entangler gains $\cosh^2 r_E$. As expected from the interference term in Eq. (2.5), the output signal amplitude nearly cancels for $\Delta\varphi = \pi$. Last year, Schackert and coworkers have investigated the energy conservation involved in this signal cancellation by measuring the extra energy found in the output of the pump mode [62].

2.1.2 Entanglement witness

Now, it is important to note that the destructive interference we have just discussed only concerns the mean value of the fields but not their fluctuations. In fact, when two non-entangled coherent fields destructively interfere with the Josephson mixer, their average value cancel but their fluctuations are on the contrary amplified by the gain of the mixer.

We have shown that, if the two input modes are non-entangled, the level of noise at the output of one mode of the mixer is always larger than the level of amplified vacuum

---

[1] Note that on the b output port, at the most destructive phase difference ($\Delta\varphi = \pi$), the field amplitude is not zero but equal to $\langle\hat{b}_{in,E}\rangle$. From the point of view of the second mixer though, it corresponds to a reduction by a factor $\cosh(r_E)$ between input and output.

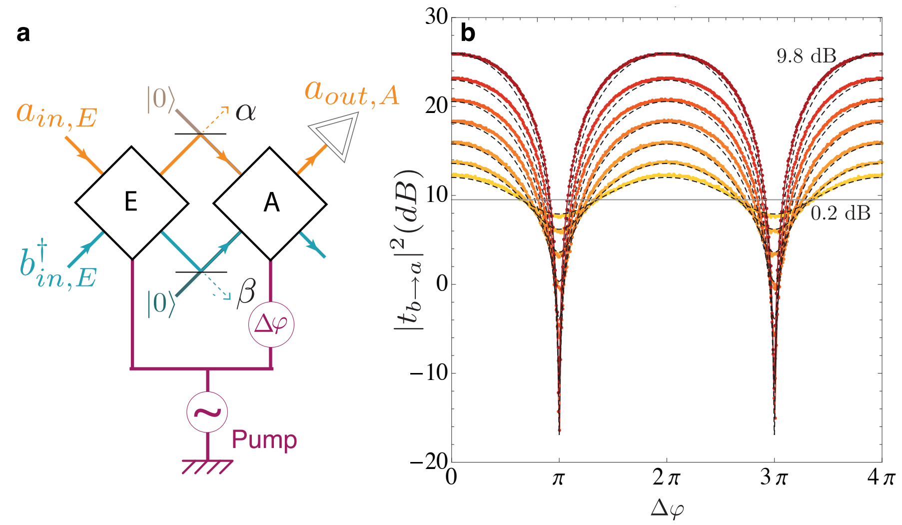

Figure 2.2: **a** Scheme of the circuit demonstrating the cancellation of two coherent states using a Josehpson mixer. Each diamond represents one Josephson mixer, nicknamed the entangler (E) or the analyzer (A). It has two inputs and two outputs: orange for mode a at 5.6 GHz and blue for mode b at 8.8 GHz. Losses are modeled as beam splitters of transparency α^2 and β^2 coupling a cold load to the signals. **b.** Color traces: measured intensity of the output field $|\langle a_{out,A}\rangle|^2$ in units of the intensity $|\langle b_{in,E}\rangle|^2$ of the coherent field sent on the b input mode, plotted as a function of the phase difference $\Delta\varphi$ between the pump signals. Here, the input of a is in the vacuum state. The gain of the analyzer is set to $G_A = \cosh^2 r_A = 10$ (solid gray line). Each trace and color corresponds to a different gain for the entangler $G_E = \cosh^2 r_E = 0.2, 0.8, 1.8, 3.2, 5, 7.2, 9.8$ dB. Dashed lines: fits to the data using equation (3) in Ref. [53] and the single fit parameter $(1-\beta)/(1-\alpha) = 0.945$.

fluctuations. This can be viewed by calculating the output noise on port a for a non-entangled pair of incoming fields. Assume that $\rho_{in} = \sum_i p_i \rho_a^{(i)} \otimes \rho_b^{(i)}$. Let us also assume that $\langle a_{in}\rangle = \langle b_{in}\rangle = 0$ for simplicity. Then, the level of noise referred to the input (divided by the gain $\cosh(r)^2$ is (see Fig. A.3 for the definition of Var_W)

$$\frac{\mathrm{Var}_W(a_{out})}{\cosh(r)^2} = \frac{1}{2}\left\langle\left\{\hat{a}_{in} + e^{i\varphi_P}\hat{b}^\dagger_{in}, \hat{a}^\dagger_{in} + e^{-i\varphi_P}\hat{b}_{in}\right\}\right\rangle. \tag{2.6}$$

Hence,

$$\frac{\mathrm{Var}_W(a_{out})}{\cosh(r)^2} = \left\langle \hat{a}^\dagger_{in}\hat{a}_{in}\right\rangle + \left\langle \hat{b}^\dagger_{in}\hat{b}_{in}\right\rangle + 2\mathrm{Re}\left(e^{i\varphi_P}\langle \hat{a}_{in}\hat{b}_{in}\rangle\right) + 1. \tag{2.7}$$

Then, from the expression of ρ_{in}, one gets the inequality

$$\frac{\mathrm{Var}_W(a_{out})}{\cosh(r)^2} \geq \sum_i p_i \left| \langle \hat{a}_{in} \rangle_i + e^{i\varphi_P} \langle \hat{b}^\dagger_{in} \rangle_i \right|^2 + 1 \geq 1. \tag{2.8}$$

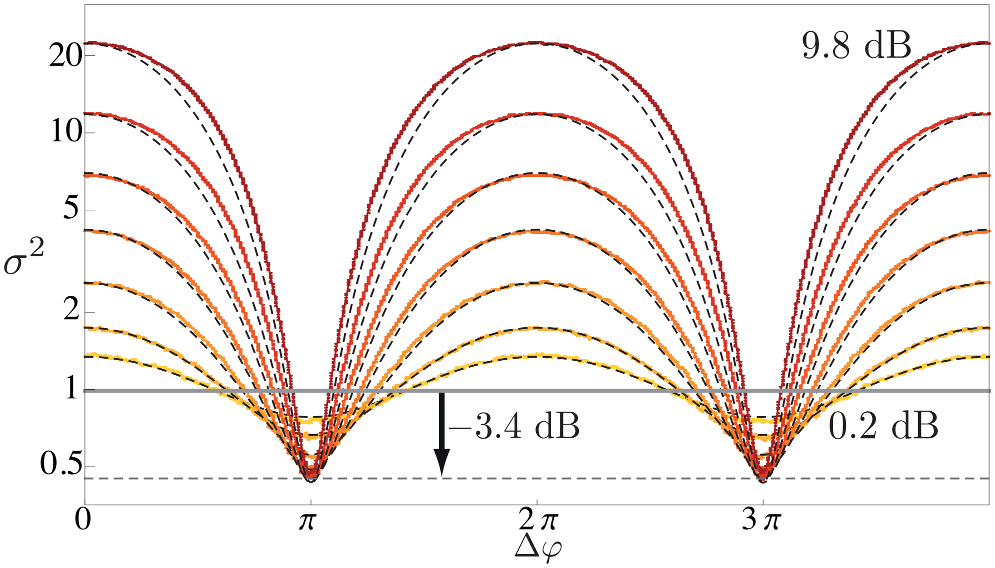

Figure 2.3: **a.** Color traces: variance of the output mode $\mathrm{Var}_W(a_{out})$ referred to the case of vacuum input on the analyzer (divided by $\cosh(2r_A)/2$) as a function of phase difference $\Delta\varphi$, determined by measuring the spectral density of the noise at the analyzer a output when only quantum noise enters the entangler. Each color corresponds to the same gain of the entangler G_E as in Fig 2.2b with a fixed gain on the analyzer $G_A = \cosh^2 r_A = 10$. The horizontal line at $\sigma^2 = 1$ represents the measured noise for amplified vacuum at the output of the analyzer ($r_E = 0$). For $\Delta\varphi$ close to π, the measured noise goes below this level, an evidence of entanglement. Dashed lines: predicted variance using $\alpha = 0.37$ and $\beta = 0.40$.

This shows that for any separable state at the input (non entangled a and b modes), the noise at the output of a cannot be smaller than the amplified vacuum noise (which is 1). In the experiment, we show that the noise goes below this threshold for $\Delta\varphi = \pi$, hence demonstrating the entangled nature of the fields produced by the Josephson mixer A (Fig. 2.3). In practice, the noise level was 3.4 dB lower than the threshold, which corresponds to the production of 6 millions of equivalent entangled bits per second given the rather large bandwidth of the mixer. This value is here limited by the losses introduced by the reflections on the various commercial components used to connect the first Josephson mixer to the second. In theory, without any loss, one would have got close to 12 dB of noise compression with the pump amplitudes used in the experiment.

After our work, this experiment was reproduced in the optical domain in Ref. [63] where similar noise cancellation was observed.

2.2 Quantum node for entanglement and storage of microwave radiation

Once coupled to various quantum systems [5, 6, 7, 2], microwave fields could realize quantum networks, in which entangled information is processed by quantum nodes and distributed through photonic channels [64, 65]. The quantum nodes should generate and distribute microwave entangled fields while controlling their emission and reception in time. We have seen in the previous section that superconducting circuits are able to generate entanglement. On the other hand, quantum memories provide control in time as demonstrated in emerging implementations in the microwave domain using spin ensembles [66, 67, 68], superconducting circuits [69, 70] or mechanical resonators [71, 72]. In this section, we present a promising device for storing and manipulating microwave radiation based on the Josephson mixer. Our device offers the advantage of having a large storage efficiency (80 %) and the ability to generate entanglement shared between a memory and a propagating mode of a transmission line.

2.2.1 Time control of the coupling to a cavity

Contrary to the perspective of building an amplifier or a fast entanglement generator, for which the coupling rates of both ports a and b are maximized, we consider here the case where one of the resonators of the Josephson mixer is as closed as possible $\kappa_b \ll \kappa_a$. In this case, the b mode becomes a storage medium while the a mode becomes a buffer cavity that provides an input/output port to the memory. In order to maximally close the b mode, we used a superconducting 3D cavity [73] (see Fig. 2.4). The principle of this memory consists in turning on or off the coupling between a and b modes using a pump field. In this sense, it is similar to the circuit demonstrated in Refs. [69, 70].

Effectively, it is possible to transfer what is stored in mode a at frequency ω_a into the memory mode b at frequency ω_b. This is realized in the conversion mode of the Josephson mixer, when the pump frequency is not the sum of both resonator frequencies as in sections 1.4 and 2.1, but their difference $\omega_p = \omega_a - \omega_b$. The mixing Hamiltonian can then be approximated to

$$H_{mix} = i\hbar\chi_{abp}(\hat{a}^\dagger\hat{b}\hat{p} - \hat{a}\hat{b}^\dagger\hat{p}^\dagger). \tag{2.9}$$

This regime has recently been explored experimentally in Ref. [48], in the context of fast frequency conversion with large coupling rates on each resonator. In the stiff pump regime,

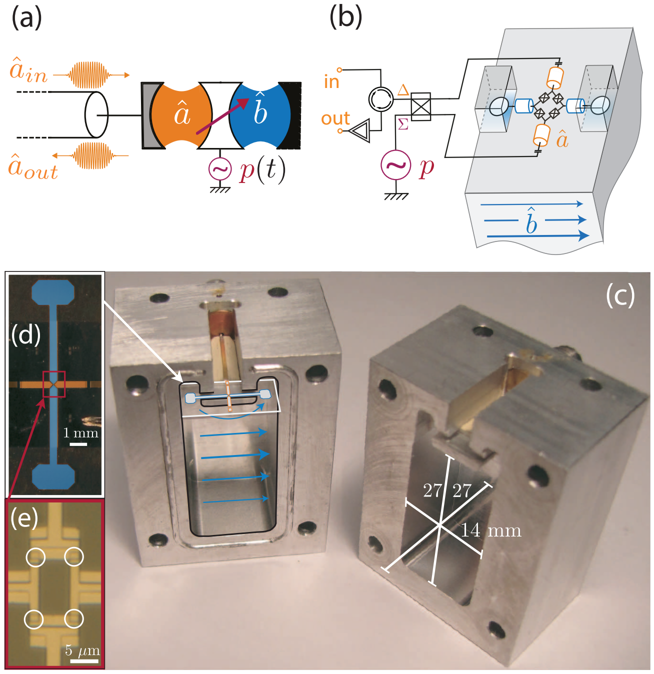

Figure 2.4: (a) Schematic of the experimental setup. A high-Q memory mode $\hat{b}$ is parametrically coupled to a low-Q buffer mode $\hat{a}$, hence to input/output propagating modes $\hat{a}_{in}$ and $\hat{a}_{out}$, depending on the pump amplitude p. (b),(c) Schematics and picture of the device. The on-chip circuit couples to a 3D superconducting cavity via antennas. The blue arrows represent the polarization of the fundamental mode TE 110 in the cavity. The Josephson ring and buffer resonator are on-chip. The differential mode (Δ) couples with the buffer mode while the common mode (Σ) is used for addressing the pump. (d) Picture of the aluminum circuit fabricated on a c-plane sapphire substrate. The antennas (blue) and the buffer microstrip resonator (orange) are highlighted in false color. (e) Optical microscope image of the Josephson ring at the crossing between antennas and buffer resonator. The Josephson junctions are circled in white.

the pump operator $\hat{p}$ can be replaced by a scalar number so that we introduce

$$\chi_{ab} e^{i\varphi} = \chi_{abp} \langle \hat{p} e^{i\omega_p t} \rangle \tag{2.10}$$

and thus

$$H_{mix} = i\hbar\chi_{ab}(\hat{a}^\dagger \hat{b} e^{i\varphi} - \hat{a}\hat{b}^\dagger e^{-i\varphi}). \tag{2.11}$$

Input/output rate

For a given pump amplitude, one defines the input/output coupling rate γ_{io} of the node as the inverse characteristic decay time of the memory mode. Its expression can be found by solving the Langevin equations for the memory mode b and for the fields coming in and out of the buffer resonator a [50]. We get

$$\gamma_{io} \approx \frac{\kappa_a}{2} \mathrm{Re} \left(1 - \sqrt{1 - 4\frac{|\chi_{abp} p|^2}{\kappa_a^2}} \right). \tag{2.12}$$

For larger pump power $\chi_{abp}|p| > \kappa_a/2$, the system enters the strong coupling regime. The coupling rate overcomes the output losses κ_a, thus the two modes hybridize. Consequently, the input/output rate saturates to $\gamma_{io}(\chi_{abp}|p| > \kappa_a/2) = \frac{\kappa_a}{2}$. The input/output rate being only limited by the largest coupling rate of both resonators a and b, one can reach rather large writing times for the memory.

Reflection measurements

We have tested our understanding of the input/output relations leading to Eq. (2.12) by measuring the reflection coefficient $R_{aa} = a_{out}/a_{in}$ as a function of frequency for various pump powers in a preliminary device with coplanar resonators (Fig. 2.5). The input/output formalism gives the following approximate expression for R_{aa} close to resonance

$$R_{aa} = \frac{\kappa_a - \kappa_{a\to b} + 2i\delta\omega_a}{\kappa_a + \kappa_{a\to b} - 2i\delta\omega_a}. \tag{2.13}$$

Here, $\delta\omega_a$ is the detuning between the probe field and resonance frequency of mode a, and $\kappa_{a\to b}$ is given by

$$\kappa_{a\to b} = \kappa_a C \left(1 - 2\frac{i\delta\omega_a + i\delta\omega_p}{\kappa_b} \right)^{-1} \tag{2.14}$$

with $C = 4\chi_{abp}^2|p|^2/(\kappa_a\kappa_b)$ the cooperativity – see Eq. (1.21) – and $\delta\omega_p$ the detuning between the pump frequency and the difference $\omega_a - \omega_b$. In figure 2.5, one can see the following regimes of power accessed experimentally.

- For $C < \kappa_b/\kappa_a$, the usual characteristics of a single resonator measured in reflection are observed: a 2π phase shift with increasing probe frequency and a constant amplitude.

- For $\kappa_b/\kappa_a < C < 1$, the coupling between resonators a and b becomes effective so that an extra loop appears in the quadrature phase space (Fig. 2.5c). This loop translates into a slope change in the phase shift and the appearance of a dip in the reflected amplitude.

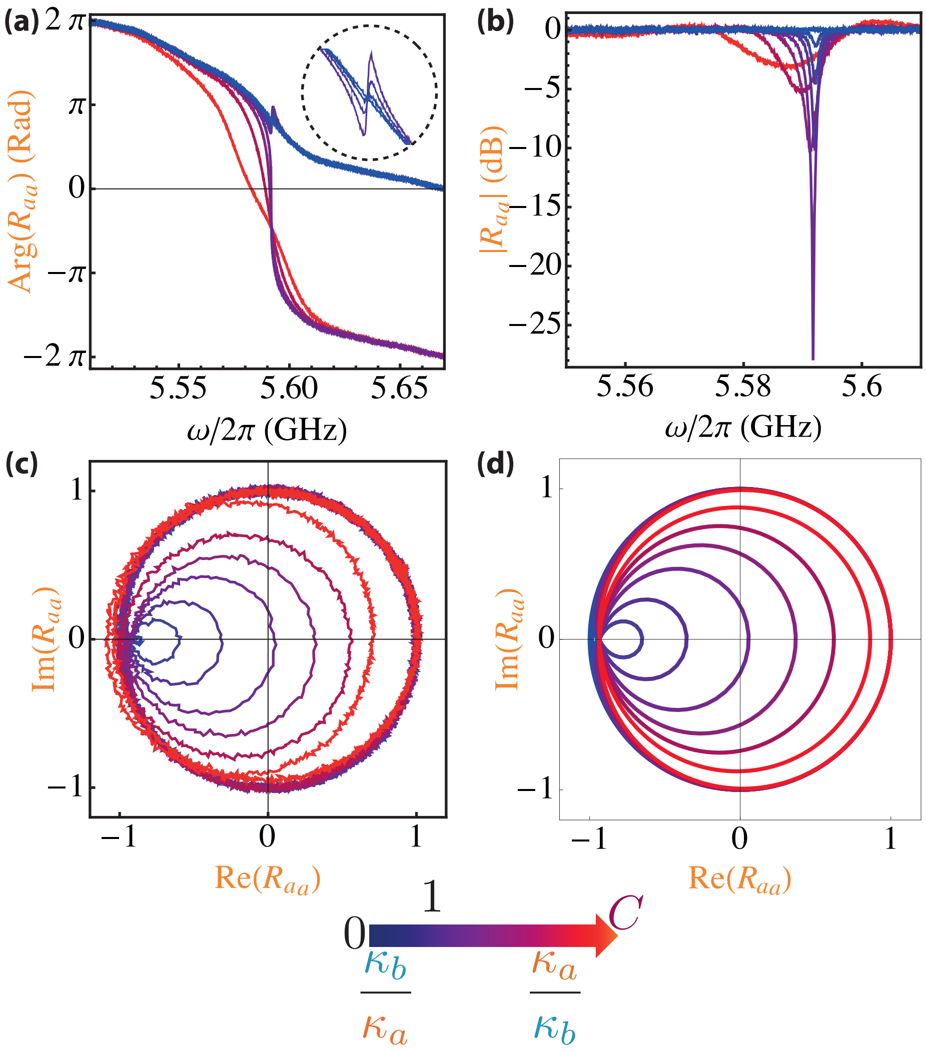

Figure 2.5: Reflection coefficient R_{aa} on port a as a function of frequency for various values of the pump power (cooperativity C encoded in color). **(a)** Measured phase. **(b)** Measured amplitude. **(c)** Measured reflection coefficient in polar coordinates. **(d)** Expected behavior of R_{aa} using Langevin equations.

- For $C = 1$, the conversion rate $\kappa_{a\to b}$ is equal to κ_a at resonance so that the reflection goes to zero. At this point, a continuous wave incoming on a is entirely converted into the b mode and exits through the b losses.

- For $1 < C < \kappa_a/\kappa_b$, a 4π phase shift develops in reflection.
- For $\kappa_a/\kappa_b < C$, the 4π phase shift decomposes into two 2π phase shifts, each indicating a resonance. This is the strong coupling regime, where the conversion rate lifts the effective degeneracy between the two hybridized resonators.

2.2.2 Storage and retrieval

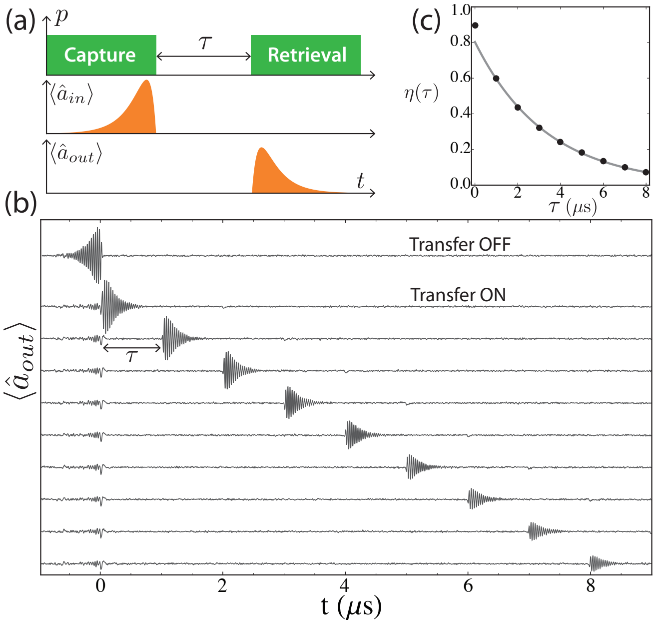

Figure 2.6: (a) Capture, store and release protocol. Pulse sequences for the pump field p (green) at the difference frequency $f_p = f_a - f_b$, the input field a_{in} and the resulting output field a_{out} (orange). The temporal shape of the input field is chosen in order to optimize the capture efficiency. (b) Time traces of the amplitude of the output field down converted to 40MHz and averaged 6×10^4 times. The top trace is measured without pump and reveals the optimized input signal. The following traces correspond to the sequence of (a) with increasing delay τ between capture and retrieval from 0 μs to 8 μs. (c) Dots: retrieval efficiency η as function of delay τ. η is defined as the ratio of the retrieved energy normalized to the input energy. Plain line: exponential decay $\eta_0 e^{-\tau/\tau_m}$ characterizing the memory lifetime. Best fit obtained for $\eta_0 = 80$ % and $\tau_m = 3.3$ μs.

In a practical quantum network, the temporal shape of the transmitted fields plays a crucial role in the efficiency of the coupling to the node. Given the shape of the incoming pulse, the pump temporal shape needs to be optimized in order to most efficiently catch the pulse. Reciprocally, one may use a square shape for the pump amplitude and optimize the temporal shape of the incoming wave packet using techniques such as in Ref. [74].

This optimal envelope is shown in Fig. 2.6a. It is the time-reverse of the pulse released by the memory when applying a square pump, that is close to a rising exponential with characteristic time γ_{io}, similar to what was demonstrated in Refs. [69, 70]. The amplitude $\langle \hat{a}_{out} \rangle$ of the mode coming back from the device is measured for several pump pulse sequences (Fig. 2.6b). In a first control measurement (top trace), the pump is kept turned off such that the measurement corresponds to the directly reflected incoming pulse. In the following measurements (traces below) the pump is turned on before time 0 and after time τ (Fig. 2.6a). Only 5 % of the incoming pulse energy is reflected while it is sent at $t < 0$ indicating the efficient absorption of this pulse shape. When the pump is turned back on after a delay τ, the device releases the captured state back in the transmission line as can be seen in Fig. 2.6b.

Calculating the memory efficiency η, which is the ratio between the retrieved pulse energy and the incoming pulse energy leads to an exponential decay as a function of delay time $\eta(\tau) = \eta_0 e^{-\tau/\tau_m}$ (Fig. 2.6c). The memory lifetime $\tau_m = 3.3$ μs is much larger than γ_{io}^{-1} but limited by unidentified losses in the 3D cavity coupled to the antennas. The much smaller decay rates achieved in similar 3D cavities [75, 73] leave room for improvement in the future. Besides the outgoing phase is identical to that of the incoming pulse, demonstrating that the memory preserves phase coherence. Finally, the number of operations that can be performed by the memory within its lifetime is limited by the time-bandwidth product $\gamma_{io}\tau_m = 30$. This combination of large memory efficiency and time-bandwidth product makes this device a state of the art quantum memory [76].

2.2.3 Entanglement between the node and a communication channel

Up to now, we have presented the circuit mostly as a quantum memory such as the one in Ref. [69, 70]. In fact, using the flexibility of the Josephson mixer, we can also generate a pair of entangled states (similar to what was done in section 2.1) shared between the memory and a propagating mode of the transmission line. This is done by applying a pump pulse at the sum frequency $f_p = f_a + f_b$ with both modes initially in the vacuum. At a later time, the content of the memory mode b can be released using the protocol described in the previous section (Fig. 2.7a).

We have performed a full tomography of the system made of the propagating wave packet on transmission line a_{out} and of the memory mode b by performing repeated heterodyne measurements of the mode a_{out} and of the later released memory mode b [15]. The second-order correlations between the measured quadratures of the two modes characterize the Gaussian state completely and are summarized in the covariance matrix (Fig. 2.7b). In practice, we have used an FPGA board (see Ref.[15]) to pre-process the measurements and extract the covariance matrix out of 40 millions pulse sequences in only 5 minutes.

The entanglement between the 3D cavity mode b and the propagating mode a_{out} re-

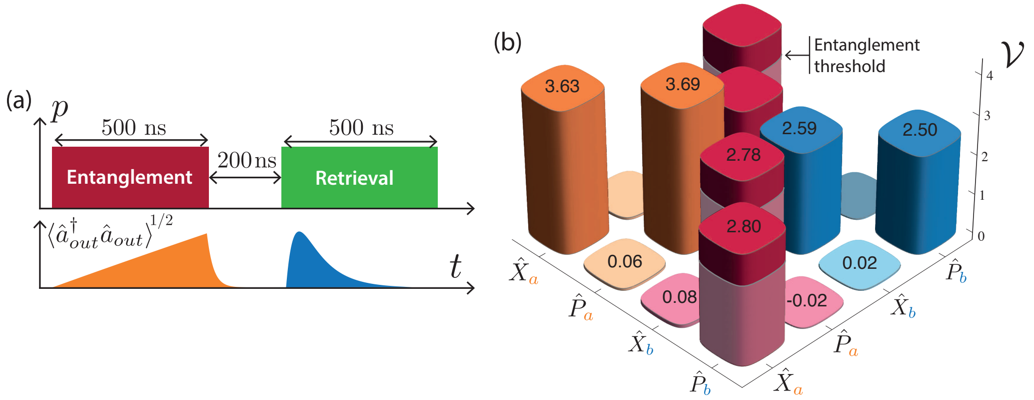

Figure 2.7: Entanglement between memory and propagating mode. (a) Scheme of the pulse sequence. Top: pump amplitude p is shown in red for $f_p = f_a + f_b$ and in green for $f_p = f_a - f_b$. Bottom: output noise amplitude in time. (b) Measured two-mode covariance matrix. The convention used is such that the vacuum state corresponds to the unity matrix. The 2×2 block-diagonal matrices in orange and blue represent the single mode $\hat{a}$ and $\hat{b}$ covariance matrices. The off-diagonal matrices in red represent the correlations between modes. Correlations go beyond the greyed regions which demonstrates entanglement.

sult in stronger cross-correlations between modes than allowed by classical systems. The corresponding entanglement threshold in the cross-correlator $\langle X_a P_b \rangle$ is indeed experimentally exceeded as can be seen in (Fig. 2.7b). The number of equivalent entangled bits (logarithmic negativity) is here close to 1.4.

In the end, we have developed and characterized a set of devices able to manipulate and entangle microwave fields in time. The versatility of these circuits paves the way for complex quantum communication protocols in the microwave domain such as continuous variable quantum teleportation [77, 78, 79, 80]. Besides, it provides a useful resource for 3D cavities where the on-demand extraction of a field quantum state was needed. This could be used to implement readout and feedback in cavity networks or even quantum computation with the memory field itself [81]. Finally, superconducting qubits can easily be embedded in this device, which could lead to protected quantum memories [2] and even protected quantum computing with microwave fields [81, 82].

Chapter 3

Controlling a quantum system by feedback

Error correction was developed in order to preserve or transmit data reliably despite the possible flaws of the support of information. These effective protocols work well for classical information. In a quantum system, two elementary assumptions used in classical error correction break down. First, the state of a quantum bit does not span only two values but a bi-dimensional vector space. Second, the sole fact of measuring the state of a system modifies it. In these circumstances, it is outstanding that a quantum state may still be preserved from decoherence, control and measurement errors using correction codes, as Shor first discovered in 1995 [83, 84, 85, 86].

The practical requirements for implementing quantum error corrections are still out of reach of current technologies, but various systems are getting closer every year [2]. Therefore, the dynamical control of quantum systems needs to be developed in this perspective.

The simplest way to control a quantum system consists in sending classical driving signals to modify its state. Yet, this open-loop control strategy has no grasp on the fact that the environment measures the system, which leads to decoherence. Only feedback control can fight decoherence efficiently. Two complementary feedback strategies coexist [87]:

- measurement based feedback consists in measuring the quantum system and modifying the driving signals depending on the measurement record,

- autonomous feedback consists in coupling the quantum system of interest to another driven quantum device able to stabilize it.

In this chapter, we present experiments on superconducting circuits that fall in one of the two categories. First, we have used measurement based feedback to stabilize a desired evolution of a quantum bit. Second, we have used autonomous feedback to cool down a quantum bit.

3.1 Stabilizing a quantum trajectory by measurement feedback

Few experiments have demonstrated the stabilization of a state (dynamic or not) by measurement feedback. In 2011, a first experiment [88] demonstrated the stabilization of a chosen number of photons in a microwave cavity. Weak measurements of the photon number were repeatedly performed using flying Rydberg atoms. Depending on the measurement record, a digital feedback loop tunes a classical driving input field, which preserves the desired number of photons. The classical driving field was later replaced by single photon excitations for better efficiency [89, 90].

Instead of controlling the state of a cavity, a single qubit can be controlled and measured using a circuit-QED architecture. It is therefore possible to control a qubit state dynamically by measurement based feedback. In 2012, Vijay and coworkers [91] used an analog feedback loop to stabilize the Rabi oscillations of a qubit permanently. When the superconducting qubit is non-resonantly coupled to the cavity, the phase of the transmitted field at cavity frequency depends on qubit state. The continuous monitoring of the transmitted field hence provides a weak QND (quantum non demolition) measurement of the qubit. The principle behind the stabilization of Rabi oscillations at 3 MHz is simple. The feedback loop needs to increase (decrease) the drive amplitude when the measured qubit trajectory is behind (ahead of) schedule. In Ref. [91], this was done by multiplying the 3 MHz reference with the weak measurement output and adding this signal to the resonant driving field amplitude.

This protocol works but is suboptimal in terms of efficiency. Indeed, continuous measurement exerts a constant dephasing rate in time, which can only degrade quantum purity when the state of the qubit is not in measurement basis. In order to maximize the feedback efficiency, one needs to adjust the measurement strength in time as we demonstrate in Ref. [92]. In our experiment, we use stroboscopic measurements that enable varying this dephasing rate in time. For trajectories like Rabi oscillations that go through eigenstates of the measurement observable (poles of the Bloch sphere), we turn on the measurement only close to the ground state which is insensitive to measurement induced dephasing, hence better preserving coherence over the whole trajectory. Besides, the stroboscopic method allows to stabilize trajectories like Ramsey oscillations, which never reach measurement eigenstates, by rotating periodically the measurement basis.

3.1.1 Experimental constraints

Several features were required to realize measurement feedback. First, we engineered a superconducting qubit in cavity with a large decoherence time ($T_2 > 10\ \mu$s)., benefiting from the recent development of the 3D transmon by Paik and coworkers [75]. Second, we used an amplifier close to the quantum limit (see Table 1.1) so that the efficiency of the detection setup is 82 % (which is still a world record). Finally, we programmed a fast electronics board (Field Programmable Gate Arrays) in order to implement digital feedback so that the total delay between measurement and correction was only 500 ns including propagation along the cables (Fig. 3.1).

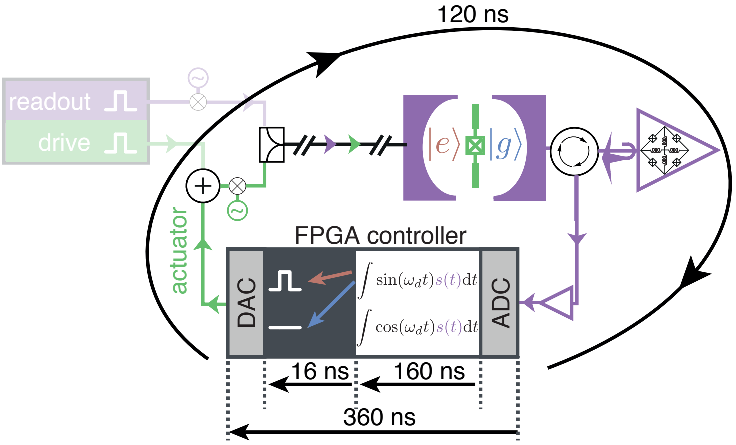

Figure 3.1: Illustration of the delays added by the various steps of the feedback loop (see Ref. [54] for details). The qubit is a transmon circuit (green) in a 3D aluminum cavity (purple). The transmitted field at cavity frequency is amplified using a Josephson mixer (triangle) and processed using an FPGA controller. Depending on the result a fast π pulse is sent or not at the qubit frequency.

3.1.2 Cooling down a qubit by measurement based feedback

Before discussing the stabilization of a quantum trajectory in time, let us focus on the deterministic stabilization of a given qubit state. This was first done by Ristè and coworkers in 2012 [93, 94] and we used a similar protocol in our experiment. The transmitted part of a pulse sent at cavity frequency realize a single shot measurement of the qubit state. If the qubit is found in the excited state, the FPGA board sends a fast π-pulse in order to put it in the ground state. Using this protocol, we could lower the qubit population from 50 % down to 3.6 % when starting from a maximally entropic state, and from 2.4 % down to 0.7 % when starting from thermal equilibrium.

3.1.3 Stabilizing Rabi and Ramsey oscillations

Without feedback, a constant driving field at qubit frequency produces Rabi oscillations of the qubit in the σ_X, σ_Z plane of the Bloch sphere (Fig. 3.2a). Due to decoherence, the oscillations decay in a characteristic time, which is here $T_R = 15.5\ \mu$s. The goal of feedback control is to preserve the oscillations despite decoherence. To do so, a strong measurement is performed each time the qubit is supposed to reach the ground state. If it is found in the ground state, the oscillations go on with the right phase. If not, a fast π-pulse is applied, so that the qubit goes back on the right track. The resulting measured oscillations in the Bloch sphere are shown in Fig. 3.2b. The average purity $\overline{\mathrm{Tr}(\rho^2)}$ of the density matrix ρ is calculated to be 80%, the time averaged fidelity $F = \overline{\langle\psi_{\mathrm{targ}}|\rho(t)|\psi_{\mathrm{targ}}\rangle}$ to the target trajectory $|\psi_{\mathrm{targ}}\rangle$ is $F = 85\%$ and the average preserved information quantity $1-\mathrm{Tr}(-\rho\log\rho) = 0.50$ bit. This is indeed more efficient than for continuous feedback where only 0.15 bit was preserved on average in Ref. [91].

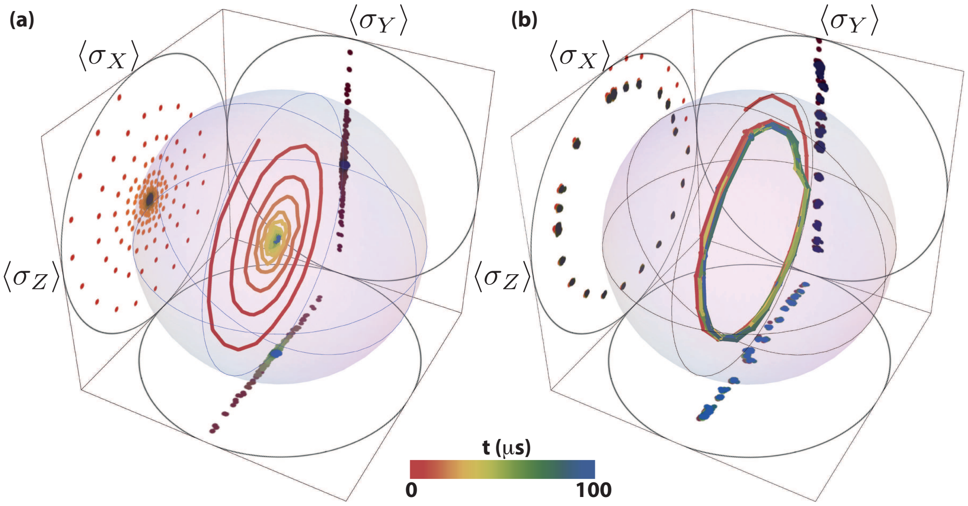

Figure 3.2: (**a**) Measured decaying Rabi oscillations represented in the Bloch sphere. Here, the Rabi period is 6.284 μs and they decay in $T_R = 15.5$ μs. Time is encoded in color. (**b**) Similar representation of the measured stabilized Rabi oscillations.

Similarly, it was possible to stabilize Ramsey oscillations. These oscillations can be observed by first preparing the qubit in state $(|g\rangle + |e\rangle)/\sqrt{2}$ and then realizing a qubit tomography as a function of time. In order to connect to the usual representation of Ramsey fringes at a given frequency ω_{Ry}, we can rotate linearly in time the measurement axis so that $\langle\sigma_X\rangle$ maps onto $\langle\cos(\omega_{Ry}t)\sigma_X+\sin(\omega_{Ry}t)\sigma_Y\rangle$ and $\langle\sigma_Y\rangle$ onto $\langle-\sin(\omega_{Ry}t)\sigma_X+\cos(\omega_{Ry}t)\sigma_Y\rangle$.

Without measurement based feedback, the Bloch vector of the qubit decays exponentially both in Z ($T_1 = 28$ μs) and in the X, Y plane ($T_2 = 11.5$ μs) as shown in Fig. 3.3a. The stabilization by feedback works as follows. Every 4 μs, the qubit is rotated by $\pi/2$ and measured. The rotation axis is chosen so that the qubit should be found in state $|g\rangle$ if it follows the targeted trajectory. Therefore, if it is found in $|e\rangle$, a fast actuation π pulse puts it back in the desired state $|g\rangle$. It is then rotated back by $-\pi/2$ to go back to the Ramsey trajectory, with the right phase. Using this stroboscopic measurement based feedback, Ramsey oscillations are indeed preserved indefinitely (Fig 3.3b). The average purity

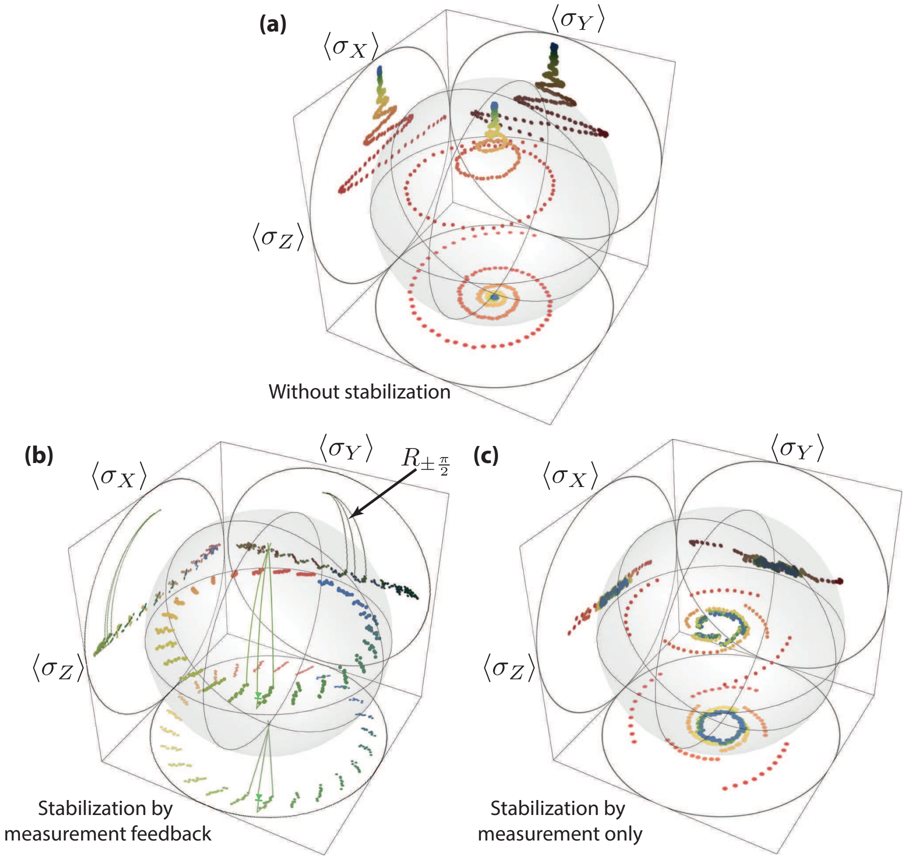

Figure 3.3: (**a**) Measured evolution of the qubit initially prepared in state $(|g\rangle + |e\rangle)/\sqrt{2}$ at time 0 represented in the Bloch sphere with a Ramsey frequency $\omega_{Ry}/2\pi = 100$ kHz. At each time (color as in Fig. 3.2), the outcome of qubit tomography is represented as a dot in the Bloch sphere and in the three orthogonal projection planes. The large black circles set the scale of the Bloch sphere extrema. (**b**) Same evolution as in (a) with stroboscopic measurement feedback every 4 μs. The Ramsey frequency is chosen at $\omega_{Ry}/2\pi = 10$ kHz instead of 100 kHz for a clearer observation of the trajectory. State tomography is only performed outside of the sensing and actuation periods. The simulated trajectory is represented as a line during a 6 μs interval. (**c**) Evolution of the qubit with the same process as in (b) but without actuation. An average persistent coherence of 18 % remains without any actuation. Here, $\omega_{Ry}/2\pi = 100$ kHz.

$\mathrm{Tr}(\rho^2)$ of the density matrix ρ is calculated to be 85%, the time averaged fidelity $F = 76\%$ and the average information quantity 0.60 bit. Note that the measured trajectories shown in Figs. 3.3 and 3.2 are perfectly reproduced by a resolution of the Bloch equations in a piecewise manner (see Ref. [54]).

3.2 Autonomous feedback

Interestingly, the sole effect of stroboscopically measuring the qubit, without any measurement feedback, induces persistent Ramsey oscillations, even though with less purity (52%), fidelity (56%) and information quantity (0.03 bit) (Fig 3.3c). This is due to the relaxation of the qubit during the measurement period towards state $|g\rangle$ making it more probable to reinitiate in state $(|g\rangle + |e\rangle)/\sqrt{2}$ than in state $(|g\rangle - |e\rangle)/\sqrt{2}$ after the measurement ends. This stabilization without actuation enters in the domain of autonomous feedback or reservoir engineering. Indeed, the control fields resulting in the successive rotations and measurements use the natural dissipation in the environment of the qubit/cavity system so that relaxation can be steered towards any chosen state. This kind of reservoir engineering was investigated in depth by Murch and coworkers in 2012 [95]. By continuous wave control fields, they were able to engineer dissipation so that the qubit relaxes in state $|g\rangle + |e\rangle/\sqrt{2}$ with a state purity of 70%.

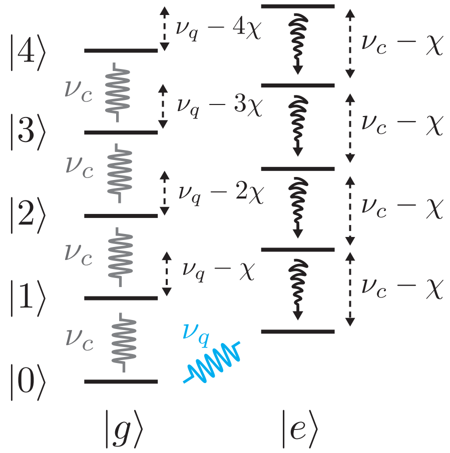

Figure 3.4: Scheme of the cooling of a qubit by reservoir engineering following Ref. [96]. Two continuous waves at the qubit frequency ν_q and at cavity frequency ν_c are applied. These fields induce transitions respectively only when the cavity is in the vacuum and when the qubit is in the ground state.

Autonomous feedback can also be used to cool down a qubit without resorting to measurement feedback as in section 3.1.2. In Ref. [97], we have used such a protocol to cool down a qubit before each experiment. This protocol, first demonstrated in Ref. [96], uses the cavity as the quantum system performing the reset on the qubit. Under the effect of two control fields (see Fig. 3.4), the qubit/cavity system relaxes into the state $|g\rangle \otimes |\alpha\rangle$, where $|\alpha\rangle$ is the stationary coherent state in the cavity under excitation at ν_c. Thermal excitations of the qubit are countered by the fast relaxation of the cavity when the qubit is in the excited state. In the experiments reported in Ref. [97], this protocol allowed us to cool down the qubit from 30% excitations to 10% excitations.

3.3 What's next?

More and more experiments on circuit-QED use quantum feedback control now. In 2013, measurement based feedback was used to deterministically reach a given entangled state between two qubits [98], and to perform teleportation [99], and earlier this year, measurement based feedback was used to correct for the dephasing induced by measurement in real time [100]. On the side of autonomous feedback, an entangled state between two qubits was stabilized last year in circuit-QED [101] and in ion traps [102]. Autonomous feedback can also be a way to interpret complex quantum networks as has been demonstrated with superconducting circuits and mechanical resonators [103, 104].

Another exciting prospect for quantum control is the quantum Zeno blockade. It is a kind of autonomous feedback for which the qubit is used to tailor dynamically the Hamiltonian of a harmonic oscillator. It consists in measuring repeatedly whether or not a cavity has N photons (where N can be chosen freely). By Zeno effect, the cavity is then fixed into either state $|N\rangle$ or the subspace orthogonal to $|N\rangle$ [105, 106]. In Ref. [107], the coherent dynamics of a 51-level atom blocked by Zeno effect was explored. We are currently seeing a very similar dynamics in a circuit-QED architecture.

As a final note, we see now two promising and fascinating quantum error correction schemes using superconducting circuits. A first approach, actively pursued by the UCSB group [108, 109] and by IBM Yorktown[110, 111], consists in using thousands to millions of physical qubits in order to create one protected qubit using surface codes. Another approach, actively pursued by the Yale groups, consists in using protected Schrdinger cats of the field inside of a cavity as a computational basis [82]. In this picture, one logical qubit is encoded in a single mode of a field, which is much simpler to achieve technically. It seems to me that this second approach, if fully validated, is much more attractive, certainly in large parts because it remains a project that is accessible to a small research group. I'm very curious to see what will emerge as the first scalable protected quantum bit in the near future.

Chapter 4

Quantum measurement with past and future information

Quantum measurement theory aims at predicting the statistics of results found when measuring a quantity on many realizations of a quantum system in a given state. The state of the system is defined here by the recipe of everything that happened to the system before the measurement occurs at time t. It is described most efficiently by a density matrix $\rho(t)$. The measurement itself is defined by an ensemble of operators $\{M_m\}$ where m spans all measurement results [5], and such that $\sum_m M_m^\dagger M_m = \mathbf{1}$. The probability to get the outcome m is then simply given by

$$p_m = \mathrm{Tr}(M_m \rho(t) M_m^\dagger). \tag{4.1}$$

Recently, a generalization of quantum measurement theory was proposed in order to include the information on the future of the system [112, 113]. Indeed, on top of assuming a given past $\rho(t)$ for the preparation of a system, one may select only the experiments for which a set of future measurement outcomes will be found. It turns out that the full set of conditions on the future can be efficiently encoded as an effect matrix $E(t)$, which has the same dimension as the density matrix. The probability to get an outcome m then becomes

$$p_m = \frac{1}{\mathcal{N}} \mathrm{Tr}(M_m \rho(t) M_m^\dagger E(t)). \tag{4.2}$$

where $\mathcal{N} = \sum_m \mathrm{Tr}(M_m \rho(t) M_m^\dagger E(t))$ is a normalization factor.

In this chapter, we present an experiment illustrating these new concepts on the simplest open quantum system: a qubit in presence of a relaxation channel. We have measured the average resonance fluorescence signal of a superconducting qubit for various initial states and final measured states.

4.1 Superconducting circuits: a testbed for quantum measurement theory

Before describing in detail our experiment, let us discuss recent experiments on superconducting circuits, which demonstrate properties of measurement theory. Key advantages are offered by superconducting circuits in the prospect of probing quantum measurement theory:

- long coherence times can now be reached with up to 10^4 logical operations per error [2]
- they easily couple to quantum detectors like other qubits or propagating microwave fields
- in circuit-QED, measurements can be repeated (QND).
- the detectors are more and more efficient (see section 1.4.5) so that thousands of bits of information can be extracted within the qubit lifetime [2].

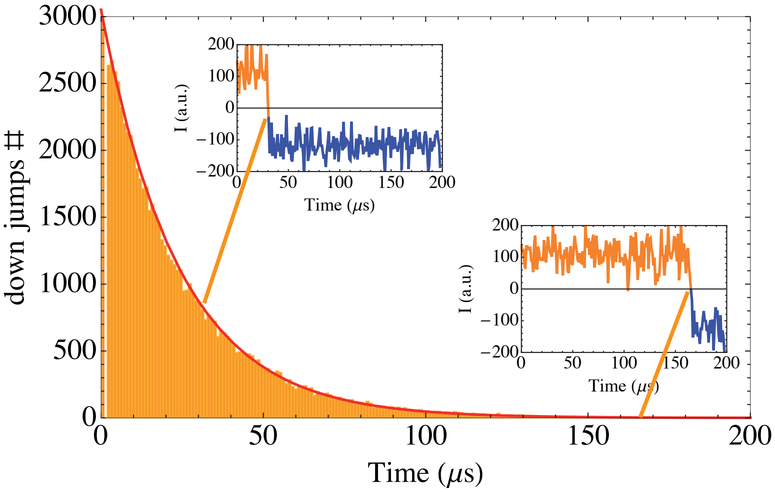

Figure 4.1: Measured histogram of the time before a relaxation event is observed for the qubit presented in Ref. [54]. The relaxation event is identified by the sign change of the I quadrature of the transmitted field through the cavity of the transmon. The red line is an exponentially decreasing function with characteristic time $T_1 = 26\ \mu$s. Insets show two particular measurement records.

A nice illustration of the single shot and QND nature of the measurements in circuit-QED consists in continuously measuring a quantum bit starting in the excited state. At some time, the qubit relaxes which can be seen directly on the time trace of the measurement record. In Fig. 4.1 is shown the histogram of quantum jumps we obtained during one of our experiments on 3D transmons similarly to what was measured in Ref. [114]. Similarly, the discrete loss of photons can be followed in time by measuring the parity of the cavity photon number [115].

Superconducting qubits can be measured with a tunable measurement strength. For strong measurements, the qubit jumps into one of the two eigenstates of the observable. Instead, for weak measurements, only partial information is extracted so that the qubit state evolves by small steps. Interestingly, the measurement back action on the qubit state depends on the detector, and so do the measurement operators M_m. In 2006, Katz and coworkers watched the effect of a detector producing a click with a finite probability when the qubit is excited [116, 117]. The backaction is very different when the probe is one quadrature of the field transmitted through a coupled cavity at its frequency as demonstrated in Ref. [118], and again different when both quadratures are measured simultaneously [16]. In an experiment still in 2013 by Groen and coworkers, another qubit was used as a detector resulting in yet another kind of measurement backaction [119]. In all these experiments, the measurement strength can be tuned in situ. More recently, it was shown that one can track the effect of a joint measurement on a system of two distant qubits [98, 120].

4.2 Fluorescence of a superconducting qubit

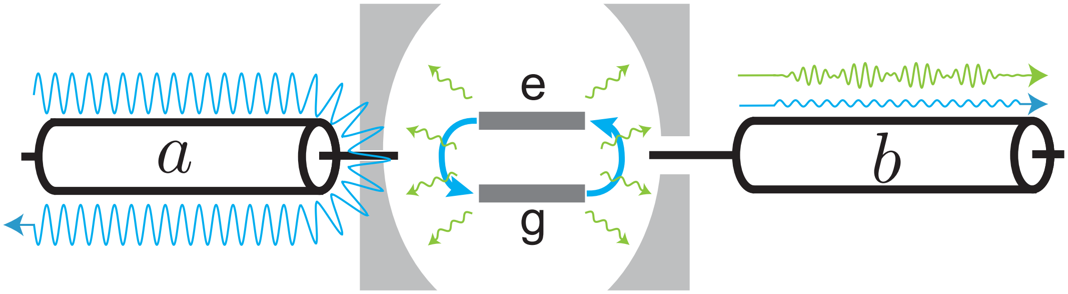

Figure 4.2: Scheme of the fluorescence signal emitted by a superconducting qubit in a cavity. The cavity is out of resonance with the qubit, weakly coupled to the b port, and even more weakly coupled to the a port. When a coherent drive is sent through port a at the qubit frequency ν_q, the qubit endures Rabi oscillations between ground $|g\rangle$ and excited state $|e\rangle$. A field is then reemitted by the qubit on port b, with an imprint of the qubit dynamics.

In our experiment, a superconducting qubit at frequency $\nu_q = 5.19$ GHz is enclosed in a 3D cavity whose first mode is at $\nu_c = 7.76$ GHz (see Fig. 4.2). The cavity is connected to two transmission lines. Line a is coupled as weakly as the internal cavity losses with a rate $\Gamma_a = 2$ kHz. It is used as a channel for resonant driving of the qubit. Since the fundamental cavity mode is far detuned from ν_q, almost all the resonant incoming signal is reflected. The cavity is coupled more strongly to line b, with a rate $\Gamma_b = 0.25$ MHz. When a coherent tone at frequency ν_q is sent through port a, the qubit rotates in the Bloch sphere at the Rabi frequency ν_R. One may then wonder what is the qubit dynamics imprint on the field that is reemitted. Using quantum Langevin equations in a similar model as in Ref. [121], we were able to show that the fluorescence signal can be seen as an oscillation at the Rabi frequency ν_R in both the amplitude and photon number of the outgoing fields. Using Pauli operators $\sigma_z = |e\rangle\langle e| - |g\rangle\langle g|$, $\sigma_x = |g\rangle\langle e| + |e\rangle\langle g|$ and $\sigma_- = |g\rangle\langle e|$, we find that the field amplitudes oscillate as

$$\left\{ \begin{array}{lcl} \langle b_{out}\rangle_{\rho(t)} & = & \langle b_{out}\rangle_0 - \sqrt{\gamma_{1b}}\langle\sigma_-\rangle_{\rho(t)} \\ \langle a_{out}\rangle_{\rho(t)} & = & \langle a_{out}\rangle_0 - \sqrt{\gamma_{1a}}\langle\sigma_-\rangle_{\rho(t)} \end{array} \right. \tag{4.3}$$

whereas the photon rates oscillate as

$$\left\{ \begin{array}{lcl} \langle b_{out}^\dagger b_{out}\rangle_{\rho(t)} & = & \gamma_{1b}\left(1 + \langle\sigma_z\rangle_{\rho(t)}\right)/2 \\ \langle a_{out}^\dagger a_{out}\rangle_{\rho(t)} & = & |a_{in}|^2 + 2\pi\nu_R\langle\sigma_x\rangle_{\rho(t)}/2 \end{array} \right. \tag{4.4}$$

assuming the phase of the drive is such that the qubit evolves in the (x, z) plane, that is, rotates around σ_y. Here, we have introduced the spontaneous emission rates $\gamma_{1a} \ll \gamma_{1b} \approx (0.1\text{ ms})^{-1}$ into line a (or b) set by the Purcell effect in the cavity. Interestingly, we remark that the stimulated emission goes entirely into line a (where the drive field is incoming) while the spontaneous emission goes mostly into line b (which is more open than a). In the experiment, we chose to perform a homodyne measurement of mode b_{out}. Experimentally, we could subtract the qubit independent term $\langle b_{out}\rangle_0$, which mostly comes from a leak of the drive through the cavity. Besides, since the qubit rotates around σ_y (this can be chosen freely as long as the phase of the drive does not vary in time), only one quadrature of the heterodyne measurement oscillates in time. We hence define the fluorescence signal $s_-(t)$ as the measurement outcome of the observable $\mathrm{Re}\left(\langle b_{out}\rangle_0 - b_{out}\right)/\sqrt{\gamma_{1b}}$ at time t. Given Eq. (4.3), one gets that

$$\overline{s_-(t)} = \mathrm{Re}\left(\langle\sigma_-\rangle_{\rho(t)}\right) = \frac{1}{2}\langle\sigma_x\rangle_{\rho(t)}. \tag{4.5}$$

4.3 Past and future information

4.3.1 Past information

The evolution of the qubit density matrix in presence of a relaxation channel is captured by the master equation

$$\frac{d\rho}{dt} = -\frac{i}{\hbar}[H, \rho] + \gamma_1\left(\sigma_-\rho\sigma_+ - \frac{1}{2}\left[\sigma_+\sigma_-\rho + \rho\sigma_+\sigma_-\right]\right). \tag{4.6}$$

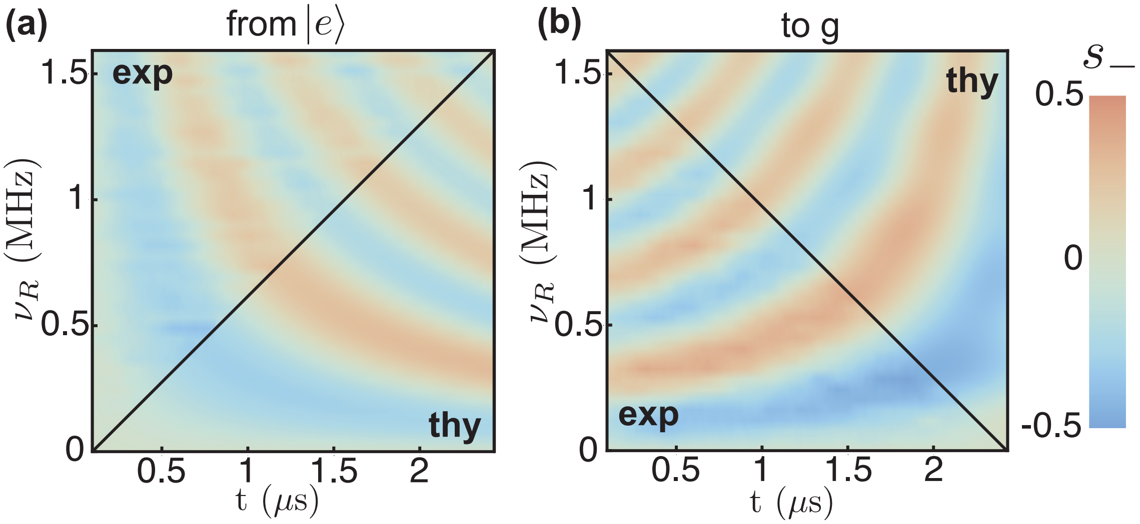

Figure 4.3: Average value of the fluorescence signal s_- as a function of both time and Rabi frequency (tuned by varying the drive amplitude), for a qubit either prepared in $|e\rangle$ (a) or post-selected in g (b). Both measured and predicted averages of s_- are shown in separate regions. Absolute values remain well bellow 0.5, as expected for the measurement of $\mathrm{Re}\left[\langle\sigma_-\rangle\right] = \langle\sigma_x\rangle/2$.

The first term describes the Hamiltonian evolution of the qubit in presence of a drive, with $H = h\nu_q\sigma_z/2 + h\nu_R\sigma_y/2$. The second term takes into account relaxation with a rate $\gamma_1 = (16\ \mu\mathrm{s})^{-1}$, part of which is due to the spontaneous emission rate γ_{1b} introduced in Eq. (4.3). This is rather usual and allows to predict the average signal fluorescence $\overline{s_-(t)}$ over time for a given initial qubit state $\rho(0)$. In Fig. 4.3a, one finds a good agreement between the measured average fluorescence and the prediction for $\langle\sigma_x\rangle_{\rho(t)}/2$ coming from the master equation (4.6).

4.3.2 Future information

Decoherence leads to a continuous increase of the qubit entropy, which diminishes the contrast of the oscillations. Which set of experiments do one has to consider in order to get the time-symmetric version of the oscillations shown in Fig. 4.3a for the average fluorescence signal? Up to now, we only considered information about the system at times smaller than the measurement time t and assumed nothing on the future. Let us now reciprocally assume nothing about the past but something about the future. We prepare the qubit at time 0 in the most entropic state by performing half the experiments in the equilibrium state at time 0 and the other half with a fast π pulse at time 0. Then, at a final time $T = 2.5\ \mu$s, we measure the qubit in a single shot manner along σ_z and select only the experiments indicating that the qubit is in the ground state at time T. The resulting average fluorescence signal is then indeed time-symmetric to the former experiment as can be seen on Fig. 4.3b. In particular, the contrast of the oscillations increases with time.

Using the formalism developed in Refs. [122, 112, 113], one can model the information about the future as an operator $E(t)$ evolving according to a master equation similar but different from (4.6).

$$\frac{dE}{dt} = -\frac{i}{\hbar}\left[H, E\right] - \gamma_1\left(\sigma_+ E\sigma_- - \frac{1}{2}\left[\sigma_+\sigma_- E + E\sigma_+\sigma_-\right]\right). \tag{4.7}$$

The information about ending up in the ground state at time T is simply described by the boundary condition $E(T) = (1 - p_T)|g\rangle\langle g| + p_T|e\rangle\langle e|$, where $p_T \ll 1$ takes into account the imperfection of the final measurement. Then, using Eq. (4.2) in the case where $\rho(t) = \mathbf{1}/2$, one gets the following prediction for the fluorescence signal

$$\overline{s_-(t)} = \mathrm{Tr}\left[E(t)\sigma_-\right]/\mathrm{Tr}\left[E(t)\right] \text{ if } \rho(t) = \mathbf{1}/2. \tag{4.8}$$

As can be seen on Fig. 4.3b, the agreement between measurement and theory is very good indeed.

4.3.3 Past and future information

How are time traces of fluorescence modified when using knowledge of both past and future? The conditional average of the fluorescence signal is represented on Fig. 4.4 for both a preparation in excited state (as in Fig. 4.3d) and a postselection in ground state (as in Fig. 4.3e). This fluorescence signal, which probes the weak values $\langle\sigma_-\rangle_w$, is dramatically changed. Schematically, Fig. 4.4a exhibits interferences between the oscillations of Fig. 4.3d and of Fig. 4.3e, with the appearance of negative (blue) and positive (red) pockets. There are times t and Rabi frequencies ν_R in these pockets for which the weak values go beyond the conventional range of unconditional averages, set by $|\mathrm{Re}(\langle\sigma_-\rangle)| \leq 1/2$. In Fig. 4.4, plain lines represent the contours within which this boundary is violated. Quantitatively, the largest weak value we could obtain is 2.6 times larger than the unconditional average. This purely quantum effect, first predicted in 1988 [123] and observed already in quantum optics in 1991 [124], is a complementary evidence to the irrelevancy of macro realism [125, 126]. In superconducting circuits, out of bound weak values have already been demonstrated in connection with the Leggett-Garg inequalities [127] on the autocorrelation spectrum of $\sigma_z(t)$ [51] and for discrete weak measurements performed by another artificial atom [119].

Special features develop when past and future information disagree, which is for Rabi frequencies such that the qubit rotates by an even amount of π in a time T (Fig. 4.4). There, the weak values go to zero but a small shift in Rabi frequency results in a dramatic change of the signal as evidenced in Fig. 4.4b, where the weak value of the fluorescence

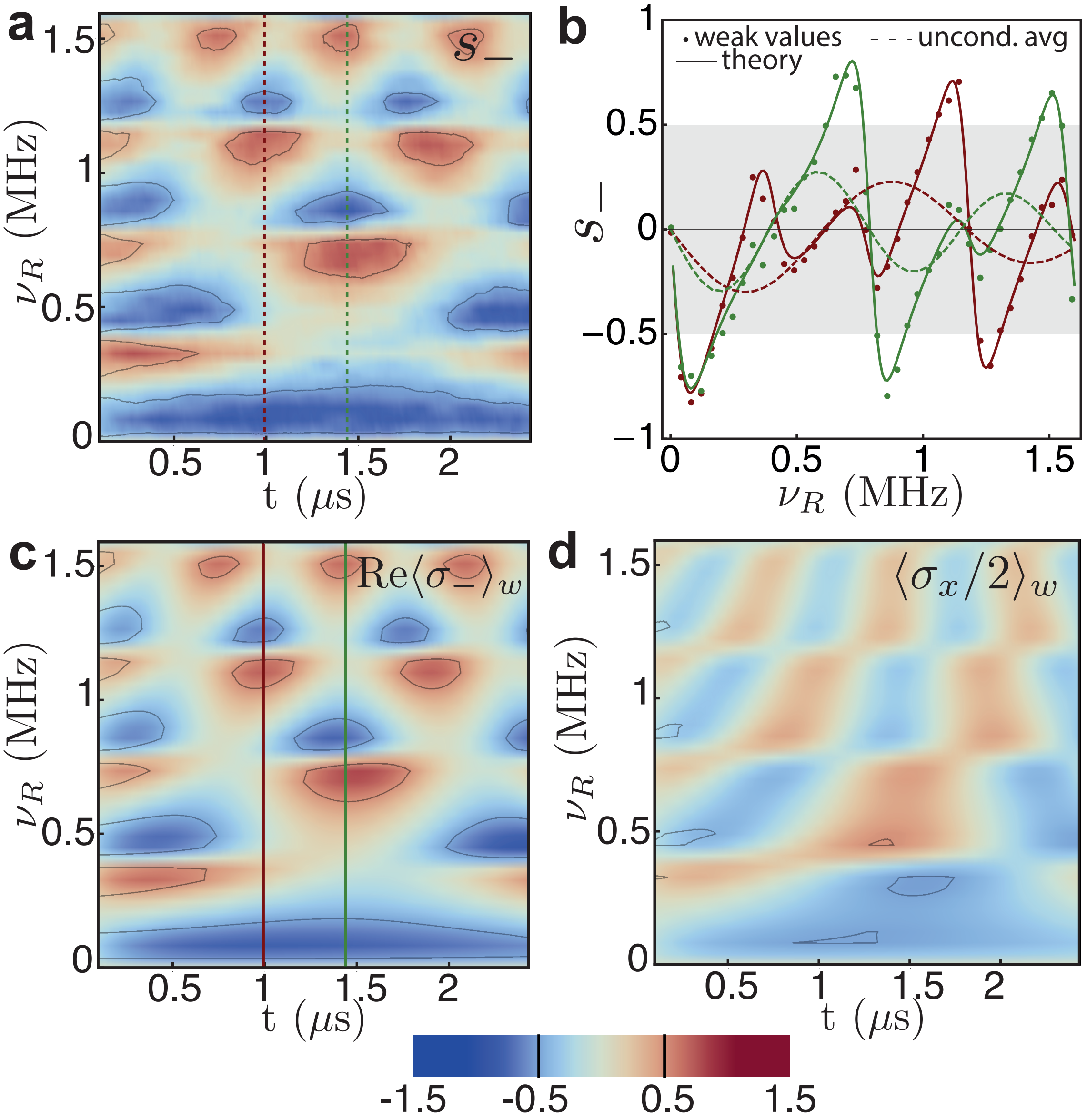

Figure 4.4: **Interferences between past and future states.** **a,** Average value of the measured fluorescence signal s_- as a function of both time and Rabi frequency, for a qubit prepared in $|e\rangle$ and post-selected in $|g\rangle$. Plain lines surround regions with weak values beyond the range allowed by macro realism. **b,** Dots: cuts of **a** as a function of ν_R for times $t = 0.99$ μs (green) and $t = 1.44$ μs (red). Plain lines: prediction for the same curves using Eq (4.9). Dashed lines: cuts of Fig. 4.3d at the same times. The gray region delimits the range of possible unconditional average values, like the contours in (a). **c,** Theoretical counterpart of **a** assuming that the average of s_- is a measure of $\mathrm{Re}(\langle\sigma_-\rangle_w)$ and using Eq. 4.9. **d,** Theoretical counterpart of **a** assuming that the average of s_- is a measure of $\langle\mathrm{Re}\sigma_-\rangle_w)$.

signal is shown as dots as a function of ν_R at times $t = 0.99$ μs and $t = 1.44$ μs. At the sign change, the slope of the weak value is much stiffer than the one of the unconditional signal (dashed line), which illustrates the amplifying abilities of weak values [128, 129]. Indeed, this could be used for better parameter estimation or even feedback in case of the stabilization of a drive amplitude. For instance, this curve was the most sensitive way to determine the measurement fidelity in the experiment.

The conditional average of fluorescence signals can be quantitatively understood using the same formalism as described above. The weak value for σ_- at any time t can indeed be obtained from the operators $\rho(t)$ from the past and $E(t)$ from the future, and is given by [122, 112, 113].

$$\langle\sigma_-\rangle_w = \mathrm{Tr}(\tilde{\rho}\sigma_-), \text{ where } \tilde{\rho}(t) = \frac{\rho(t)E(t)}{\mathrm{Tr}(\rho(t)E(t))}. \tag{4.9}$$

The experiment offers a quantitative test of this simple expression, since the post-selected fluorescence signal is given by $\mathrm{Re}(\langle\sigma_-\rangle_w)$. As can be seen on Fig. 4.4b, the resulting prediction (plain lines) agrees well with the data (dots). The agreement is good for all measurements as can be seen between Figs. 4.4a and 4.4c where both prediction and measurements are compared as a function of time t and Rabi frequency ν_R. The predicted contours surrounding the regions where macro realism is violated are represented as plain lines and they indeed match well their experimental counterpart. The agreement was excellent for any conditions we considered on preparation and post-selection [97].

Interestingly, the operator σ_- probed by the conditional averaged s_- is not an observable as it is not hermitian. This illustrates the ability of weak values to probe complex quantities [130]. Here, the measured observable leading to s_- is the field quadrature $\mathrm{Re}(b_{out}) = (b_{out}^\dagger + b_{out})/2$. For averages prepared only or post-selected only, Eq. (4.3) leads to $\overline{s_-} = \mathrm{Re}\langle\sigma_-\rangle$ or $\overline{s_-} = \langle\mathrm{Re}\sigma_-\rangle = \langle\sigma_x/2\rangle$, which are formally identical. This is not the case anymore for pre and post-selected measurements for which $\mathrm{Re}\langle\sigma_-\rangle_w$ and $\langle\sigma_x/2\rangle_w$ differ and indeed give very different predictions as can be seen in Figs 4.4c and 4.4d. It is clear that the experiment matches only the prediction associated with $\mathrm{Re}\langle\sigma_-\rangle_w$, which cannot be interpreted as the weak value of the observable $\sigma_x/2$.

Perspectives

Superconducting circuits and microwave fields are amazingly controllable systems. We now have a large set of tools to pursue various projects I find particularly interesting.

First, we need to find a way to implement quantum error correction with these systems. As discussed at the end of section 3, I'm very excited about the possibility of encoding and protecting quantum information using superpositions of Schrödingier cat states of a microwave mode. I believe that the quantum node we have developed will be a great tool for that purpose and I think it makes sense to go in this direction.

Our systems are also good candidates to explore the fascinating link between information and energy. We can perform enlightening thought experiments illustrating thermodynamics of quantum information with superconducting circuits. For instance, we are working on the implementation of a quantum version of the Maxwell demon using qubits and cavities. The link between work and entanglement should also be possible to explore. Another interesting aspect concerns the statistics of measured quantum trajectories using close to unit efficiency quantum detectors.

On a broad picture, I think that superconducting circuits and microwave signals will soon prove to be the best quantum processor for any local operations but not for operations on a distance, due to the large attenuation of microwave signals in cables. We need to find a good way to convert efficiently and rapidly quantum information encoded in these systems into quantum information encoded on traveling light in optical fibers. A lot of groups show promising results in this direction using mechanical oscillators as an interface and I'm excited to see these devices coming to life.

Bibliography

[1] Y. Nakamura, Y. A. Pashkin and J. S. Tsai. Coherent control of macroscopic quantum states in a single-Cooper-pair box. Nature **398**, 786–788 (1999).

[2] M. H. Devoret and R. J. Schoelkopf. Superconducting circuits for quantum information: an outlook. Science (New York, N.Y.) **339**, 1169–74 (2013).

[3] G. Chiribella, G. D'Ariano and P. Perinotti. Informational derivation of quantum theory. Phys. Rev. A **84**, 012311 (2011).

[4] Zurek. Decoherence, einselection, and the quantum origins of the classical. Reviews of Modern Physics **75**, 715–775 (2003).

[5] S. Haroche and J. Raimond. Exploring the Quantum: Atoms, Cavities, and Photons. Oxford Graduated Text 616 (2006).

[6] R. J. Schoelkopf and S. M. Girvin. Wiring up quantum systems. Nature **451**, 664–9 (2008).

[7] Z.-L. Xiang, S. Ashhab, J. Q. You and F. Nori. Hybrid quantum circuits: Superconducting circuits interacting with other quantum systems. Reviews of Modern Physics **85**, 623–653 (2013).

[8] A. A. Clerk, M. H. Devoret, S. M. Girvin, F. Marquardt and R. J. Schoelkopf. Introduction to quantum noise, measurement, and amplification. Reviews of Modern Physics **82**, 1155–1208 (2010).

[9] G. Y. Xiang, T. C. Ralph, A. P. Lund, N. Walk and G. J. Pryde. Heralded noiseless linear amplification and distillation of entanglement. Nature Photonics **4**, 316–319 (2010).

[10] H. A. Haus and J. A. Mullen. Quantum Noise in Linear Amplifiers. Physical Review **128**, 2407 (1962).

[11] C. M. Caves. Quantum limits on noise in linear amplifiers. Physical Review D **26**, 1817 (1982).

[12] E. Arthurs and J. L. Kelly. On simultaneous measurement of a pair of conjugate observables. Bell System Technical Journal, **44**, 725 (1965).

[13] S. L. Braunstein, C. M. Caves and G. J. Milburn. Interpretation for a positive P representation. Physical Review A **43**, 1153–1159 (1991).

[14] U. Leonhardt and H. Paul. Phase measurement and Q function. Physical Review A **47**, 2460–2463 (1993).

[15] C. Eichler, D. Bozyigit and A. Wallraff. Characterizing quantum microwave radiation and its entanglement with superconducting qubits using linear detectors. Physical Review A **86**, 032106 (2012).

[16] M. Hatridge, S. Shankar, Mirrahimi, F. Schackert, K. Geerlings, T. Brecht, K. Sliwa, B. Abdo, L. Frunzio, Girvin, Schoelkopf and M. Devoret. Quantum Back-Action of an Individual Variable-Strength Measurement. Science **339**, 178–181 (2013).

[17] M. Tinkham. Introduction to Superconductivity (Vol I) (Dover Books on Physics, 2004).

[18] D. Mattis and J. Bardeen. Theory of the Anomalous Skin Effect in Normal and Superconducting Metals. Physical Review **111**, 412–417 (1958).

[19] A. Palacios-Laloy. Superconducting qubit in a resonator: test of the Leggett-Garg inequality and si
Ph.D. thesis, Université Pierre et Marie Curie, Paris 6, CEA Saclay (2010).

[20] B. Yurke, L. R. Corruccini, P. G. Kaminsky, L. W. Rupp, A. D. Smith, A. H. Silver, R. W. Simon and E. A. Whittaker. Observation of parametric amplification and deamplification in a Josephson parametric amplifier. Physical Review A **39**, 2519 (1989).

[21] C. M. Caves, J. Combes, Z. Jiang and S. Pandey. Quantum limits on phase-preserving linear amplifiers. Physical Review A **86**, 063802 (2012).

[22] D. Walls and G. J. Milburn. Quantum Optics (Springer, 2008).

[23] M. A. Castellanos-Beltran and K. W. Lehnert. Widely tunable parametric amplifier based on a superconducting quantum interference device array resonator. Applied Physics Letters **91**, 083509 (2007).

[24] M. A. Castellanos-Beltran, K. D. Irwin, G. C. Hilton, L. R. Vale and K. W. Lehnert. Amplification and squeezing of quantum noise with a tunable Josephson metamaterial. Nature Physics **4**, 929–931 (2008).

[25] C. M. Wilson, T. Duty, M. Sandberg, F. Persson, V. Shumeiko and P. Delsing. Photon Generation in an Electromagnetic Cavity with a Time-Dependent Boundary. Physical Review Letters **105**, 233907 (2010).

[26] M. Hatridge, R. Vijay, D. H. Slichter, J. Clarke and I. Siddiqi. Dispersive magnetometry with a quantum limited SQUID parametric amplifier. Physical Review B **83**, 134501 (2011).

[27] C. Eichler, D. Bozyigit, C. Lang, M. Baur, L. Steffen, J. M. Fink, S. Filipp and A. Wallraff. Observation of Two-Mode Squeezing in the Microwave Frequency Domain. Physical Review Letters **107**, 113601 (2011).

[28] E. A. Tholén, A. Ergül, K. Stannigel, C. Hutter and D. B. Haviland. Parametric amplification with weak-link nonlinearity in superconducting microresonators. Physica Scripta **T137**, 014019 (2009).

[29] E. a. Tholen, A. Ergul, E. M. Doherty, F. M. Weber, F. Gregis and D. B. Haviland. Nonlinearities and parametric amplification in superconducting coplanar waveguide resonators. Applied Physics Letters **90**, 253509 (2007).

[30] B. Ho Eom, P. K. Day, H. G. LeDuc and J. Zmuidzinas. A wideband, low-noise superconducting amplifier with high dynamic range. Nature Physics **8**, 623–627 (2012).

[31] T. Yamamoto, K. Inomata, M. Watanabe, K. Matsuba, T. Miyazaki, W. D. Oliver, Y. Nakamura and J. S. Tsai. Flux-driven Josephson parametric amplifier. Applied Physics Letters **93**, 042510 (2008).

[32] M. Muck, M.-O. Andre, J. Clarke, J. Gail and C. Heiden. Radio-frequency amplifier based on a niobium dc superconducting quantum interference device with microstrip input coupling. Applied Physics Letters **72**, 2885 (1998).

[33] D. Kinion and J. Clarke. Microstrip superconducting quantum interference device radio-frequency amplifier: Scattering parameters and input coupling. Applied Physics Letters **92**, 172503 (2008).

[34] L. Spietz, K. Irwin, M. Lee and J. Aumentado. Noise performance of lumped element direct current superconducting quantum interference device amplifiers in the 48 GHz range. Applied Physics Letters **97**, 142502 (2010).

[35] D. Hover, Y.-F. Chen, G. J. Ribeill, S. Zhu, S. Sendelbach and R. McDermott. Superconducting low-inductance undulatory galvanometer microwave amplifier. Applied Physics Letters **100**, 063503 (2012).

[36] N. Bergeal, R. Vijay, V. E. Manucharyan, I. Siddiqi, R. J. Schoelkopf, S. M. Girvin and M. H. Devoret. Analog information processing at the quantum limit with a Josephson ring modulator. Nature Physics **6**, 296–302 (2010).

[37] N. Bergeal, F. Schackert, M. Metcalfe, R. Vijay, V. E. Manucharyan, L. Frunzio, D. E. Prober, R. J. Schoelkopf, S. M. Girvin and M. H. Devoret. Phase-preserving amplification near the quantum limit with a Josephson ring modulator. Nature **465**, 64 (2010).

[38] M. Devoret, B. Huard, N. Bergeal, R. J. Schoelkopf and S. M. Girvin. Amplifying quantum signals with Josephson tunnel junction circuits. In B. Deveaud-Plédran, A. Quattropani and P. Schwendimann (eds.) Proceedings of the International School of Physics "Enrico Fermi", Volume 171, 151 (Quantum Coherence in Solid State Systems, 2009).

[39] A. Kamal, A. Marblestone and M. Devoret. Signal-to-pump back action and self-oscillation in double-pump Josephson parametric amplifier. Physical Review B **79**, 184301 (2009).

[40] I. Siddiqi, R. Vijay, F. Pierre, C. M. Wilson, M. Metcalfe, C. Rigetti, L. Frunzio and M. H. Devoret. RF-Driven Josephson Bifurcation Amplifier for Quantum Measurement. Physical Review Letters **93**, 207002 (2004).

[41] I. Siddiqi, R. Vijay, F. Pierre, C. Wilson, L. Frunzio, M. Metcalfe, C. Rigetti, R. Schoelkopf, M. Devoret, D. Vion and D. Esteve. Direct Observation of Dynamical Bifurcation between Two Driven Oscillation States of a Josephson Junction. Physical Review Letters **94**, 027005 (2005).

[42] R. Vijay, M. H. Devoret and I. Siddiqi. Invited review article: The Josephson bifurcation amplifier. The Review of scientific instruments **80**, 111101 (2009).

[43] F. Mallet, F. R. Ong, A. Palacios-Laloy, F. Nguyen, P. Bertet, D. Vion and D. Esteve. Single-shot qubit readout in circuit quantum electrodynamics. Nature Physics **5**, 791–795 (2009).

[44] Ong, Boissonneault, Mallet, Palacios-Laloy, A. Dewes, Doherty, Blais, Bertet, Vion and Esteve. Circuit QED with a Nonlinear Resonator: ac-Stark Shift and Dephasing. Physical Review Letters **106**, 167002 (2011).

[45] N. Roch, E. Flurin, F. Nguyen, P. Morfin, P. Campagne-Ibarcq, M. H. Devoret and B. Huard. Widely Tunable, Nondegenerate Three-Wave Mixing Microwave Device Operating near the Quantum Limit. Physical Review Letters **108**, 147701 (2012).

[46] B. Abdo, F. Schackert, M. Hatridge, C. Rigetti and M. Devoret. Josephson amplifier for qubit readout. Applied Physics Letters **99**, 162506 (2011).

[47] B. Abdo, A. Kamal and M. Devoret. Nondegenerate three-wave mixing with the Josephson ring modulator. Physical Review B **87**, 014508 (2013).

[48] B. Abdo, K. Sliwa, F. Schackert, N. Bergeal, M. Hatridge, L. Frunzio, A. D. Stone and M. Devoret. Full Coherent Frequency Conversion between Two Propagating Microwave Modes. Physical Review Letters **110**, 173902 (2013).

[49] V. Manucharyan, E. Boaknin, M. Metcalfe, R. Vijay, I. Siddiqi and M. Devoret. Microwave bifurcation of a Josephson junction: Embedding-circuit requirements. Physical Review B **76**, 014524 (2007).

[50] E. Flurin, N. Roch, J.-D. Pillet, F. Mallet and B. Huard. Superconducting quantum node for entanglement and storage of microwave radiation. arXiv:1401.5622 (2014).

[51] A. Palacios-laloy, F. Mallet, F. Nguyen, P. Bertet, D. Vion, D. Esteve and A. N. Korotkov. Experimental violation of a Bells inequality in time with weak measurement. Nature Physics **6**, 442–447 (2010).

[52] C. Eichler and A. Wallraff. Controlling the dynamic range of a Josephson parametric amplifier. EPJ Quantum Technology **1**, 2 (2014).

[53] E. Flurin, N. Roch, F. Mallet, M. H. Devoret and B. Huard. Generating Entangled Microwave Radiation Over Two Transmission Lines. Physical Review Letters **109**, 183901 (2012).

[54] P. Campagne-Ibarcq, E. Flurin, N. Roch, D. Darson, P. Morfin, M. Mirrahimi, M. H. Devoret, F. Mallet and B. Huard. Persistent Control of a Superconducting Qubit by Stroboscopic Measurement Feedback. Physical Review X **3**, 021008 (2013).

[55] S. Weinreb, M. Pospieszalski and R. Norrod. Cryogenic, HEMT, low-noise receivers for 1.3 to 43 GHz range. In 1988., IEEE MTT-S International Microwave Symposium Digest, 945–948 (IEEE, 1988).

[56] S. L. Braunstein and P. van Loock. Quantum information with continuous variables. Reviews of Modern Physics **77**, 513–577 (2005).

[57] B. Yurke, P. G. Kaminsky, R. E. Miller, E. A. Whittaker, A. D. Smith, A. H. Silver and R. W. Simon. Observation of 4.2-K equilibrium-noise squeezing via a Josephson-parametric amplifier. Physical Review Letters **60**, 764 (1988).

[58] Mallet, Castellanos-Beltran, Ku, Glancy, E. Knill, Irwin, Hilton, Vale and Lehnert. Quantum State Tomography of an Itinerant Squeezed Microwave Field. Physical Review Letters **106**, 220502 (2011).

[59] C. M. Wilson, G. Johansson, A. Pourkabirian, M. Simoen, J. Johansson, T. Duty, F. Nori and P. Delsing. Observation of the dynamical Casimir effect in a superconducting circuit. Nature **479**, 376–379 (2012).

[60] E. P. Menzel, R. Di Candia, F. Deppe, P. Eder, L. Zhong, M. Ihmig, M. Haeberlein, A. Baust, E. Hoffmann, D. Ballester, K. Inomata, T. Yamamoto, Y. Nakamura, E. Solano, A. Marx and R. Gross. Path Entanglement of Continuous-Variable Quantum Microwaves. Physical Review Letters **109**, 250502 (2012).

[61] W. Wan, Y. Chong, L. Ge, H. Noh, A. D. Stone and H. Cao. Time-reversed lasing and interferometric control of absorption. Science (New York, N.Y.) **331**, 889–92 (2011).

[62] F. Schackert, A. Roy, M. Hatridge, M. H. Devoret and A. D. Stone. Three-Wave Mixing with Three Incoming Waves: Signal-Idler Coherent Attenuation and Gain Enhancement in a Parametric Amplifier. Physical Review Letters **111**, 073903 (2013).

[63] J. Kong, F. Hudelist, Z. Y. Ou and W. Zhang. Cancellation of Internal Quantum Noise of an Amplifier by Quantum Correlation. Physical Review Letters **111**, 033608 (2013).

[64] J. Cirac, P. Zoller, H. Kimble and H. Mabuchi. Quantum State Transfer and Entanglement Distribution among Distant Nodes in a Quantum Network. Physical Review Letters **78**, 3221–3224 (1997).

[65] H. J. Kimble. The quantum internet. Nature **453**, 1023–30 (2008).

[66] H. Wu, R. E. George, J. H. Wesenberg, K. Mø lmer, D. I. Schuster, R. J. Schoelkopf, K. M. Itoh, A. Ardavan, J. J. L. Morton and G. A. D. Briggs. Storage of Multiple Coherent Microwave Excitations in an Electron Spin Ensemble. Physical Review Letters **105**, 140503 (2010).

[67] Y. Kubo, I. Diniz, a. Dewes, V. Jacques, a. Dréau, J.-F. Roch, a. Auffeves, D. Vion, D. Esteve and P. Bertet. Storage and retrieval of a microwave field in a spin ensemble. Physical Review A **85**, 012333 (2012).

[68] S. Saito, X. Zhu, R. Amsüss, Y. Matsuzaki, K. Kakuyanagi, T. Shimo-Oka, N. Mizuochi, K. Nemoto, W. J. Munro and K. Semba. Towards Realizing a Quantum Memory for a Superconducting Qubit: Storage and Retrieval of Quantum States. Physical Review Letters **111**, 107008 (2013).

[69] Y. Yin, Y. Chen, D. Sank, P. J. J. OMalley, T. C. White, R. Barends, J. Kelly, E. Lucero, M. Mariantoni, A. Megrant, C. Neill, A. Vainsencher, J. Wenner, A. N. Korotkov, A. N. Cleland and J. M. Martinis. Catch and Release of Microwave Photon States. Physical Review Letters **110**, 107001 (2013).

[70] J. Wenner, Y. Yin, Y. Chen and R. Barends. Catching Shaped Microwave Photons with 99.4% Absorption Efficiency. arXiv:1311.1180 (2013).

[71] T. a. Palomaki, J. W. Harlow, J. D. Teufel, R. W. Simmonds and K. W. Lehnert. Coherent state transfer between itinerant microwave fields and a mechanical oscillator. Nature **495**, 210–4 (2013).

[72] T. a. Palomaki, J. D. Teufel, R. W. Simmonds and K. W. Lehnert. Entangling Mechanical Motion with Microwave Fields. Science (New York, N.Y.) **710** (2013).

[73] M. Reagor, H. Paik, G. Catelani, L. Sun, C. Axline, E. Holland, I. M. Pop, N. a. Masluk, T. Brecht, L. Frunzio, M. H. Devoret, L. Glazman and R. J. Schoelkopf. Reaching 10ms single photon lifetimes for superconducting aluminum cavities. Applied Physics Letters **102**, 192604 (2013).

[74] M. Pechal, C. Eichler, S. Zeytinoglu, S. Berger, A. Wallraff and S. Filipp. Microwave-controlled generation of shaped single photons in circuit quantum electrodynamics. arxiv:1308.4094 (2013).

[75] H. Paik, D. I. Schuster, L. S. Bishop, G. Kirchmair, G. Catelani, a. P. Sears, B. R. Johnson, M. J. Reagor, L. Frunzio, L. I. Glazman, S. M. Girvin, M. H. Devoret and R. J. Schoelkopf. Observation of High Coherence in Josephson Junction Qubits Measured in a Three-Dimensional Circuit QED Architecture. Physical Review Letters **107**, 240501 (2011).

[76] C. Simon et al. Quantum memories. The European Physical Journal D **58**, 1–22 (2010).

[77] L. Vaidman. Teleportation of quantum states. Phys. Rev. A **49**, 1473 (1993).

[78] S. L. Braunstein and H. J. Kimble. Teleportation of Continuous Quantum Variables. Physical Review Letters **80**, 869–872 (1998).

[79] Furusawa, Sorensen, Braunstein, Fuchs, Kimble and Polzik. Unconditional quantum teleportation. Science **282**, 706–709 (1998).

[80] Takeda, Webb, Huntington and Furusawa. Teleportation of nonclassical wave packets of light. Science (2011).

[81] Z. Leghtas, G. Kirchmair, B. Vlastakis, R. J. Schoelkopf, M. H. Devoret and M. Mirrahimi. Hardware-Efficient Autonomous Quantum Memory Protection. Physical Review Letters **111**, 120501 (2013).

[82] M. Mirrahimi, Z. Leghtas, V. V. Albert, S. Touzard, R. J. Schoelkopf, L. Jiang and M. H. Devoret. Dynamically protected cat-qubits: a new paradigm for universal quantum computation. arxiv:1312.2017 (2013).

[83] P. W. Shor. Scheme for reducing decoherence in quantum computer memory. Physical Review A **52**, R2493–R2496 (1995).

[84] A. Steane. Multiple-Particle Interference and Quantum Error Correction. Proceedings of the Royal Society A: Mathematical, Physical and Engineering Sciences **452**, 2551–2577 (1996).

[85] E. Knill and R. Laflamme. Theory of quantum error-correcting codes. Physical Review A **55**, 900–911 (1997).

[86] D. Gottesman. Stabilizer Codes and Quantum Error Correction. arXiv:quant-ph/9705052 (1997).

[87] H. Mabuchi. Coherent-feedback quantum control with a dynamic compensator. Physical Review A **78**, 32323 (2008).

[88] C. Sayrin, I. Dotsenko, X. Zhou, B. Peaudecerf, T. Rybarczyk, S. Gleyzes, P. Rouchon, M. Mirrahimi, H. Amini, M. Brune, J. Raimond and S. Haroche. Real-time quantum feedback prepares and stabilizes photon number states. Nature **477**, 73–77 (2011).

[89] X. Zhou, I. Dotsenko, B. Peaudecerf, T. Rybarczyk, C. Sayrin, S. Gleyzes, J. M. Raimond, M. Brune and S. Haroche. Field Locked to a Fock State by Quantum Feedback with Single Photon Corrections. Physical Review Letters **108**, 243602 (2012).

[90] B. Peaudecerf, C. Sayrin, X. Zhou, T. Rybarczyk, S. Gleyzes, I. Dotsenko, J. Raimond, M. Brune and S. Haroche. Quantum feedback experiments stabilizing Fock states of light in a cavity. Physical Review A **87**, 042320 (2013).

[91] R. Vijay, C. Macklin, D. H. Slichter, S. J. Weber, K. W. Murch, R. Naik, A. N. Korotkov and I. Siddiqi. Stabilizing Rabi oscillations in a superconducting qubit using quantum feedback. Nature **490**, 77–80 (2012).

[92] M. Mirrahimi, B. Huard and M. Devoret. Strong measurement and quantum feedback for persistent Rabi oscillations in circuit QED experiments. In 2012 IEEE 51st IEEE Conference on Decision and Control (CDC), 3646–3651 (IEEE, 2012).

[93] D. Ristè, C. Bultink, K. Lehnert and L. Dicarlo. Feedback Control of a Solid-State Qubit Using High-Fidelity Projective Measurement. Physical Review Letters **109**, 240502 (2012).

[94] D. Ristè, C. C. Bultink, M. J. Tiggelman, R. N. Schouten, K. W. Lehnert and L. DiCarlo. Millisecond charge-parity fluctuations and induced decoherence in a superconducting transmon qubit. Nature communications **4**, 1913 (2013).

[95] K. W. Murch, U. Vool, D. Zhou, S. J. Weber, S. M. Girvin and I. Siddiqi. Cavity-Assisted Quantum Bath Engineering. Physical Review Letters **109**, 183602 (2012).

[96] K. Geerlings, Z. Leghtas, I. M. Pop, S. Shankar, L. Frunzio, R. J. Schoelkopf, M. Mirrahimi and M. H. Devoret. Demonstrating a Driven Reset Protocol for a Superconducting Qubit. Physical Review Letters **110**, 120501 (2013).

[97] P. Campagne-Ibarcq, L. Bretheau, E. Flurin, A. Auffèves, F. Mallet and B. Huard. Observing interferences between past and future quantum states in resonance fluorescence. arxiv:1311.5605 (2013).

[98] D. Ristè, M. Dukalski, C. a. Watson, G. de Lange, M. J. Tiggelman, Y. M. Blanter, K. W. Lehnert, R. N. Schouten and L. DiCarlo. Deterministic entanglement of superconducting qubits by parity measurement and feedback. Nature **502**, 350–4 (2013).

[99] L. Steffen, Y. Salathe, M. Oppliger, P. Kurpiers, M. Baur, C. Lang, C. Eichler, G. Puebla-Hellmann, a. Fedorov and a. Wallraff. Deterministic quantum teleportation with feed-forward in a solid state system. Nature **500**, 319–22 (2013).

[100] G. de Lange, D. Ristè, M. Tiggelman, C. Eichler, L. Tornberg, G. Johansson, a. Wallraff, R. Schouten and L. DiCarlo. Reversing Quantum Trajectories with Analog Feedback. Physical Review Letters **112**, 080501 (2014).

[101] S. Shankar, M. Hatridge, Z. Leghtas, K. M. Sliwa, A. Narla, U. Vool, S. M. Girvin, L. Frunzio, M. Mirrahimi and M. H. Devoret. Autonomously stabilized entanglement between two superconducting quantum bits. Nature **504**, 419–22 (2013).

[102] Y. Lin, J. P. Gaebler, F. Reiter, T. R. Tan, R. Bowler, A. S. Sø rensen, D. Leibfried and D. J. Wineland. Dissipative production of a maximally entangled steady state of two quantum bits. Nature **504**, 415–8 (2013).

[103] J. Kerckhoff and K. W. Lehnert. Superconducting Microwave Multivibrator Produced by Coherent Feedback. Physical Review Letters **109**, 153602 (2012).

[104] J. Kerckhoff, R. W. Andrews, H. S. Ku, W. F. Kindel, K. Cicak, R. W. Simmonds and K. W. Lehnert. Tunable Coupling to a Mechanical Oscillator Circuit Using a Coherent Feedback Network. Physical Review X **3**, 021013 (2013).

[105] J. M. Raimond, C. Sayrin, S. Gleyzes, I. Dotsenko, M. Brune, S. Haroche, P. Facchi and S. Pascazio. Phase Space Tweezers for Tailoring Cavity Fields by Quantum Zeno Dynamics. Physical Review Letters **105**, 213601 (2010).

[106] J. M. Raimond, P. Facchi, B. Peaudecerf, S. Pascazio, C. Sayrin, I. Dotsenko, S. Gleyzes, M. Brune and S. Haroche. Quantum Zeno dynamics of a field in a cavity. Physical Review A **86**, 032120 (2012).

[107] A. Signoles, A. Facon, D. Grosso, I. Dotsenko, S. Haroche, J.-M. Raimond, M. Brune and S. Gleyzes. Confined quantum Zeno dynamics of a watched atomic arrow. arxiv:1402.0111 (2014).

[108] A. G. Fowler, M. Mariantoni, J. M. Martinis and A. N. Cleland. Surface codes: Towards practical large-scale quantum computation. Physical Review A **86**, 032324 (2012).

[109] R. Barends et al. Logic gates at the surface code threshold: Superconducting qubits poised for fault-tolerant quantum computing. arXiv:1402.4848 (2014).

[110] D. P. DiVincenzo. Fault-tolerant architectures for superconducting qubits. Physica Scripta **T137**, 014020 (2009).

[111] J. M. Chow, J. M. Gambetta, E. Magesan, S. J. Srinivasan, A. W. Cross, D. W. Abraham, N. A. Masluk, B. R. Johnson, C. A. Ryan and M. Steffen. Implementing a strand of a scalable fault-tolerant quantum computing fabric. arXiv:1311.6330 (2013).

[112] M. Tsang. Optimal waveform estimation for classical and quantum systems via time-symmetric smoothing. Physical Review A **80**, 033840 (2009).

[113] S. r. Gammelmark, B. Julsgaard and K. Mø lmer. Past Quantum States of a Monitored System. Physical Review Letters **111**, 160401 (2013).

[114] Vijay, Slichter and Siddiqi. Observation of Quantum Jumps in a Superconducting Artificial Atom. Physical Review Letters **106**, 110502 (2011).

[115] L. Sun, A. Petrenko, Z. Leghtas, B. Vlastakis, G. Kirchmair, K. M. Sliwa, A. Narla, M. Hatridge, S. Shankar, J. Blumoff, L. Frunzio, M. Mirrahimi, M. H. Devoret and R. J. Schoelkopf. Tracking Photon Jumps with Repeated Quantum Non-Demolition Parity Measurements. arxiv:1311.2534 (2013).

[116] N. Katz, M. Ansmann, R. C. Bialczak, E. Lucero, R. McDermott, M. Neeley, M. Steffen, E. M. Weig, a. N. Cleland, J. M. Martinis and a. N. Korotkov. Coherent state evolution in a superconducting qubit from partial-collapse measurement. Science (New York, N.Y.) **312**, 1498–500 (2006).

[117] N. Katz, M. Neeley, M. Ansmann, R. C. Bialczak, M. Hofheinz, E. Lucero, A. O'Connell, H. Wang, A. N. Cleland, J. M. Martinis and A. N. Korotkov. Reversal of the Weak Measurement of a Quantum State in a Superconducting Phase Qubit. Physical Review Letters **101**, 200401 (2008).

[118] K. W. Murch, S. J. Weber, C. Macklin and I. Siddiqi. Observing single quantum trajectories of a superconducting quantum bit. Nature **502**, 211–4 (2013).

[119] J. P. Groen, D. Ristè, L. Tornberg, J. Cramer, P. C. de Groot, T. Picot, G. Johansson and L. DiCarlo. Partial-Measurement Backaction and Nonclassical Weak Values in a Superconducting Circuit. Physical Review Letters **111**, 090506 (2013).

[120] N. Roch, M. E. Schwartz, F. Motzoi, C. Macklin, R. Vijay, A. W. Eddins, A. N. Korotkov, K. B. Whaley, M. Sarovar and I. Siddiqi. Observation of measurement-induced entanglement and quantum trajectories of remote superconducting qubits. arxiv:1402.1868 (2014).

[121] D. Valente, S. Portolan, G. Nogues, J. P. Poizat, M. Richard, J. M. Gérard, M. F. Santos and a. Auffèves. Monitoring stimulated emission at the single-photon level in one-dimensional atoms. Physical Review A **85**, 023811 (2012).

[122] H. Wiseman. Weak values, quantum trajectories, and the cavity-QED experiment on wave-particle correlation. Physical Review A **65**, 032111 (2002).

[123] Y. Aharonov, D. Albert and L. Vaidman. How the result of a measurement of a component of the spin of a spin-1/2 particle can turn out to be 100. Physical Review Letters **60**, 1351–1354 (1988).

[124] N. Ritchie, J. Story and R. Hulet. Realization of a measurement of a weak value. Physical Review Letters **66**, 1107–1110 (1991).

[125] N. Williams and A. Jordan. Weak Values and the Leggett-Garg Inequality in Solid-State Qubits. Physical Review Letters **100**, 026804 (2008).

[126] J. Dressel and A. N. Korotkov. Avoiding loopholes with hybrid Bell-Leggett-Garg inequalities. Physical Review A **89**, 012125 (2014).

[127] C. Emary, N. Lambert and F. Nori. LeggettGarg inequalities. Reports on Progress in Physics **77**, 016001 (2014).

[128] O. Hosten and P. Kwiat. Observation of the spin hall effect of light via weak measurements. Science (New York, N.Y.) **319**, 787–90 (2008).

[129] P. Dixon, D. Starling, A. Jordan and J. Howell. Ultrasensitive Beam Deflection Measurement via Interferometric Weak Value Amplification. Physical Review Letters **102**, 173601 (2009).

[130] J. S. Lundeen, B. Sutherland, A. Patel, C. Stewart and C. Bamber. Direct measurement of the quantum wavefunction. Nature **474**, 188–91 (2011).

[131] K. E. Cahill and R. J. Glauber. Density operators and quasiprobability distributions. Physical Review **177** (1969).

[132] M. Hillery, R. O'connell, M. Scully and E. Wigner. Distribution functions in physics: fundamentals. Physics Reports **106**, 121 (1984).

Appendix A

Some results on linear amplifiers

A.1 Representing mode states

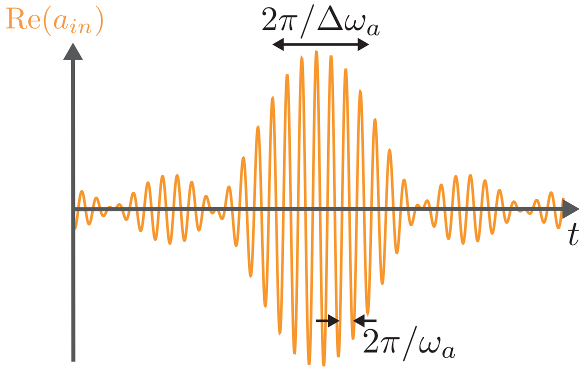

Figure A.1: Propagating mode in the Shannon basis occupied by a coherent state $|\alpha\rangle$. Here, we represent a mode $a_{in}(t) = \langle a_{in}\rangle\sqrt{\frac{\Delta\omega_a}{2\pi}}\mathrm{sinc}[(t - n\Delta t)\Delta\omega_a/2]e^{im\Delta\omega_a t}$

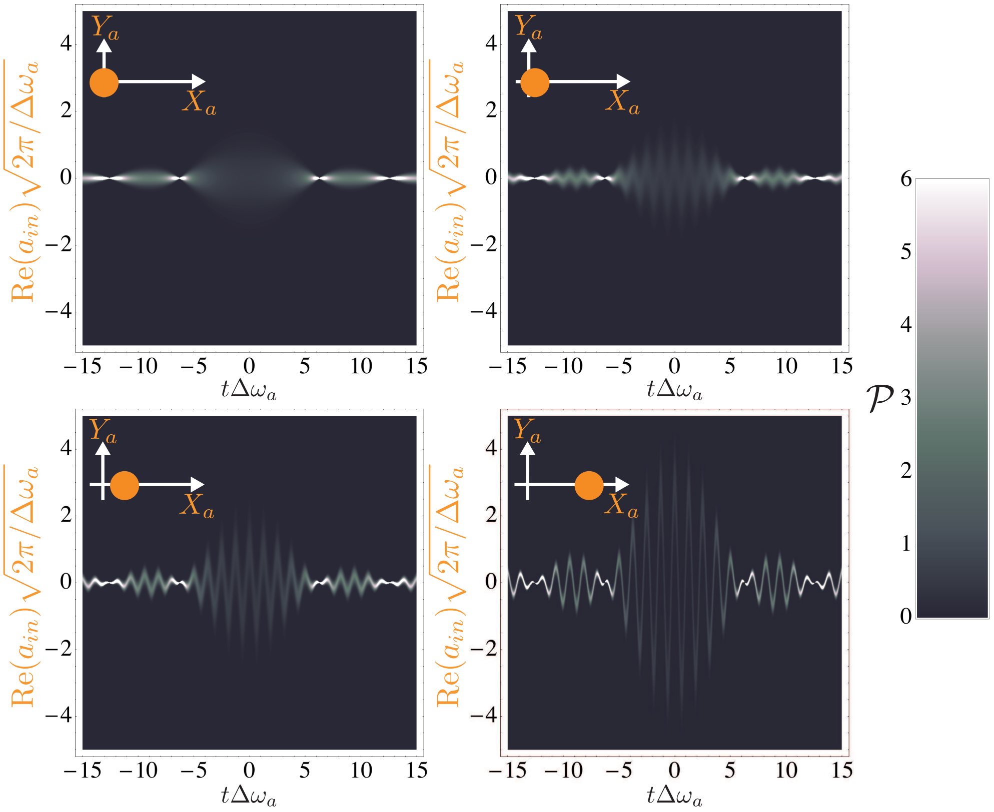

Figure A.2: Probability density $\mathcal{P}$ for the outcomes $\mathrm{Re}(a_{in}(t))$ of a homodyne measurement when the signal is in a coherent state $|\alpha_{in}\rangle$ of the Shannon mode of Fig. A.1. The four panels correspond to coherent states $\alpha_{in} = 0, 0.3, 1$ and 3. The corresponding Wigner function is represented on each panel (see Fig. A.3).

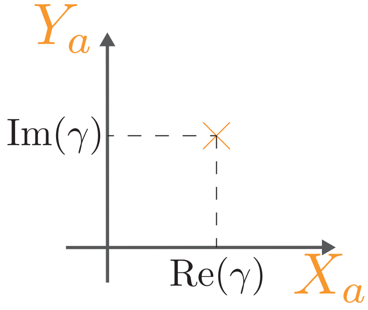

Glauber-Sudarshan P
Coherent state $\lvert\gamma\rangle \Rightarrow P(\alpha) = \delta^{(2)}(\alpha-\gamma)$
$\overline{(\alpha^*)^m\alpha^n} = \langle (a^\dagger)^m a^n\rangle$
Variance $\overline{\lvert\Delta\alpha\rvert^2} = \langle \Delta a^\dagger \Delta a\rangle$

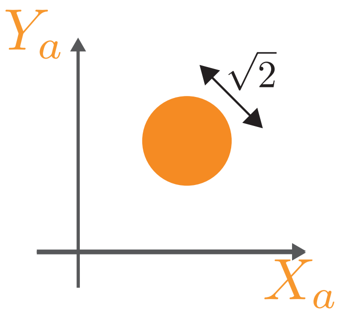

Wigner W
$W(\alpha) = 2\int_{\mathbf{C}} \frac{\mathrm{d}\beta}{\pi} e^{-2\lvert\alpha-\beta\rvert^2} P(\beta)$
Coherent state $\lvert\gamma\rangle \Rightarrow W(\alpha) = \frac{2}{\pi} e^{-2\lvert\alpha-\gamma\rvert^2}$
$\overline{(\alpha^*)^m\alpha^n} = \langle \{(a^\dagger)^m a^n\}_{\text{sym ordering}}\rangle$
Variance $\overline{\lvert\Delta\alpha\rvert^2} = \frac{\langle \Delta a^\dagger \Delta a\rangle + \langle \Delta a \Delta a^\dagger\rangle}{2}$

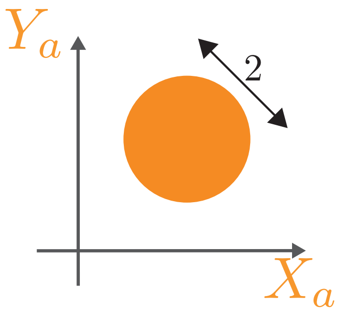

Husumi Q
$Q(\alpha) = \int_{\mathbf{C}} \frac{\mathrm{d}\beta}{\pi} e^{-\lvert\alpha-\beta\rvert^2} P(\beta)$
Coherent state $\lvert\gamma\rangle \Rightarrow Q(\alpha) = \frac{1}{\pi} e^{-\lvert\alpha-\gamma\rvert^2}$
$\overline{(\alpha^*)^m\alpha^n} = \langle a^n (a^\dagger)^m\rangle$
Variance $\overline{\lvert\Delta\alpha\rvert^2} = \langle \Delta a \Delta a^\dagger\rangle$

Figure A.3: Few properties of distribution functions P, W and Q. On the left of each table, in the quadrature phase-space, a disk represents the area where the distribution of a coherent state is larger than its maximum divided by e. Note that the surface of the disk is here $\pi\overline{\lvert\Delta\alpha\rvert^2}$. In the tables are given the distribution function for coherent state, the average value of $(\alpha^*)^m\alpha^n$ weighted by the distribution function and the variance of the distribution. Note that, by definition, $\Delta a = a - \langle a\rangle$.

A.2 Quantum limit

A.2.1 Noise added on mode quadratures

The variance of the output quadrature $\hat{X}_{a_{out}}$ is

$$\langle \Delta X^2_{a_{out}} \rangle \equiv \left\langle \left(\frac{\hat{a}_{out} + \hat{a}^\dagger_{out}}{2} \right)^2 \right\rangle - \left\langle \frac{\hat{a}_{out} + \hat{a}^\dagger_{out}}{2} \right\rangle^2 . \tag{A.1}$$

For a phase-preserving amplifier, this gives

$$\left\{ \begin{array}{l} \langle \Delta X^2_{a_{out}} \rangle = G \langle \Delta X^2_{a_{in}} \rangle + (G-1) \langle \Delta X^2_{b_{in}} \rangle \\ \langle \Delta Y^2_{a_{out}} \rangle = G \langle \Delta Y^2_{a_{in}} \rangle + (G-1) \langle \Delta Y^2_{b_{in}} \rangle \end{array} \right. \quad \text{(phase-preserving)} \tag{A.2}$$

Since $\langle \Delta X^2_{b_{in}} \rangle + \langle \Delta Y^2_{b_{in}} \rangle \geq 2\sqrt{\langle \Delta X^2_{b_{in}} \rangle \langle \Delta Y^2_{b_{in}} \rangle} \geq \frac{1}{2}$, the sole participation of an extra mode $\hat{b}_{in}$ adds noise to the quadratures so that

$$\frac{\langle \Delta X^2_{a_{out}} \rangle + \langle \Delta Y^2_{a_{out}} \rangle}{G} \geq \langle \Delta X^2_{a_{in}} \rangle + \langle \Delta Y^2_{a_{in}} \rangle + \frac{G-1}{2G} \tag{A.3}$$

$$\boxed{\frac{\langle \Delta X^2_{a_{out}} \rangle + \langle \Delta Y^2_{a_{out}} \rangle}{G} \underset{G \to \infty}{\gtrsim} \langle \Delta X^2_{a_{in}} \rangle + \langle \Delta Y^2_{a_{in}} \rangle + \frac{1}{2}} \tag{A.4}$$

The minimum is reached for the unsqueezed vacuum in $\hat{b}_{in}$ and corresponds to half a photon of extra noise at the input of the amplifier [11]. On the contrary, for a phase-sensitive amplifier, there is no limit on the added noise. Indeed,

$$\left\{ \begin{array}{l} \langle \Delta X^2_{a_{out}} \rangle = G_s \langle \Delta X^2_{a_{in}} \rangle \\ \langle \Delta Y^2_{a_{out}} \rangle = \frac{1}{G_s} \langle \Delta Y^2_{a_{in}} \rangle \end{array} \right. . \quad \text{(phase-sensitive)} \tag{A.5}$$

A.2.2 Degradation of the signal to noise ratio

As can be seen from the quantum limit above, a phase-preserving amplifier necessarily adds noise to the quadratures. However, one should not jump to the conclusion that the signal to noise ratio is always degraded by an amplifier. It depends on what the signal is! In order to illustrate this point, let us consider the case of homodyne and heterodyne detection. First, we will discuss the link between these measurement schemes and the distribution functions for the field.

The state of a mode can always be described by a density matrix ρ. It can also conveniently be represented by real-valued distribution functions in the quadrature phase space [131, 132]. The Glauber-Sudarshan P function is uniquely defined by

$$\rho = \int_{\mathbf{C}} \mathrm{d}\alpha P(\alpha) |\alpha\rangle\langle\alpha| . \tag{A.6}$$

From its convolutions with Gaussian distributions, one defines a whole class of distribution functions. Two of them, the Wigner function W and the Husumi Q function, are directly related to homodyne and heterodyne measurements. A summary of these functions is given in Fig. A.3.

Homodyne measurement

Homodyne measurement consists in measuring only one quadrature $X_{e^{i\theta}a_{in}}$ of the field a_{in}. In the microwave domain, it can be done by first mixing the field a_{out} with a powerful tone at frequency ω_a and phase θ. Then, by measuring the average value of the output voltage using a proper low-pass filter (typically averaged over $2\pi/\Delta\omega_a$), one gets an outcome proportional to $X_{e^{i\theta}a_{in}}$. The Wigner function gives a direct prediction of the probability to find a given outcome in homodyne measurement. Indeed, the probability $\mathcal{P}_\theta$ that the measurement of $X_{e^{i\theta}a_{in}}$ gives the outcome x is simply the integral of the Wigner function on all complex outcomes sharing that quadrature value.

$$\mathcal{P}_\theta(x) = \int_{-\infty}^{\infty} \mathrm{d}y W\left[(x+iy)e^{-i\theta}\right]. \tag{A.7}$$

Let us consider the case of an amplified coherent state. The variance of the Wigner function is then $|\Delta\alpha_{in}|^2 = \frac{1}{2}$. If one uses a phase-preserving amplifier with the idler b_{in} in the unsqueezed vacuum state (Fig. 1.1), the variance of the Wigner function $\mathrm{Var}_W(a_{out}) = \int_{\mathbf{C}} W_{out}(\alpha)\Delta\alpha^2 \mathrm{d}\alpha$ at the output is

$$\mathrm{Var}_W(a_{out}) = G - \frac{1}{2} \underset{G\to\infty}{\to} \mathbf{2}G\mathrm{Var}_W(a_{in}). \tag{A.8}$$

The factor 2 indicates that the output noise of a phase-preserving amplifier is twice as large as the input noise when considering homodyne measurement for large gains [21]. This limited efficiency can be seen directly on the signal to noise ratio. In the case of homodyne measurement, we define it as $\mathrm{SNR} \equiv \frac{\langle X\rangle^2}{\mathrm{Var}(X)}$. Therefore,

$$\mathrm{SNR}_{out} = \frac{\langle X_{a_{out}}\rangle^2}{\mathrm{Var}(X_{a_{out}})} = \frac{\langle X_{a_{in}}\rangle^2}{\langle\Delta X^2_{a_{in}}\rangle + (1-1/G)\langle\Delta X^2_{b_{in}}\rangle} \underset{G\to\infty}{\to} \frac{\mathrm{SNR}_{in}}{1+\frac{\langle\Delta X^2_{b_{in}}\rangle}{\langle\Delta X^2_{a_{in}}\rangle}}. \tag{A.9}$$

The least possible degradation would then be obtained for a squeezed idler mode, but perfect efficiency is reached only asymptotically on the squeezing parameter of idler. Note that a phase sensitive amplifier is perfectly suited to homodyne detection as it does not add any noise while amplifying the homodyne signal.

Heterodyne measurement

Heterodyne measurement consists in measuring simultaneously both quadratures $X_{a_{in}}$ and $Y_{a_{in}}$. It can be done by first mixing the field a_{out} with a powerful tone at frequency

$\omega_a+\omega_h$, where ω_h is larger than the propagating mode bandwidth $\Delta\omega_a$ but smaller than the bandwidth of the detector. It is then possible to record the resulting signal and numerically demodulate it at frequency ω_h in order to extract its quadratures $X_{a_{in}}$ and $Y_{a_{in}}$. The Husumi Q distribution gives a direct prediction of the probability to find a given outcome in heterodyne measurement [12, 13, 14, 15]. The probability to find x and y is then

$$\mathcal{P}(x+iy) = Q(x+iy). \tag{A.10}$$

If one uses a phase-preserving amplifier with the idler in the unsqueezed vacuum state (Fig. 1.1), the variance of the Husumi Q function $\mathrm{Var}_Q(a_{out}) = \int_{\mathbf{C}} Q_{out}(\alpha)\Delta\alpha^2 \mathrm{d}\alpha$ at the output is

$$\mathrm{Var}_Q(a_{out}) = G\mathrm{Var}_Q(a_{in}) + (G-1)\left(\mathrm{Var}_Q(b_{in})-1\right) = G\mathrm{Var}_Q(a_{in}). \tag{A.11}$$

Therefore, the noise of heterodyne measurement scales as the signal itself, by the gain of the amplifier. Therefore, **it is physically possible not to degrade the signal to noise ratio of a heterodyne measurement using a phase preserving amplifier**. This property translates quantitatively in the possibility to keep a qubit in a pure state during a weak heterodyne measurement of the field in a circuit-QED architecture, as was shown in Ref. [16] last year.

A.2.3 Quantifying the degradation of the signal to noise ratio in practice

There are several ways to quantify the noise added by an amplifier (see section A.3). From the perspective of quantum measurement, the most relevant is the efficiency η, which is related to the increase in variance of the Q distribution

$$\eta = \frac{G\mathrm{Var}_Q(\hat{a}_{in})}{\mathrm{Var}_Q(\hat{a}_{out})}. \tag{A.12}$$

In case of a quantum limited phase preserving amplifier, the efficiency is unity $\eta = 1$. An imperfect amplifier adds more noise than required by quantum mechanics and leads to a smaller efficiency.

A.3 Quantifying the degradation of the signal to noise ratio in practice

There are several ways to quantify the noise added by an amplifier.

- Efficiency

  The **efficiency** η is related to the increase in variance of the Q distribution

  $$\eta = \frac{G\mathrm{Var}_Q(\hat{a}_{in})}{\mathrm{Var}_Q(\hat{a}_{out})}. \tag{A.13}$$

In case of a quantum limited phase preserving amplifier, the efficiency is unity $\eta = 1$. An imperfect amplifier adds more noise than required by quantum mechanics and leads to a smaller efficiency.

- Added noise

The **added noise number** $\mathcal{A}$ is defined by the increase in the variance of the Wigner function referred to the input

$$\frac{\mathrm{Var}_W(\hat{a}_{out})}{G} \equiv \mathrm{Var}_W(\hat{a}_{in}) + \mathcal{A}.$$

The quantum limit for large gains is thus

$$\mathcal{A}_{\min} \xrightarrow[G\to+\infty]{} \frac{1}{2}.$$

- Noise figure

The **noise figure** F is defined as the ratio between signal to noise ratios of a homodyne measurement at the input and at the output

$$F \equiv \frac{\mathrm{SNR}_{in}}{\mathrm{SNR}_{out}} = \frac{1}{G}\frac{\mathrm{Var}_W(\hat{a}_{out})}{\mathrm{Var}_W(\hat{a}_{in})} = 1 + \frac{\mathcal{A}}{\mathrm{Var}_W(\hat{a}_{in})}$$

Thus, if the input is occupied by a coherent state $|\alpha\rangle$, we have the simple relation $F = 1 + 2\mathcal{A}$.

- Noise temperature

The **noise temperature** T_N is the increase in temperature that would explain the output noise if it was simply due to a thermal state. If the input state of $\hat{a}_{in}$ is a thermal field at temperature T, then

$$\frac{\mathrm{Var}_W(\hat{a}_{out})}{G} = \frac{1}{2}\coth\left(\frac{\hbar\omega}{2kT}\right) + \mathcal{A} \equiv \frac{1}{2}\coth\left(\frac{\hbar\omega}{2k(T+T_N)}\right).$$

This definition leads to the relation (if $T \to 0$)

$$T_N = \frac{\hbar\omega}{k}\frac{1}{\ln\left(1+\frac{1}{\mathcal{A}}\right)}$$

A.4 Reflection coefficient on the Josephson mixer

We consider the following Hamiltonian for the Josephson mixer in the stiff pump regime (p is a scalar complex number describing the amplitude of the pump at $\omega_a + \omega_b + \delta_p$)

$$\begin{aligned} H/\hbar = {} & -i\chi_{abp} a b p^* + i\chi_{abp} a^\dagger b^\dagger p \\ & +(\omega_a - \chi_{ap}|p|^2 - \chi_{aa} a^\dagger a) a^\dagger a \\ & +(\omega_b - \chi_{bp}|p|^2 - \chi_{bb} b^\dagger b) b^\dagger b \\ & -\chi_{ab} b^\dagger b a^\dagger a \end{aligned} \tag{A.14}$$

Quantum Langevin equations then read

$$\left\{ \begin{array}{rcl} -i\omega a & = & i[H/\hbar, a] - \frac{\kappa_a}{2} a + \sqrt{\kappa_a}\tilde{a}_{in} \\ -i\omega b & = & i[H/\hbar, b] - \frac{\kappa_b}{2} b + \sqrt{\kappa_b}\tilde{b}_{in} \end{array} \right. \tag{A.15}$$

thus,

$$\left\{ \begin{array}{rcl} -i\omega a & = & \chi_{abp} b^\dagger p - i(\omega_a - \chi_{ap}|p|^2 - \chi_{ab} b^\dagger b) a + 2i\chi_{aa}(a^\dagger a + \frac{1}{2}) a - \frac{\kappa_a}{2} a + \sqrt{\kappa_a}\tilde{a}_{in} \\ -i\omega b & = & \chi_{abp} a^\dagger p - i(\omega_b - \chi_{bp}|p|^2 - \chi_{ab} a^\dagger a) b + 2i\chi_{bb}(b^\dagger b + \frac{1}{2}) b - \frac{\kappa_b}{2} b + \sqrt{\kappa_b}\tilde{b}_{in} \end{array} \right. \tag{A.16}$$

Let us solve these equations in the classical case now ($a^\dagger \to a^*$).

$$\left\{ \begin{array}{rcl} -i\delta\omega_a a & = & \chi_{abp} b^* p + i\chi_{ab}|b|^2 a + 2i\chi_{aa}|a|^2 a - \frac{\kappa_a}{2} a + \sqrt{\kappa_a}\tilde{a}_{in} \\ -i\delta\omega_b b & = & \chi_{abp} a^* p + i\chi_{ab}|a|^2 b + 2i\chi_{bb}|b|^2 b - \frac{\kappa_b}{2} b + \sqrt{\kappa_b}\tilde{b}_{in} \end{array} \right. \tag{A.17}$$

where $\delta\omega_a = \omega - \omega_a + \chi_{ap}|p|^2 + \chi_{aa}$ and $\delta\omega_b = \omega - \omega_b + \chi_{bp}|p|^2 + \chi_{bb}$. Hence,

$$\left\{ \begin{array}{rcl} (\frac{\kappa_a}{2} - i\delta\omega_a - i\chi_{ab}|b|^2 - 2i\chi_{aa}|a|^2) a & = & \chi_{abp} b^* p + \sqrt{\kappa_a}\tilde{a}_{in} \\ (\frac{\kappa_b}{2} - i\delta\omega_b - i\chi_{ab}|a|^2 - 2i\chi_{bb}|b|^2) b & = & \chi_{abp} a^* p + \sqrt{\kappa_b}\tilde{b}_{in} \end{array} \right. \tag{A.18}$$

We now use the large gain assumption

$$|b_{in}|^2 \ll \kappa_b|b|^2 \approx |b_{out}|^2 \approx |a_{out}|^2 \approx \kappa_a|a|^2 \gg |a_{in}|^2. \tag{A.19}$$

The validity of this assumption will be checked in the end. Therefore,

$$\left\{ \begin{array}{rcl} a & = & \frac{\chi_{abp} b^* p + \sqrt{\kappa_a}\tilde{a}_{in}}{\frac{\kappa_a}{2} - i\delta\omega_a - i[\chi_{ab}\kappa_a/\kappa_b + 2\chi_{aa}]|a|^2} \\ b & = & \frac{\chi_{abp} a^* p + \sqrt{\kappa_b}\tilde{b}_{in}}{\frac{\kappa_b}{2} - i\delta\omega_b - i[\chi_{ab} + 2\chi_{bb}\kappa_a/\kappa_b]|a|^2} \end{array} \right. \tag{A.20}$$

Replacing the second equation in the first one, we get

$$\begin{aligned} a = {} & \frac{\chi_{abp}^2|p|^2}{(\frac{\kappa_a}{2} - i\delta\omega_a - i[\chi_{ab}\kappa_a/\kappa_b + 2\chi_{aa}]|a|^2)(\frac{\kappa_b}{2} + i\delta\omega_b + i[\chi_{ab} + 2\chi_{bb}\kappa_a/\kappa_b]|a|^2)} a \\ & + \frac{\sqrt{\kappa_a}\tilde{a}_{in}}{\frac{\kappa_a}{2} - i\delta\omega_a - i[\chi_{ab}\kappa_a/\kappa_b + 2\chi_{aa}]|a|^2} \\ & + \frac{\chi_{abp} p \sqrt{\kappa_b}\tilde{b}_{in}}{(\frac{\kappa_a}{2} - i\delta\omega_a - i[\chi_{ab}\kappa_a/\kappa_b + 2\chi_{aa}]|a|^2)(\frac{\kappa_b}{2} + i\delta\omega_b + i[\chi_{ab} + 2\chi_{bb}\kappa_a/\kappa_b]|a|^2)} \end{aligned} \tag{A.21}$$

Now introducing the cooperativity $C = 4\chi_{abp}^2|p|^2/(\kappa_a\kappa_b)$, the adimensionless frequency shifts $\delta\omega'_a = 2\delta\omega_a/\kappa_a + 2[\chi_{ab}/\kappa_b + 2\chi_{aa}/\kappa_a]|a|^2$ and $\delta\omega'_b = 2\delta\omega_b/\kappa_b + 2[\chi_{ab}/\kappa_b + 2\chi_{bb}/\kappa_b]|a|^2$.

$$a\left[1 - \frac{C}{(1-i\delta\omega'_a)(1+i\delta\omega'_b)}\right] = \frac{2\tilde{a}_{in}/\sqrt{\kappa_a}}{1-i\delta\omega'_a} + \alpha\tilde{b}_{in} \tag{A.22}$$

Thus, if the reflection coefficient on a is

$$r_a = \left.\frac{\tilde{a}_{out}}{\tilde{a}_{in}}\right|_{\tilde{b}_{in}=0} = \left.\frac{\sqrt{\kappa_a}a}{\tilde{a}_{in}}\right|_{\tilde{b}_{in}=0} - 1 = \frac{2+2i\delta\omega'_b}{(1-i\delta\omega'_a)(1+i\delta\omega'_b)-C} - 1 \tag{A.23}$$

and

$$r_a = \frac{1+C+i(\delta\omega'_a+\delta\omega'_b)-\delta\omega'_a\delta\omega'_b}{1-C-i(\delta\omega'_a-\delta\omega'_b)+\delta\omega'_a\delta\omega'_b} \tag{A.24}$$

Widely Tunable, Nondegenerate Three-Wave Mixing Microwave Device Operating near the Quantum Limit

N. Roch,[1] E. Flurin,[1] F. Nguyen,[1,*] P. Morfin,[1] P. Campagne-Ibarcq,[1] M. H. Devoret,[2,1,3] and B. Huard[1,†]
[1]*Laboratoire Pierre Aigrain, Ecole Normale Supérieure, CNRS (UMR 8551), Université P. et M. Curie, Université D. Diderot 24, rue Lhomond, 75231 Paris Cedex 05, France*
[2]*Collège de France, 11 Place Marcelin Berthelot, F-75231 Paris Cedex 05, France*
[3]*Department of Applied Physics, Yale University, P.O. Box 208284, New Haven, Connecticut 06520-8284, USA*
(Received 30 September 2011; published 6 April 2012)

We present the first experimental realization of a widely frequency tunable, nondegenerate three-wave mixing device for quantum signals at gigahertz frequency. It is based on a new superconducting building block consisting of a ring of four Josephson junctions shunted by a cross of four linear inductances. The phase configuration of the ring remains unique over a wide range of magnetic fluxes threading the loop. It is thus possible to vary the inductance of the ring with flux while retaining a strong, dissipation-free, and noiseless nonlinearity. The device has been operated in amplifier mode, and its noise performance has been evaluated by using the noise spectrum emitted by a voltage-biased tunnel junction at finite frequency as a test signal. The unprecedented accuracy with which the crossover between zero-point fluctuations and shot noise has been measured provides an upper bound for the noise and dissipation intrinsic to the device.

DOI: 10.1103/PhysRevLett.108.147701 PACS numbers: 84.40.Dc, 42.50.Lc, 84.30.Le, 85.25.−j

Three-wave mixing devices, i.e., nonlinear circuits converting power among three microwave signals, are key elements of analog information processing in the microwave domain [1]. However, they are based on dissipative components such as semiconductor diodes or superconductor-insulator-superconductor tunnel junctions biased near the superconducting gap [2]. The loss of signal limits their operation and also introduces noise above the minimum required by quantum mechanics [3,4]. A nondegenerate mixing device with noise close to that minimum level was demonstrated recently [5,6]. However, the hysteresis preventing flux tunability for this four-junction circuit limited possible applications to analog quantum signal processing. In this Letter, we show that, by adding four inductances to the four-junction loop, we can fully suppress the hysteresis and reach a 500 MHz frequency tunability while operating close to the quantum limit. Our improvement of the device tunability by an order of magnitude is obtained without jeopardizing other advantages of nondegenerate three-wave mixing.

An ideal nondegenerate three-wave mixing device in the microwave domain absorbs three signals at frequencies such that $\omega_X + \omega_Y = \omega_Z$ with complex amplitudes A_X^{in}, A_Y^{in}, and A_Z^{in}, respectively, and reemits signals at the same frequencies with amplitudes A_X^{out}, A_Y^{out}, and A_Z^{out} such that $|A_X^{\mathrm{out}}|^2 + |A_Y^{\mathrm{out}}|^2 + |A_Z^{\mathrm{out}}|^2 = |A_X^{\mathrm{in}}|^2 + |A_Y^{\mathrm{in}}|^2 + |A_Z^{\mathrm{in}}|^2$, that is, without internal dissipation. The device can operate in two power amplification modes: (i) the photon gain mode, for which $|A_Z^{\mathrm{in}}|^2 \gg |A_X^{\mathrm{in}}|^2, |A_Y^{\mathrm{in}}|^2$ is the pump power providing the extra photon numbers in the reemitted signals at frequencies ω_X and ω_Y, and (ii) the pure up-conversion mode for which $|A_Y^{\mathrm{in}}|^2 \gg A_X^{\mathrm{in}}, A_Z^{\mathrm{in}}$ is the pump power providing the energy difference between photons at ω_Z and photons at ω_X. The Josephson parametric converter (JPC) [6], consisting of a ring of four Josephson junctions, can perform both functions. However, its operation has little tunability, since the flux Φ_{ext} applied through the ring has to be adjusted in the close vicinity of the value $\Phi_0/2$, where $\Phi_0 = h/2e$ is the flux quantum. In the present work, we consider a more general three-wave mixing device in which four linear inductances are cross-linking the ring modulator like the spokes of a wheel [see Fig. 1(a)]. The Hamiltonian of the ring is

$$\begin{aligned} H = {} & -\tfrac{1}{2}E_J \sin(\varphi_{\mathrm{ext}})\varphi_X\varphi_Y\varphi_Z \\ & + \tfrac{1}{2}(E_L/2 + E_J\cos\varphi_{\mathrm{ext}})({\varphi_X}^2 + {\varphi_Y}^2) \\ & + \tfrac{1}{2}(E_L/4 + E_J\cos\varphi_{\mathrm{ext}}){\varphi_Z}^2 + O({\varphi_{X,Y,Z}}^4), \end{aligned} \quad (1)$$

where the three spatial mode amplitudes $\varphi_X = \varphi_1 - \varphi_3$, $\varphi_Y = \varphi_2 - \varphi_4$, and $\varphi_Z = \varphi_1 + \varphi_3 - \varphi_2 - \varphi_4$ are gauge-invariant, orthogonal linear combinations of the superconducting phases of the four nodes of the Josephson junction ring [Fig. 1(b)].

We will see below how these standing wave modes can be excited by the propagating mode amplitudes A_X^{in}, A_Y^{in}, and A_Z^{in} and emit the amplitudes A_X^{out}, A_Y^{out}, and A_Z^{out}. In the Hamiltonian (1), $E_L = {\phi_0}^2/L$ is the energy associated with each of the inductances L, and $E_J = \phi_0^2/L_J^0$ is the Josephson energy of each tunnel junction. We also define the reduced flux quantum $\phi_0 = \hbar/2e$ and the dimensionless flux $\varphi_{\mathrm{ext}} = \Phi_{\mathrm{ext}}/4\phi_0$ threading each of the nominally identical four loops of the device. The first term of the Hamiltonian is a pure three-wave mixing term, while the two others are quadratic terms determining the effective inductance of modes X, Y, and Z: $L_{X,Y,Z}^{-1} = {\phi_0}^{-2}\partial^2 H/\partial\varphi_{X,Y,Z}^2$. The value $\varphi_{\mathrm{ext}} = \pi/2$ maximizes the strength of

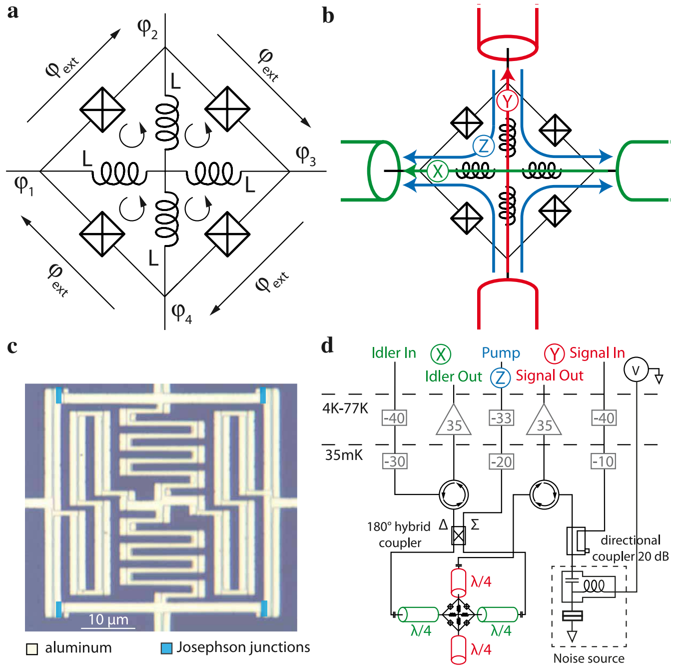

FIG. 1 (color online). (a) Device schematic: four linear inductances L cross-link a ring of four Josephson junctions. Each subloop is biased by a magnetic flux $\varphi_{\mathrm{ext}}\phi_0$. For $L < L_J^0/4$, the current through the inductances is zero, and the external flux phase biases the junctions to φ_{ext}. (b) The device is embedded at the intersection of four transmission lines and couples to spatial modes X, Y, and Z represented as arrows. (c) Optical microscope image of the ring modulator. The meanders in the center of the ring implement the four linear inductances from (a). The stripes on the meanders are due to the fabrication process based on shadow evaporation. (d) Simplified schematic of the setup used to characterize three-wave mixing operation. The idler resonator (X) is excited through a 180° hybrid coupler, while the signal resonator (Y) is single-ended. The noise emitted by the voltage-biased tunnel junction in its normal state is amplified through the signal port.

the mixing term. Provided that $E_L/2 > E_J$, modes X and Y can be tuned by varying φ_{ext} while retaining their stability: $L_{X,Y}^{-1} > 0$ on the whole range of variation. However, there is a range of fluxes for which $L_Z^{-1} < 0$ where the device departs from $\langle\varphi_Z\rangle = 0$ so that the expansion (1) is inappropriate. If the inductances are lowered even more such that $E_L/4 > E_J$, then all three modes of the device are stable for every value of φ_{ext} but at the expense of significant dilution of the nonlinear term. In contrast, as E_L is lowered below $2E_J$, dilution of nonlinearity is minimized but at the expense of the stability of the three modes. This is why the JPC, for which $E_L = 0$, can operate only within a small range of values of φ_{ext} forbidding any tunability of the device.

We have tested this new, tunable, mixing element design, by inserting the ring into a resonant structure consisting of two $\lambda/2$ transmission line resonators coupled to the X and Y modes [Fig. 1(d)] as in Ref. [7]. The Z mode is nonresonant and excited through resonator X using a hybrid coupler [Fig. 1(d)]. By varying the externally applied flux, it is possible to adjust the X and Y resonator frequencies given by

$$\omega_{X,Y} = \omega_{X,Y}^0 \frac{\pi^2 L_{X,Y}^{\lambda/2}/2}{\pi^2 L_{X,Y}^{\lambda/2}/2 + L_{X,Y}(\varphi_{\mathrm{ext}})}, \tag{2}$$

where $\omega_{X,Y}^0$ is the resonance frequency of the bare $\lambda/2$ resonator without a ring, $L_{X,Y}^{\lambda/2} = 2Z_0/(\pi\omega_{X,Y}^0)$ its lumped-element equivalent inductance [1], and Z_0 its characteristic impedance. As long as $E_L/4 + E_J\cos\varphi_{\mathrm{ext}} > 0$, the ring inductance $L_{X,Y}$ is given by

$$L_{X,Y}(\varphi_{\mathrm{ext}}) = \phi_0^2\left(\frac{E_L}{2} + E_J\cos\varphi_{\mathrm{ext}}\right)^{-1}. \tag{3}$$

The device presented in Fig. 1(c) is realized in a single e-beam lithography step. The critical current of the Al/Al$_2$O$_3$/Al Josephson junctions was designed to be in the microampere range. The wide geometric linear inductances cross-linking the ring are approximately given by $\mu_0 l$, where $l = 100$ μm is the length of each of the four meanders. According to theory, they should present negligible kinetic inductance [8]. The value of the ratio $E_L/E_J = 3 \pm 2$ should favor the stability of the X and Y modes.

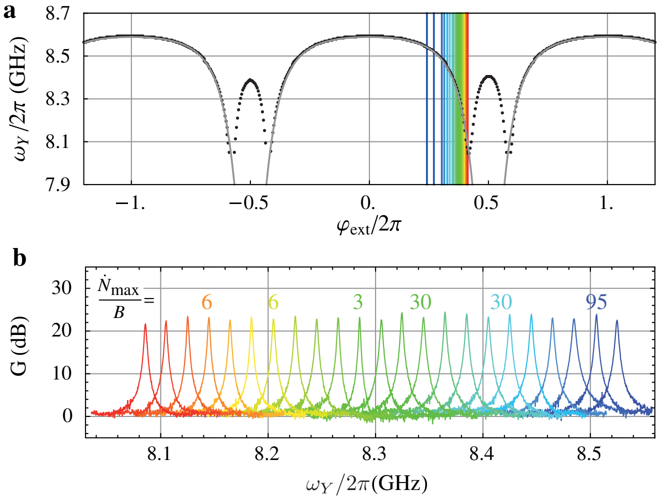

FIG. 2 (color online). (a) Dots: Measured resonance frequency ω_Y of the signal cavity as a function of flux applied to the ring modulator without the pump. Solid line: Fit of ω_Y using Eq. (2) with $\omega_Y^0/2\pi = 8.82$ GHz, $L = 49$ pH, and $E_J = \phi_0 \times 1.9$ μA and including the known stray inductance around the loop $4L_S = 200$ pH (see Ref. [9]). (b) Reflection gain measured on the signal port as a function of frequency for various values of the flux indicated by the color lines in (a). Pump parameters are optimized for each curve. The numbers on top represent the 1 dB compression point (maximum input power) expressed in input photon rate per dynamical bandwidth for six different working frequencies coded by color.

The device was operated in the photon gain mode. The phase and amplitude of the waves A_X^{out} and A_Y^{out}, relative to those of A_X^{in} and A_Y^{in}, are measured with a vector network analyzer, for a whole set of pump tones A_Z^{in}. Turning off the pump tone first, we obtained the resonance frequency of both resonators as a function of flux [see Fig. 2(a)] as well as their half-maximum bandwidths $B_X = 39$ MHz and $B_Y = 29$ MHz. Unlike in the JPC, no hysteresis was found in the dependence of the resonance frequency on applied flux, confirming the stability of our device. However, two regimes must be distinguished in the data: that of the wide arches obeying (2) with a ring inductance given by (3) and that of the narrow arches for which $E_L/4 + E_J \cos\varphi_{\mathrm{ext}} < 0$ and where the ring inductance depends precisely on the nonzero value of $\langle\varphi_Z\rangle$ emerging from the broken symmetry along the Z mode. It is interesting to note that the two possible opposite values for $\langle\varphi_Z\rangle$ in this regime give exactly the same resonance frequency. Besides, the fit of Fig. 2(a) does not take into account the perturbative effect of the parasitic inductances in series with the junctions. By using the full Hamiltonian and these stray inductances, a complete agreement with the data can be obtained over the full flux variation range [9].

The power gain G of the device is defined as the ratio of the reflected power with the pump on and off. The dependence of the gain on the pump power is shown in Fig. 3. Note, in particular, that a dynamical bandwidth $B = 3.2$ MHz is obtained for a gain of 20 dB. We checked that the parametric amplifier relation $\sqrt{G}B(G) = 2(B_X^{-1} + B_Y^{-1})^{-1}$ holds to less than 1 MHz of deviation for any pump power yielding a gain greater than 5 dB, for both signal and idler waves, as theory predicts [5].

As illustrated in Fig. 2(b), the amplifier center frequency can be flux-tuned over 400 MHz, which represents a range 2 orders of magnitude greater than the bandwidth at 20 dB. Indeed, for each center frequency, we can find a reproducible set of applied flux, pump power, and pump frequency yielding a gain higher than 20 dB and a dynamical bandwidth of $B = 3$ MHz [Fig. 2(b)]. No amplification was found in the domain of the narrow arches. While this observation cannot be explained directly by the expansion (1), it is consistent with the full Hamiltonian that predicts the nonlinear term to be significantly spoiled by spurious terms when $\langle\varphi_Z\rangle \neq 0$. The key point of our experiment is that we can still benefit, outside the range of the narrow arches, from a comfortable tunable three-wave nonlinearity. The tunability of this nondegenerate amplifier can therefore compete with the state-of-the-art degenerate Josephson amplifiers [10–15] with the added benefits of pump-signal separation.

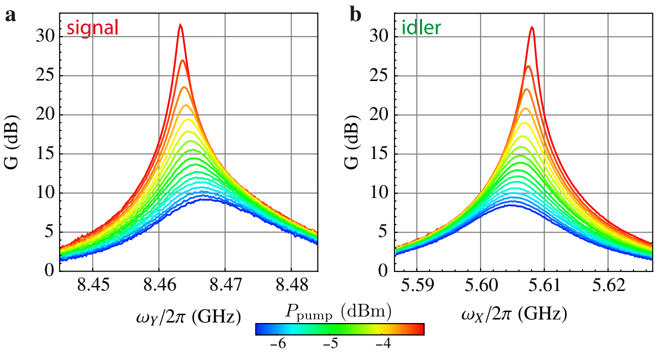

FIG. 3 (color online). Reflection gain of the phase-preserving Josephson amplifier observed on the signal Y (a) and the idler X (b) modes. The color bar indicates the pump power referred to the output of the generator. The pump frequency is $\omega_Z/2\pi = 14.071$ GHz, and the flux is set to $\varphi_{\mathrm{ext}}/2\pi \approx 0.3125$.

We now turn to dynamical range measurements which further characterize the nonlinear operation of our device. For these measurements, we first calibrated the attenuation of the line named "signal in" [Fig. 1(d)] with an accuracy of 3 dB [16]. We then measured the so-called 1 dB compression point of the amplifier mode of our device, which is the input power for which the gain is reduced by 1 dB. As presented in Fig. 2(b), this maximal power ranges between −133 and −118 dB m, corresponding to 3 and 95 photons per inverse dynamical bandwidth. The reduction in maximal allowed power occurs at lower frequencies where we have also observed that the pump power needed for a given gain is ~30 dB lower than at higher frequencies. We believe that it could be explained by the pump frequency becoming, at lower signal frequencies, resonant with a mode of the crossed resonators. The device would hence depart from the stiff pump condition needed for parametric amplification with maximal dynamic range.

In a last series of experiments, the noise of our device was assessed by using the noise emitted by a voltage-biased normal-insulator-normal (*n*-*i*-*n*) tunnel junction as input signal. This noise, which is well-understood and therefore of predictable amplitude, plays the role of an *in situ* calibrated signal. At small electronic temperatures ($k_B T_e \ll \hbar\omega_S$), the noise from a tunnel junction presents two regimes as a function of voltage. For $eV < \hbar\omega_S$, zero-point fluctuations across the junction dominate with a power spectral density $S_p(\omega_S) = \frac{\hbar\omega_S}{2}$, while for $eV > \hbar\omega_S$, electrons in the junction produce nonequilibrium shot noise and $S_p(\omega_S) = \frac{eV}{2}$. The electronic temperature T_e in the electrodes of the junction sets the sharpness of the crossover between these two regimes [17,18] as $S_p = S_p^+ + S_p^-$ with

$$S_p^{\pm}(\omega) = \frac{1}{4}(eV \pm \hbar\omega)\coth\frac{eV \pm \hbar\omega}{2k_B T_e}. \tag{4}$$

Our experiment was performed by using an aluminum junction kept in its normal state by permanent magnets close by. We measured *in situ* a normal resistance of 43.9 Ω [measurement lines not shown in Fig. 1(b)]. The output spectral density was recorded with a spectrum analyzer and averaged over a 2 MHz bandwidth around the center frequency of the amplifier [see Fig. 4(a)]. Its dependence with bias voltage was obtained [Fig. 4(b)] for

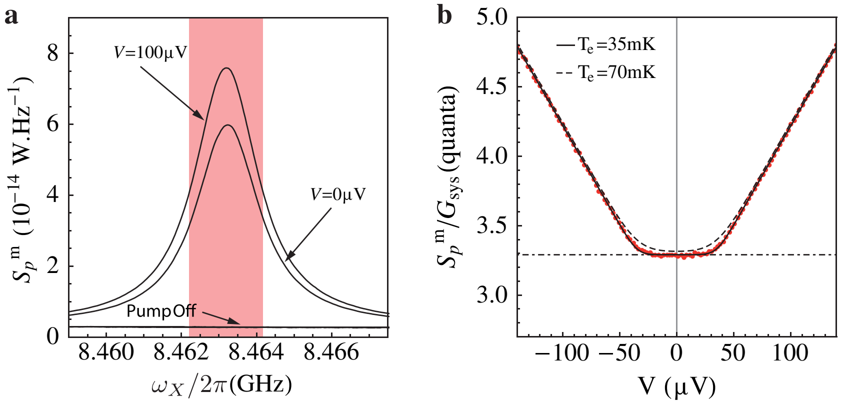

FIG. 4 (color online). (a) Power spectral density as a function of frequency measured at the output of signal out for three settings: pump *off* and $V = 0$, pump *on* and $V = 0$, or $V = 100\ \mu$V. The colored area represents the averaging range used in the right panel. (b) Average power spectral density over a 2 MHz bandwidth around the center frequency of the amplifier as a function of bias voltage V. The solid line shows what is expected by using Eq. (5) and fitting an overall gain $G_{\mathrm{sys}} = 94.6$ dB and an extra noise N_{add} of 2.8 quanta coming from both the unavoidable quantum noise of the idler port (0.5 quanta) and the unwanted losses between the tunnel junction and the amplifier (2.3 quanta). The gain G_{sys} allows us to express this power spectral density in units of photon number or quantum.

an amplifier gain of 23 dB with the same settings as in Fig. 3. The measured power spectral density is remarkably well described by an expression of the form

$$S_p^m(\omega_S) = G_{\mathrm{sys}}(S_p + N_{\mathrm{add}}\hbar\omega_S). \tag{5}$$

In the shot noise regime, it is possible to calibrate the system gain $G_{\mathrm{sys}} = dS_p^m/d(eV/2) = 94.6$ dB from the *n*-*i*-*n* tunnel element to the spectrum analyzer including a possible attenuation from the element to the input port of the amplifier. Without any additional calibration, we extracted the apparent system-added noise $N_{\mathrm{add}} = 2.8$ at the plateau [Fig. 4(b)]. This number of quanta can be thought of as the standard half quantum attributable to the unavoidable quantum noise of the load at the idler port, and 2.3 quanta left, which can be seen as an upper bound on the extra noise generated inside the device. On the other hand, an electronic temperature T_e equal to the refrigerator mixing chamber temperature of 35 mK describes perfectly the crossover. It is worth emphasizing that the noise power of the total measurement setup is presented in Fig. 4 without any background subtraction and is therefore the full *absolute* system noise. In fact, there is a finite attenuation between the junction and the amplifier leading to an underestimation of the gain counted from the input of amplifier and hence to the actual noise added by the device. Besides the unwanted insertion loss inherent to our type of low temperature measurement setup, the complex impedance of the junction itself is imperfectly matched [19]. Given the size of the junction ($\simeq 10\ \mu\mathrm{m}^2$) and previous experiments on similar junctions, we estimated its capacitance to be in the 0.7–1 pF range. Using the resistance of the junction and the characteristic impedance of the amplifier, we calculated that the loss of signal due to the *RC* filtering of the junction noise leads to an apparent added noise between 1.3 and 2.1 photons. Our measurement thus improves the N_{add} found by Bergeal *et al.* in that the measurement frequency and bandwidth are substantially higher [5]. It is straightforward to compare the noise measurement with and without our device. Turning off the pump tone, the same noise measurement using only a state-of-the-art high-electron-mobility transistor amplifier at 4 K [20] yielded an apparent added noise 20 times larger than with the pump on. This translates into an acquisition time 400 times longer, keeping the same bandwidth.

In conclusion, we have shown that it is possible to realize with Josephson tunnel junctions a widely tunable, dissipationless, nondegenerate three-wave mixing element which processes microwave signals, adding a level of noise not significantly greater than the level of unavoidable quantum noise. Such an element could be useful in a certain number of analog quantum signal processing applications, like the feedback control of the state of a quantum bit [21].

Discussions with the Quantronics group at CEA Saclay as well as with F. Mallet, F. Schackert, and T. Kontos have been greatly useful. We gratefully acknowledge P. Pari and his team as well as O. Andrieu and J. C. Dumont for technical support. The devices have been made within the consortium Salle Blanche Paris Centre. We thank D. Mailly for helping us dice wafers at LPN-Marcoussis and the Quantronics group for metal evaporations. This work was supported by the EMERGENCES program Contract of Ville de Paris and by the ANR contract ULAMSIG.

---

[*] Present address: National Institute of Standards and Technology, 325 Broadway, Boulder, CO 80305, USA.

[†] Corresponding author.
benjamin.huard@ens.fr

[1] D. Pozar, *Microwave Engineering* (Wiley, New York, 2005).

[2] M. Tinkham, *Introduction to Superconductivity* (Dover, New York, 2004).

[3] C. M. Caves, Phys. Rev. D **26**, 1817 (1982).

[4] A. Clerk *et al.*, Rev. Mod. Phys. **82**, 1155 (2010).

[5] N. Bergeal *et al.*, Nature (London) **465**, 64 (2010).

[6] N. Bergeal *et al.*, Nature Phys. **6**, 296 (2010).

[7] B. Abdo *et al.*, Appl. Phys. Lett. **99**, 162506 (2011).

[8] A. J. Annunziata *et al.*, Nanotechnology **21**, 445202 (2010).

[9] See Supplemental Material at http://link.aps.org/supplemental/10.1103/PhysRevLett.108.147701 for more details.

[10] M. A. Castellanos-Beltran *et al.*, Nature Phys. **4**, 929 (2008).

[11] M. Hatridge *et al.*, Phys. Rev. B **83**, 134501 (2011).

[12] T. Yamamoto *et al.*, Appl. Phys. Lett. **93**, 042510 (2008).

[13] R. Vijay, D. H. Slichter, and I. Siddiqi, Phys. Rev. Lett. **106**, 110502 (2011).

[14] C. Eichler *et al.*, Phys. Rev. Lett. **107**, 113601 (2011).

[15] C. M. Wilson *et al.*, Phys. Rev. Lett. **105**, 233907 (2010).

[16] To calibrate the attenuation of the signal in line, we first measure the amplification of the signal out line using the tunnel junction spectrum. We can then easily deduce the attenuation at the input by measuring the transmission from signal in to signal out lines over a wide range of powers. A 3 dB uncertainty remains due to the imperfectly known impedance of the tunnel junction.

[17] R. J. Schoelkopf *et al.*, Phys. Rev. Lett. **78**, 3370 (1997).

[18] Y. Blanter and M. Buttiker, Phys. Rep. **336**, 1 (2000).

[19] L. Spietz *et al.*, Appl. Phys. Lett. **97**, 142502 (2010).

[20] S. Weinreb, M. W. Pospieszalski, and R. Norrod, IEEE MTT-S International Microwave Symposium Digest **2**, 945 (1988).

[21] A. Korotkov, Phys. Rev. B **71**, 201305 (2005).

Selected for a Viewpoint in *Physics*
PRL **109,** 183901 (2012) PHYSICAL REVIEW LETTERS week ending 2 NOVEMBER 2012

Generating Entangled Microwave Radiation Over Two Transmission Lines

E. Flurin,[1] N. Roch,[1] F. Mallet,[1] M. H. Devoret,[2,1,3] and B. Huard[1,*]
[1]*Laboratoire Pierre Aigrain, Ecole Normale Supérieure, CNRS (UMR 8551), Université P. et M. Curie, Université D. Diderot 24, rue Lhomond, 75231 Paris Cedex 05, France*
[2]*Collège de France, 11 Place Marcelin Berthelot, F-75231 Paris Cedex 05, France*
[3]*Department of Applied Physics, Yale University, P.O. Box 208284, New Haven, Connecticut 06520-8284, USA*
(Received 3 May 2012; published 31 October 2012)

Using a superconducting circuit, the Josephson mixer, we demonstrate the first experimental realization of spatially separated two-mode squeezed states of microwave light. Driven by a pump tone, a first Josephson mixer generates, out of quantum vacuum, a pair of entangled fields at different frequencies on separate transmission lines. A second mixer, driven by a π-phase shifted copy of the first pump tone, recombines and disentangles the two fields. The resulting output noise level is measured to be lower than for the vacuum state at the input of the second mixer, an unambiguous proof of entanglement. Moreover, the output noise level provides a direct, quantitative measure of entanglement, leading here to the demonstration of 6 $\text{Mebit} \cdot \text{s}^{-1}$ (mega entangled bits per second) generated by the first mixer.

DOI: 10.1103/PhysRevLett.109.183901 PACS numbers: 42.65.Lm, 03.67.−a, 84.40.Dc, 85.25.−j

Pairs of entangled electromagnetic fields propagating on physically separated channels constitute an essential resource in quantum information processing, communication, and measurements [1,2]. They can be realized by squeezing a vacuum state shared by two spatially separated modes. This entanglement is revealed in the cross correlations between well chosen quadratures of the two fields which fall below the level of quantum vacuum noise. Given the considerable development of microwave quantum optics, these Einstein-Podolsky-Rosen (EPR) states, or spatially separated two-mode squeezed vacuum states, have become highly desirable at such frequencies. At optical frequencies, EPR states are usually prepared by parametric down-conversion of a pump tone using a $\chi^{(2)}$ nonlinear medium [3,4]. At microwave frequencies, only single-mode squeezing and two-mode squeezing between sidebands of a single transmission line have been demonstrated thus far, using degenerate Josephson parametric amplifiers [5–9]. Recently, a dissipationless, nondegenerate, three-wave mixer for microwave signals based on Josephson junctions was developed [10–12] (see Figs. 1 and 2). Strong correlations between the spontaneously emitted radiations from two ports have been observed in the parametric down-conversion mode [13], but the experiment did not directly prove the presence of entanglement in the separated output fields.

Here, we describe an interference experiment demonstrating that nondegenerate Josephson mixers can entangle and disentangle usable EPR states of microwave light (Fig. 1). A first mixer, called the "entangler," is driven by a pump tone while its two input ports are terminated by cold loads ensuring that only vacuum quantum noise enters the device. The two entangled output ports feed the input ports of a second mixer called the "analyzer." The role of the analyzer is to recombine and disentangle the two microwave fields before sending them to a standard microwave amplification and detection chain. As the phase difference between both pumps varies, the noise at the output of the analyzer exhibits interference fringes which pass under the level of amplified vacuum. Remarkably, the measurement of the noise at the output of the analyzer directly quantifies entanglement between its two input fields without resorting to two homodyne detection channels and the analysis of their correlations.

The Josephson mixer [10–12] is a superconducting circuit parametrically coupling two superconducting resonators (Fig. 2) at distinct frequencies f_a and f_b via a pump at their sum frequency $f_P = f_a + f_b$. Each resonator has only one access port, but input and output signals are spatially separated by cryogenic microwave circulators (Fig. 2 and [14]) so that the entangler output can be exclusively sent to the analyzer input. Each mixer performs a reversible transform of the wave function of the field via the unitary two-mode squeeze operator $S = \exp(re^{i\varphi_P} a^\dagger b^\dagger - re^{-i\varphi_P} ab)$, where $re^{i\varphi_P}$ is the complex squeezing parameter and a and b are the field operators of the two modes [15]. The input and output canonical field operators are related by the scattering relations

$$\begin{aligned} a_{\text{out}} &= S^\dagger a_{\text{in}} S = \cosh(r) a_{\text{in}} + e^{i\varphi_P} \sinh(r) b_{\text{in}}^\dagger, \\ b_{\text{out}}^\dagger &= S^\dagger b_{\text{in}}^\dagger S = \cosh(r) b_{\text{in}}^\dagger + e^{-i\varphi_P} \sinh(r) a_{\text{in}}, \end{aligned} \tag{1}$$

where φ_P is the phase of the pump and $G = \cosh^2 r = (P_{\text{th}} + P)^2/(P_{\text{th}} - P)^2$ is the power direct gain which increases with pump power P below the parametric self-oscillation threshold P_{th}. With the pump on, the vacuum state at the input is converted into a two-mode squeezed vacuum state $|Sq\rangle = S|0\rangle_a|0\rangle_b = \cosh(r)^{-1} \times \sum \tanh(r)^n |n\rangle_a |n\rangle_b$. Note that this entangled state can be understood as the superposition of twin photons with

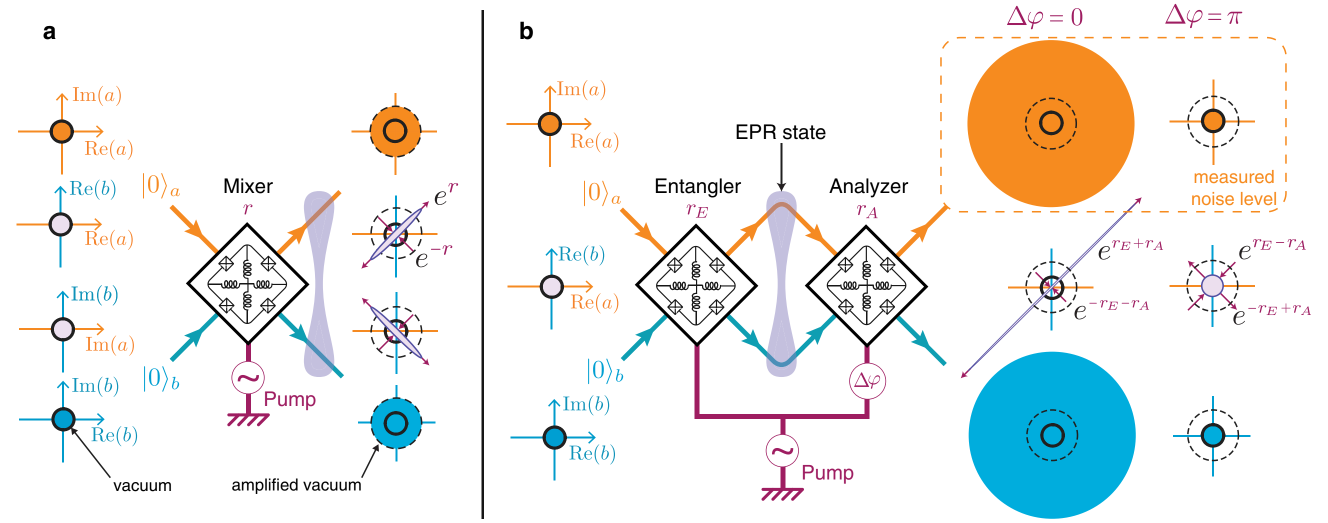

FIG. 1 (color online). Principle of the experiment. (a) When pumped with a microwave tone at frequency $f_P = f_a + f_b$, a Josephson mixer (black diamond) transforms incoming quantum vacuum noise (left) on modes a and b into an EPR state (right). The field states are represented by their standard deviation contours in the single-mode phase space of a (top), b (bottom), and in the bipartite phase space (middle) spanned by (Re(a), Re(b)) and (Im(a), Im(b)), where Re(a) $= (a + a^\dagger)/2$ and Im(a) $= (a - a^\dagger)/2i$ are the in-phase and out-of-phase quadratures of mode a. In each plot, a solid black circle sets the scale of vacuum noise and a dashed circle sets the scale of amplified vacuum noise. Quantum entanglement in the output fields is observed in the bipartite phase space where cross correlations go beyond quantum uncertainty by a squeezing factor e^{-r}. (b) In order to demonstrate entanglement at the output of this mixer named "entangler," a second, identical mixer named "analyzer" is placed in series and pumped by the same tone with phase difference $\Delta\varphi$. Entanglement at the input of the analyzer is revealed by measuring, at the analyzer output (dashed frame), a lower noise level on mode a or b than for amplified vacuum (dashed circle) for a given phase $\Delta\varphi$. The smallest (largest) output noise level occurs for opposite (equal) squeezing factor at $\Delta\varphi = \pi(0)$, and can ideally go as low as the vacuum noise level.

different frequencies and propagating on spatially separated transmission lines. Nonlocal two-mode squeezing directly appears in the combinations of output fields

$$a_{\mathrm{out}} \pm e^{i\varphi_P} b_{\mathrm{out}}^\dagger = e^{\pm r}(a_{\mathrm{in}} \pm e^{i\varphi_P} b_{\mathrm{in}}^\dagger), \tag{2}$$

which, for $\varphi_P = 0$, implies cross correlations between Re(a) and Re(b) on one hand and Im(a) and $-$Im(b) on the other hand, beating the Heisenberg limit of vacuum quantum noise, as shown in Fig. 1. In optics, these correlations have been observed by double balanced homodyne detection techniques in several systems [16]. The present experiment describes the first demonstration at microwave frequencies of these quantum correlations between signals on spatially separated transmission lines. The Josephson mixer here serves two functions. First, the entangler produces EPR states of microwave light at incommensurate frequencies and on spatially nondegenerate modes with squeezing parameter r_E. Second, the analyzer recombines input fields as shown in Eq. (1), with squeezing parameter r_A and relative pump phase $\Delta\varphi$, in order to reverse the transformation and disentangle the field state (Fig. 1).

The output noise of the entangler can be measured on each mode independently by turning off the analyzer ($r_A = 0$). The noise power spectrum measured by a spectrum analyzer is proportional to the symmetrized variance of the field operator [17]

$$(\Delta a_{\mathrm{out},E})^2 = \frac{\langle\{a_{\mathrm{out},E}, a_{\mathrm{out},E}^\dagger\}\rangle}{2} - |\langle a_{\mathrm{out},E}\rangle|^2 = \frac{\cosh 2r_E}{2}. \tag{3}$$

The variance of this "amplified vacuum" is always larger than that of the vacuum state, for which $(\Delta a)^2 = 1/2$ (Fig. 1). Discarding the information from the other mode, each output field is in a thermal state [18]. Yet, since the combined two-field state $|Sq\rangle$ is a pure state with no entropy, it is possible, ideally, to reverse the squeezing with a second mixer and reobtain a vacuum state on each port. The analyzer can perform this inversion if operated with opposite squeezing parameter $r_A = -r_E$. In practice, unavoidable losses between the two mixers prevent the exact recovery of the vacuum.

Losses are modeled as field splitters coupling uncorrelated cold thermal baths to each mode (Fig. 3) so that

$$a_{\mathrm{in},A} = \sqrt{\bar{\alpha}}\, a_{\mathrm{out},E} + \sqrt{\alpha}\, a_{\mathrm{th}} \quad \text{and} \quad b_{\mathrm{in},A} = \sqrt{\bar{\beta}}\, b_{\mathrm{out},E} + \sqrt{\beta}\, b_{\mathrm{th}},$$

where a_{th} and b_{th} describe bosonic modes of thermal baths at frequencies f_a and f_b, and $\bar{\alpha} = 1 - \alpha$, $\bar{\beta} = 1 - \beta$. Additionally, microwave photons propagate for a finite amount of time τ_a and τ_b between the two mixers leading to a correction of the phase difference entering the scattering terms $\Delta\varphi' = \Delta\varphi - 2\pi f_a \tau_a - 2\pi f_b \tau_b$. The temporal extent of the twin photons exiting the entangler is given by the inverse of the bandwidth $\Delta f = \Delta f_0 / \cosh r_E$ [13]. In

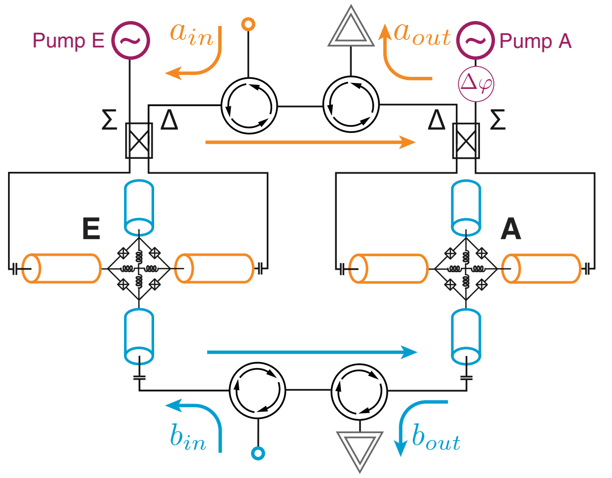

FIG. 2 (color online). Schematics of the experimental setup. Each Josephson mixer consists of a ring of Josephson junctions coupling two $\lambda/2$ superconducting resonators addressed via a 180° hybrid coupler or a single ended port. Both mixers are designed with the same geometry as in Ref. [12], and their resonance frequencies are matched at $f_a = 5.578$ GHz and $f_b = 8.812$ GHz using two independent flux biases. The pump frequencies are set to $f_P = 14.390$ GHz. Microwave circulators separate the input and output of the entangler and analyzer. Input ports are represented as open circles, and at each output port the double triangle symbolizes the low-noise amplifying measurement setup with total gain $G_{\rm LNA}$.

the experiment, the travel times τ_a and τ_b of order 2 ns are much smaller than this temporal extent since $\Delta f_0 = 28$ MHz, so that microwave photons do interfere even if their travel durations may slightly differ between modes. It is then straightforward to calculate the scattering coefficients of the full circuit. For instance, the a output mode is given by

$$a_{\text{out},A} = t_{a\to a} a_{\text{in},E} + t_{b\to a} b^{\dagger}_{\text{in},E} + \sqrt{\alpha}\cosh r_A a_{\text{th}} + e^{i\Delta\varphi}\sqrt{\beta}\sinh r_A b^{\dagger}_{\text{th}},$$

where

$$t_{a\to a} = \sqrt{\bar\alpha}\cosh r_E \cosh r_A + e^{i\Delta\varphi}\sqrt{\bar\beta}\sinh r_E \sinh r_A,$$
$$t_{b\to a} = \sqrt{\bar\alpha}\sinh r_E \cosh r_A + e^{i\Delta\varphi}\sqrt{\bar\beta}\cosh r_E \sinh r_A. \quad (4)$$

These scattering coefficients were measured using a nonlinear four-port vector network analyzer as a function of the phase difference $\Delta\varphi$ for various values of the gains $\cosh^2 r_{E,A}$ ranging from 1 to 40, a subset of which is shown in Fig. 3. The special cases where one or both of the converters is not pumped ($r = 0$) offer the opportunity to calibrate each converter gain independently. The only fit parameter for this whole set of measurements is the ratio between transmissions on both arms, found to be $\bar\beta/\bar\alpha = 0.945$.

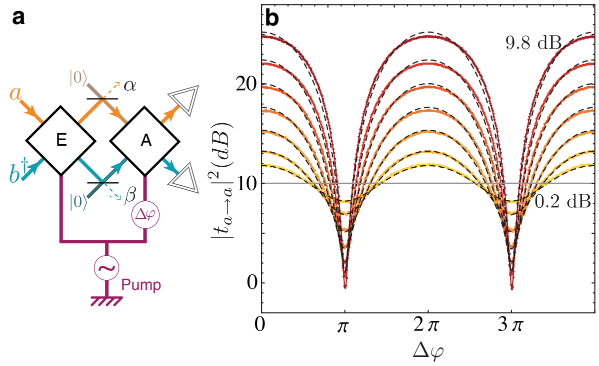

FIG. 3 (color online). (a) Protocol of the scattering coefficient measurements by a vector network analyzer connected between the a, b input and the a, b output ports. The setup is calibrated by turning on and off each Josephson mixer separately. Losses are modeled as field splitters of transparency α^2 and β^2 coupling a cold load to the signals. (b) Color traces: Transmission measurements of $|t_{a\to a}|^2$ as a function of phase difference $\Delta\varphi$ between both pump signals. The gain of the analyzer is set to $G_A = \cosh^2 r_A = 10$ (solid gray line). Each trace and color corresponds to a different gain for the entangler $G_E = \cosh^2 r_E = 0.2, 0.8, 1.8, 3.2, 5, 7.2, 9.8$ dB. Dashed lines are fits to the data using Eq. (4) and the single fit parameter $\bar\beta/\bar\alpha = 0.945$. Together with an independent, *in situ* noise calibration, this value leads to $\alpha = 0.33 \pm 0.05$ and $\beta = 0.36 \pm 0.05$ [14].

In Fig. 3, only mean values of the output field amplitudes are measured. Yet, truly quantum features appear in their correlations. Consider the case of a cold load setting the vacuum quantum state at the input of the entangler, which is reached in our experiment at 45 mK since $hf_b/k > hf_a/k = 260$ mK [14]. When the entangler is turned off ($r_E = 0$), the analyzer is fed by vacuum fluctuations and the output noise reads the amplified vacuum level $(\Delta a_{\text{out},A})^2 = \cosh(2r_A)/2$ as in Eq. (3). In general, the output noise σ^2, normalized to that reference level, on both output ports can be calculated from Eq. (4) and oscillates with phase $\Delta\varphi$ as

$$\sigma^2(\Delta\varphi) \equiv 2(\Delta a_{\text{out},A})^2/\cosh(2r_A) = \bar\alpha(\cosh 2r_E + \sinh 2r_E \tanh 2r_A \cos\Delta\varphi) + \alpha. \quad (5)$$

For simplicity, this expression is only given in the case of balanced losses $\alpha = \beta$, but the general case can be treated without much difficulty. The maximal and minimal values of σ^2, corresponding to the extrema of cross correlation between quadratures of the EPR state [ellipses in Fig. 1(a)], are obtained, respectively, for $\Delta\varphi = 0$ and $\Delta\varphi = \pi$

$$\sigma^2_{\text{max,min}} = (1-\alpha)\frac{\cosh(2r_E \pm 2r_A)}{\cosh(2r_A)} + \alpha. \quad (6)$$

The existence of a phase $\Delta\varphi$ for which the output noise σ^2 goes below 1, which demonstrate correlations beyond quantum uncertainty, is a sufficient evidence of entanglement [14,19,20].

The normalized noise power σ^2 is obtained by measuring the spectral density S_a (detailed in the Supplemental Material [14]),

$$\sigma^2(\Delta\varphi) = \frac{2}{\cosh(2r_A)}\left(\frac{S_a(\Delta\varphi) - S_{\mathrm{off}}}{hf_a G_{\mathrm{LNA}}} + \frac{1}{2}\right), \qquad (7)$$

where the noise background due to the following amplifiers S_{off} is small enough to be precisely subtracted. The spectral densities $S_a(f_a)$ and $S_b(f_b)$ of both modes at the output of the analyzer were measured using a microwave spectrum analyzer behind a cryogenic low-noise preamplifier on a 0.5 MHz bandwidth. This bandwidth was chosen to be smaller than that of the mixers for all combinations of gains $G_{E,A} = \cosh^2 r_{E,A}$ and phase differences $\Delta\varphi$. Importantly, it was possible to calibrate the total gain of the measurement setup G_{LNA}, so that the normalized noise power σ^2 is measured with at most $\pm 2.5\%$ relative error [14]. This calibration was performed by turning on a single mixer at a time and varying the temperature of a thermally decoupled input load on mode $a_{\mathrm{in},E}$. As a side result, the calibration provides the loss $\alpha = 0.33 \pm 0.05$ between mixers on mode a which, together with the ratio $\bar{\beta}/\bar{\alpha} = 0.945$ from Fig. 3, leaves no unknown parameters in the experiment.

As can be seen in Fig. 4(a), the noise does pass below the threshold of amplified vacuum noise, hence proving the existence of entanglement. Note that measurements on mode b (not shown) gave similar results, as expected. Note also that minimum noise σ^2_{min} occurs at $|r_E| < |r_A|$ and not at exactly opposite squeezing parameters. This deviation may be due to the beginning of a saturation of the analyzer mixer, corroborated by the slight deviations of the fits in Fig. 3. For each squeezing parameter r_E, it is possible to extract the extrema of noise $\sigma^2_{\mathrm{min,max}}$ from the curves of Fig. 4(a). These extremal noise measurements [Fig. 4(b)] are well described by Eq. (6) generalized to unbalanced losses between modes with $\alpha = 0.37$ and $\beta = 0.40$, consistently with the calibration. It is even possible to account for the whole dependence of the measured noise on phase difference $\Delta\varphi$ by generalizing Eq. (5) using the same parameters [Fig. 4(b)]. The overall minimum for the measured noise is reached at $\cosh^2 r_E \approx 5$ and reads $\sigma^2_{\mathrm{min}} = 0.45 \pm 0.01$ with a corresponding maximum $\sigma^2_{\mathrm{max}} = 11.9 \pm 0.1$.

It is remarkable that the amount of noise at the output of a single port of the analyzer directly measures the entanglement between the two input fields. In particular, the minimum of output noise is linked to the logarithmic negativity $E_N = -\log_2(\sigma^2_{\mathrm{min}}) = 1.15 \pm 0.04$ and to the entropy of formation $E_F = 0.69 \pm 0.03$ entangled bits (ebits, see [14]) [14,21–25]: the deeper the noise fringes, the larger the entanglement. The purity of the entangled state is also related to both extrema $\mathrm{tr}(\rho^2) = (\sigma^2_{\mathrm{min}}\sigma^2_{\mathrm{max}})^{-1} = 0.186 \pm 0.09$. These quantities of entanglement are within a factor of 2 from the state of the art in optics [21,26–28]. Given the bandwidth of the mixers, the analyzer receives a usable rate of 6 $\mathrm{Mebits \cdot s^{-1}}$ (mega entangled bits per second) from the entangler.

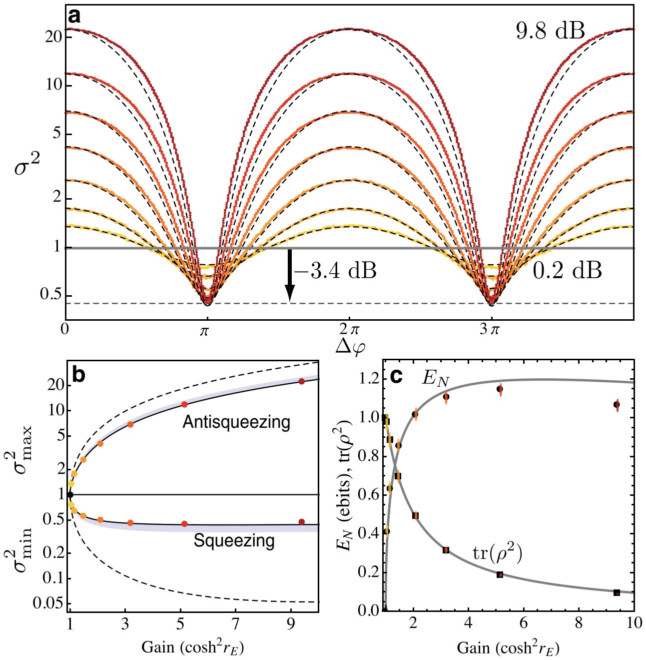

FIG. 4 (color online). (a) Color traces: Variance of the output mode $(\Delta a_{\mathrm{out}A})^2$ referred to the case of vacuum input on the analyzer [divided by $\cosh(2r_A/2)$] as a function of phase difference $\Delta\varphi$, determined by measuring the spectral density of the noise at the analyzer a output when only quantum noise enters the entangler a, b inputs. An absolute calibration allows exact conversion between both quantities with an error of at most $\pm 2.5\%$ [14]. Each color corresponds to the same gain of the entangler G_E as in Fig. 3 with a fixed gain on the analyzer $G_A = \cosh^2 r_A = 10$. The horizontal line at $\sigma^2 = 1$ represents the measured noise for amplified vacuum at the output of the analyzer ($r_E = 0$). For $\Delta\varphi$ close to π, the measured noise goes below this level, an evidence of entanglement. Dashed lines: Predicted variance using Eq. (5) extended to the unbalanced loss case using $\alpha = 0.37$ and $\beta = 0.40$. (b) Dots: Noise level measured at $\Delta\varphi = 0$ (antisqueezing) and $\Delta\varphi = \pi$ (squeezing) as a function of gain G_E for $G_A = 10$. The size of the dots is larger than the error bar. Solid lines: Prediction using Eq. (6), extended to unbalanced losses as in (a). Colored area: Consistent values of the noise using the uncertainty in the calibration of the losses α and β [14]. Dashed lines: Same prediction but without losses, $\alpha = \beta = 0$. (c) Solid dots: Logarithmic negativity measure of entanglement, with errors bars. Solid squares: Entanglement purity. Lines: Theoretical predictions using the parameters of (b).

In conclusion, we have demonstrated the production of EPR states of microwave radiation. Vacuum noise at the input of a first mixer is converted into two entangled fields. A second mixer is used to recombine and disentangle the two fields. Using an absolute calibration, the minimal noise intensity at the output of the second mixer, when the phase difference $\Delta\varphi$ is varied, constitutes a direct measure of the entanglement between the twin fields. Our measurements are limited by the finite losses between mixers but still show that a rate of 6 Mebits $\cdot$ s^{-1} travel between the entangler and the analyzer. This first implementation of spatially separated two-mode squeezed states in the microwave domain opens novel experiments on quantum teleportation or superdense coding in the fields of nanomechanical resonators and superconducting qubits. Moreover, by inserting a "circuit QED" readout cavity in one arm of the vacuum quantum noise interferometer described in this Letter, one would achieve a maximally efficient measurement, for a given photon number, of the phase shift associated with a change of qubit state.

We are grateful to N. Treps, T. Kontos, and J.-P. Poizat for fruitful discussions, P. Morfin for technical assistance, and P. Pari for giving us RuO_2 thermometers. Nanofabrication has been made within the consortium Salle Blanche Paris Centre. This work was supported by the EMERGENCES program Contract of Ville de Paris and by the ANR contract ULAMSIG.

---

[*] Corresponding author.
benjamin.huard@ens.fr

[1] S. Braunstein and P. van Loock, Rev. Mod. Phys. **77**, 513 (2005).
[2] C. Weedbrook, S. Pirandola, R. García-Patrón, N. Cerf, T. Ralph, J. Shapiro, and S. Lloyd, Rev. Mod. Phys. **84**, 621 (2012).
[3] R. E. Slusher, L. W. Hollberg, B. Yurke, J. C. Mertz, and J. F. Valley, Phys. Rev. Lett. **55**, 2409 (1985).
[4] J. Wenger, A. Ourjoumtsev, R. Tualle-Brouri, and P. Grangier, Eur. Phys. J. D **32**, 391 (2005).
[5] B. Yurke, P. Kaminsky, R. Miller, E. Whittaker, A. Smith, A. Silver, and R. Simon, Phys. Rev. Lett. **60**, 764 (1988).
[6] M. A. Castellanos-Beltran, K. D. Irwin, L. R. Vale, G. C. Hilton, and K. W. Lehnert, Nature Phys. **4**, 929 (2008).
[7] F. Mallet, M. Castellanos-Beltran, H. Ku, S. Glancy, E. Knill, K. Irwin, G. Hilton, L. Vale, and K. Lehnert, Phys. Rev. Lett. **106**, 220502 (2011).
[8] C. Eichler, D. Bozyigit, C. Lang, M. Baur, L. Steffen, J. Fink, S. Filipp, and A. Wallraff, Phys. Rev. Lett. **107**, 113601 (2011).
[9] C. M. Wilson, G. Johansson, A. Pourkabirian, M. Simoen, J. R. Johansson, T. Duty, F. Nori, and P. Delsing, Nature (London) **479**, 376 (2011).
[10] N. Bergeal, R. Vijay, V. E. Manucharyan, I. Siddiqi, R. J. Schoelkopf, S. M. Girvin, and M. H. Devoret, Nature Phys. **6**, 296 (2010).
[11] N. Bergeal, F. Schackert, M. Metcalfe, R. Vijay, V. E. Manucharyan, L. Frunzio, D. E. Prober, R. J. Schoelkopf, S. M. Girvin, and M. H. Devoret, Nature (London) **465**, 64 (2010).
[12] N. Roch, E. Flurin, F. Nguyen, P. Morfin, P. Campagne-Ibarcq, M. Devoret, and B. Huard, Phys. Rev. Lett. **108**, 147701 (2012).
[13] N. Bergeal, F. Schackert, L. Frunzio, and M. H. Devoret, Phys. Rev. Lett. **108**, 123902 (2012).
[14] See Supplemental Material at http://link.aps.org/supplemental/10.1103/PhysRevLett.109.183901 for details about the experimental setup, calibration procedure, characterization of the mixers, and calculation of the entanglement measurements.
[15] G. Grynberg, A. Aspect, and C. Fabre, *Introduction to Quantum Optics* (Cambridge University Press, Cambridge, England, 2010).
[16] M. D. Reid, P. D. Drummond, E. G. Cavalcanti, P. K. Lam, H. A. Bachor, U. L. Andersen, and G. Leuchs, Rev. Mod. Phys. **81**, 1727 (2009).
[17] A. Clerk, M. Devoret, S. Girvin, F. Marquardt, and R. Schoelkopf, Rev. Mod. Phys. **82**, 1155 (2010).
[18] P. D. Drummond and Z. Ficek, *Quantum Squeezing* (Springer-Verlag, Berlin, 2004).
[19] G. Giedke, M. M. Wolf, O. Krüger, . F. Werner, and J. I. Cirac, Phys. Rev. Lett. **91**, 107901 (2003).
[20] R. Horodecki, M. Horodecki, and K. Horodecki, Rev. Mod. Phys. **81**, 865 (2009).
[21] J. DiGuglielmo, B. Hage, A. Franzen, J. Fiurášek, and R. Schnabel, Phys. Rev. A **76**, 012323 (2007).
[22] C. H. Bennett, D. P. DiVincenzo, J. A. Smolin, and W. K. Wootters, Phys. Rev. A **54**, 3824 (1996).
[23] P. Marian and T. A. Marian, Phys. Rev. Lett. **101**, 220403 (2008).
[24] G. Vidal and R. F. Werner, Phys. Rev. A **65**, 032314 (2002).
[25] G. Adesso and F. Illuminati, Phys. Rev. A **72**, 032334 (2005).
[26] J. Laurat, T. Coudreau, G. Keller, N. Treps, and C. Fabre, Phys. Rev. A **71**, 022313 (2005).
[27] Y. Takeno, M. Yukawa, H. Yonezawa, and A. Furusawa, Opt. Express **15**, 4321 (2007).
[28] T. Eberle, V. Händchen, J. Duhme, T. Franz, R. Werner, and R. Schnabel, Phys. Rev. A **83**, 052329 (2011).

PHYSICAL REVIEW X **3**, 021008 (2013)

Persistent Control of a Superconducting Qubit by Stroboscopic Measurement Feedback

P. Campagne-Ibarcq,[1] E. Flurin,[1] N. Roch,[1] D. Darson,[1] P. Morfin,[1] M. Mirrahimi,[2]
M. H. Devoret,[3] F. Mallet,[1] and B. Huard[1]

[1]*Laboratoire Pierre Aigrain, Ecole Normale Supérieure, CNRS (UMR 8551), Université Pierre et Marie Curie, Université Denis Diderot, 24 rue Lhomond, 75231 Paris Cedex 05, France*
[2]*INRIA Paris-Rocquencourt, Domaine de Voluceau, Boîte Postale 105, 78153 Le Chesnay Cedex, France*
[3]*Department of Applied Physics, Yale University, Post Office Box 208284, New Haven, Connecticut 06520-8284, USA*

(Received 14 February 2013; published 29 May 2013)

Making a system state follow a prescribed trajectory despite fluctuations and errors commonly consists of monitoring an observable (temperature, blood-glucose level, etc.) and reacting on its controllers (heater power, insulin amount, etc.). In the quantum domain, there is a change of paradigm in feedback, since measurements modify the state of the system, most dramatically when the trajectory goes through superpositions of measurement eigenstates. Here, we demonstrate the stabilization of an arbitrary trajectory of a superconducting qubit by measurement-based feedback. The protocol benefits from the long coherence time ($T_2 > 10\ \mu$s) of the 3D transmon qubit, the high efficiency (82%) of the phase-preserving Josephson amplifier, and fast electronics that ensure less than 500 ns total delay. At discrete time intervals, the state of the qubit is measured and corrected in case an error is detected. For Rabi oscillations, where the discrete measurements occur when the qubit is supposed to be in the measurement pointer states, we demonstrate an average fidelity of 85% to the targeted trajectory. For Ramsey oscillations, which do not go through pointer states, the average fidelity reaches 76%. Incidentally, we demonstrate a fast reset protocol that allows us to cool a 3D transmon qubit down to 0.6% in the excited state.

DOI: 10.1103/PhysRevX.3.021008 Subject Areas: Condensed Matter Physics, Quantum Physics, Quantum Information

I. INTRODUCTION

The coupling of a quantum object to an environment is essential to enable its observation and manipulation. Yet, the mere existence of this coupling induces decoherence toward pointer states that are stable under monitoring of the environment [1]. There is thus a limiting time scale for the faithful preparation of a qubit in an arbitrary state or its control along a given trajectory in Hilbert space. As a part of the environment, an observer extracts information on the object and contributes to this time scale. However, if the observer acquires information faster than the uncontrolled part of the environment, it is possible to use it through a feedback process and permanently stabilize a given trajectory or state [2–5]. Superconducting qubits in cavities offer a test bed for these concepts, as well as good candidates for practical applications [6,7]. Recently, persistent Rabi oscillations have been demonstrated via analog measurement-based feedback using continuous weak measurement of a qubit [8], and qubit reset via digital measurement-based feedback using projective measurements has been performed [9]. In this work, we demonstrate a simple protocol to stabilize any trajectory of a single qubit by using a stroboscopic digital feedback based on strong measurement [10]. During the manipulation of the qubit, its state is measured in a nearly projective manner at specific time intervals and a correcting control sequence is triggered conditionally on the outcome, so as to correct its trajectory from the errors that occur due to decoherence and relaxation. The efficiency of the trajectory stabilization relies on the rapidity to measure and react, compared to decoherence. In order to minimize these time scales, we use a phase-preserving quantum-limited amplifier (see Fig. 1) [11–13] and a field-programmable gate array (FPGA), adding a delay of only 360 ns when outputting a drive pulse that is conditioned on readout (see the Supplemental Material [14] and references therein [15–19]).

II. FAST AND NONDEMOLITION PROJECTIVE MEASUREMENT

The superconducting qubit follows the design of the 3D transmon developed in Ref. [20]. A single aluminum Josephson junction, connected to two antennas of 0.4 mm by 1 mm each, on a sapphire substrate, is embedded in an empty bulk aluminum cavity, whose first coupled modes are at $\omega_c/2\pi = 7.748$ and 13 GHz when the qubit is in its ground state. External coupling rates to the first mode $\kappa_{\mathrm{in}}/2\pi = 0.34$ MHz and $\kappa_{\mathrm{out}}/2\pi = 1.49$ MHz are chosen to be of the same order of magnitude as the inverse feedback delay (500 ns), and internal losses are negligible

---

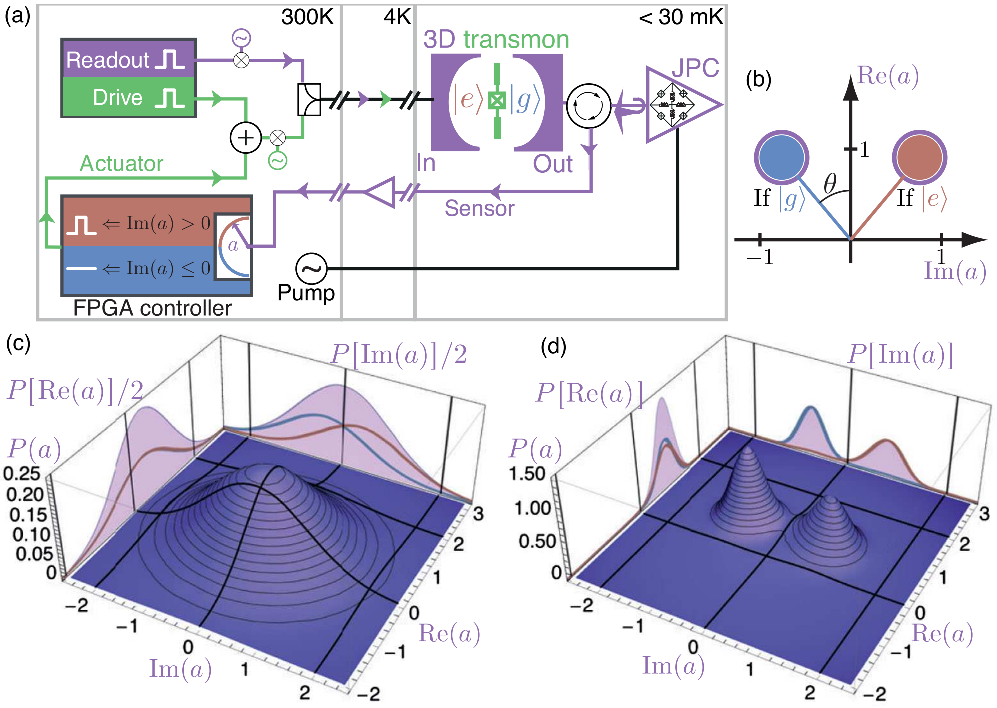

FIG. 1. (a) Schematics of the experiment. The state of a 3D transmon qubit is entangled with the phase of a coherent field transmitted through the cavity at frequency $\omega_r = \omega_c - \chi$. It is amplified by a Josephson parametric converter (JPC), and its complex amplitude a is measured and averaged by digital demodulation using an FPGA board (sensing and control). The drive at qubit transition frequency ω_{eg} is modulated by the sum of a predetermined waveform and of a conditional one generated by the FPGA board (actuation). If the transmission measurement points toward state $|e\rangle$, the actuator generates a π pulse to get the qubit back in $|g\rangle$. (b) Expected complex amplitude of the field in the cavity averaged over the measurement time T_{meas} represented as the rod of a lollypop in the Fresnel space for both qubit states. The typical deviation due to vacuum fluctuations of the field in the $N_{\mathrm{m}} = 11$ averaged modes is represented by the lollypop radius. The limited measurement efficiency ($\eta = 67\%$) only slightly increases the observed deviations by $\eta^{-1/2} - 1 = 22\%$ (purple rings). (c),(d) Probability density with the JPC (c) off and (d) on, extracted from 10^6 measurement outcomes when the qubit is prepared in state $|g\rangle$ or $|e\rangle$ with equal probability. Each outcome is the complex averaged amplitude of the field inside the transmon cavity at ω_r. The halved probability density that corresponds to the preparation of $|g\rangle$ only (respectively, $|e\rangle$) is plotted in blue (orange), together with the projections along the real and imaginary axes. Turning on the pump of the amplifier as in (d) results in a great enhancement of the measurement fidelity, compared to the case without (c).

on these scales. The cavity is anchored to a dilution fridge below 30 mK [14]. Spectroscopic measurements give a qubit frequency $\omega_{eg} = \omega_c - \Delta = 2\pi \times 3.576$ GHz that differs from the next transition by an anharmonicity $(\omega_{eg} - \omega_{fe})/2\pi = 198$ MHz. The relaxation time $T_1 = 28$ μs corresponds to the Purcell limit [21], and the pure dephasing time is $T_\phi = 14.5$ μs [Fig. 2(a)].

In the dispersive limit $\omega_{eg} - \omega_{fe} \ll \Delta$ [22], the cavity resonance frequency decreases by 2χ when the qubit goes from the ground to the excited state, and the dispersive shift here is $\chi/2\pi = 0.78$ MHz. The transmission measurement is strongest at readout frequency $\omega_r = \omega_c - \chi$, which minimizes the overlap between the two coherent states that correspond to the $|g\rangle$ and $|e\rangle$ qubit states (Fig. 1). In the experiment, square measurement pulses of 1.2 μs are sent through the cavity. The amplitude of the readout field inside the cavity can be calibrated from the measurement-induced dephasing as a function of readout power, leading to 1.4 photons, on average [14]. The outgoing signal is amplified during these 1.2 μs by using a Josephson parametric converter (JPC) [11–13] with 22 dB of gain over 6 MHz (Fig. 1 and Ref. [14]) and following amplifiers before being down-converted and digitalized by using the FPGA board input. Note that the JPC is only turned on during measurement periods, so as to minimize decoherence that occurs due to backaction [14]. The board averages numerically both quadratures of the signal during the steady part of the outgoing pulse only [see Fig. 3(a)], which corresponds to about $N_{\mathrm{m}} = T_{\mathrm{meas}}(\kappa_{\mathrm{in}} + \kappa_{\mathrm{out}}) = 11$ temporal modes of 1.4 photons. States $|g\rangle$ and $|e\rangle$ for the qubit lead to two almost nonoverlapping coherent states for the average intracavity fields $|\alpha e^{-i\theta}\rangle$ and $|\alpha e^{i\theta}\rangle$, with $\theta \approx 40°$ as expected from $\tan(\theta) = 2\chi/(\kappa_{\mathrm{in}} + \kappa_{\mathrm{out}})$ [Fig. 1(b)]. With an ideal setup measuring both quadratures of the average complex field a in the cavity, the variance on a

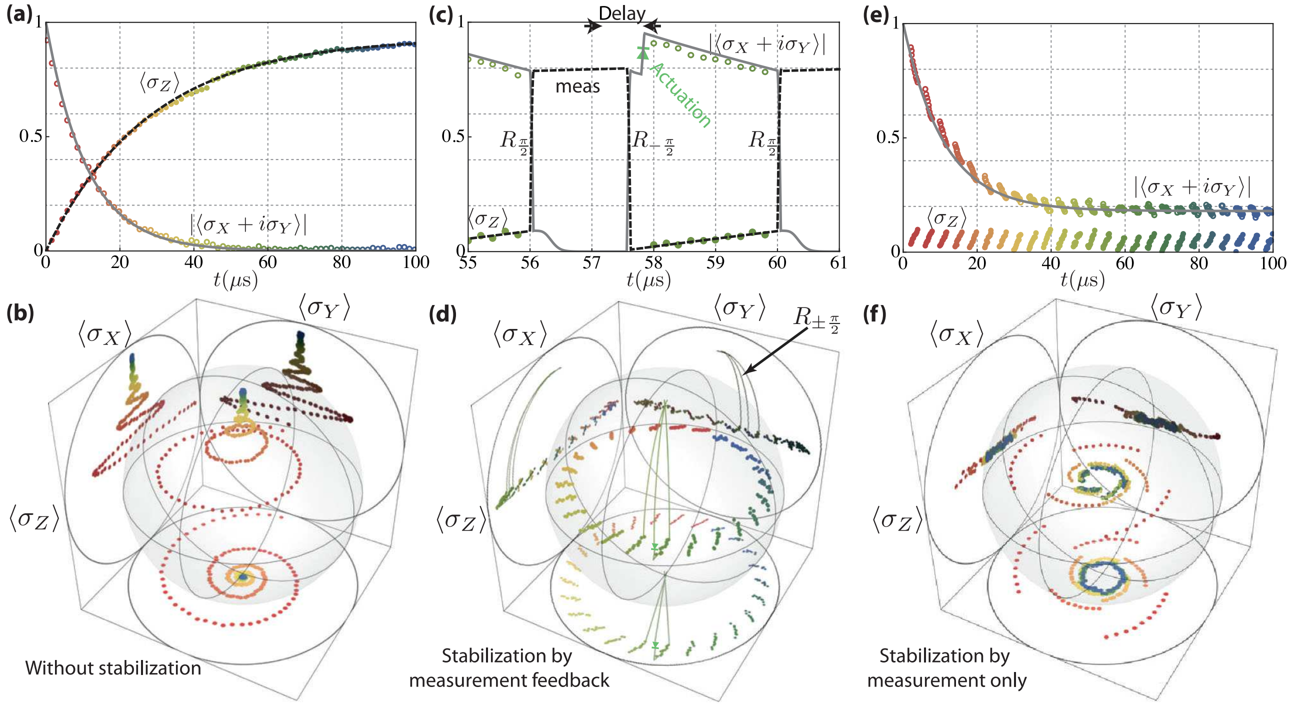

FIG. 2. (a) Evolution of $\langle\sigma_Z\rangle$ (filled dots) and of the coherence $|\langle\sigma_X + i\sigma_Y\rangle|$ (open circles) when the qubit is prepared in state $(|g\rangle + |e\rangle)/\sqrt{2}$ at time 0. The color encodes the time identically in all panels. The lines are exponential fits that use coherence time $T_2 = 11.5\ \mu$s and relaxation time $T_1 = 28\ \mu$s. (b) Same evolution represented in the Bloch sphere with a Ramsey frequency $\omega_{\mathrm{Ry}}/2\pi = 100$ kHz. At each time (color), the outcome of qubit tomography is represented as a filled dot in the Bloch sphere and in the three orthogonal projection planes. The large open black circles set the scale of the Bloch sphere extrema. (c) Same evolution as in (a), with stroboscopic measurement feedback every 4 μs. State tomography is only performed outside of the sensing and actuation periods. The lines represent the results of a simulation without extra fit parameters. When the conditional π pulse occurs (actuation), the average purity increases so that the coherences are permanently preserved, on average. (d) Same evolution represented in the Bloch sphere with a Ramsey frequency $\omega_{\mathrm{Ry}}/2\pi = 10$ kHz, instead of 100 kHz for a clearer observation of the trajectory. The simulated trajectory is represented as a line only for the time interval chosen in (c) for clarity. (e) Evolution of the qubit with the same process as in (c),(d) but without actuation. The exponential fit, using the same T_2 as in (a), indicates an average persistent coherence of 18% without any actuation. (f) In the Bloch sphere, the Ramsey frequency is chosen to be $\omega_{\mathrm{Ry}}/2\pi = 100$ kHz.

should be given by $1/\sqrt{N_{\mathrm{m}}}$ [23]. In the experiment, the 19% loss of signal through the input of the cavity ($\kappa_{\mathrm{in}}/\kappa_{\mathrm{tot}}$) and the efficiency of the detection setup (82%) degrade the signal by only 67% beyond this variance (Fig. 1). Therefore, measuring $\mathrm{Im}(a) > 0$ on the readout field indicates a qubit in the excited state $|e\rangle$ with a fidelity beyond 99.8%, taking aside the expected false counts due to relaxation events during readout. All measurement pulses in this article are performed according to this procedure, and the 0.2% infidelity is neglected throughout. Using this setup, it is possible to perform almost projective and quantum nondemolition measurements of the qubit state much faster than decoherence [24,25], a crucial ingredient of measurement-based feedback. An illustration of the discriminating power of the setup is shown as a histogram of measurement outcomes (average complex amplitude in the cavity) with the JPC amplifier on or off [Figs. 1(c) and 1(d)] for a qubit starting randomly in state $|g\rangle$ or $|e\rangle$.

III. COOLING A QUBIT USING MEASUREMENT-BASED FEEDBACK

As a benchmark of our feedback hardware, we actively cool down the qubit to its ground state, similarly to what was demonstrated by Ristè *et al.* with a phase-sensitive amplifier and digital controller [9,26]. Quantum information processing requires such removal of entropy during initialization or when correcting for errors [27]. This method allows us to do so without fast frequency tuning [28–31], postselection [24,25], or limited coupling rate $\kappa < \chi$ [32]. An initial measurement determines the qubit state. If the outcome points toward the excited state [$\mathrm{Im}(a) > 0$], the FPGA controller emits a square pulse (Fig. 1), so as to apply a π pulse around Y on the qubit only 500 ns after the first readout pulse exits the cavity (see Ref. [14] for details). As an illustration, the qubit is first prepared in the most entropic mixed state $\rho = (|g\rangle\langle g| + |e\rangle\langle e|)/2$ by either applying a π pulse or not,

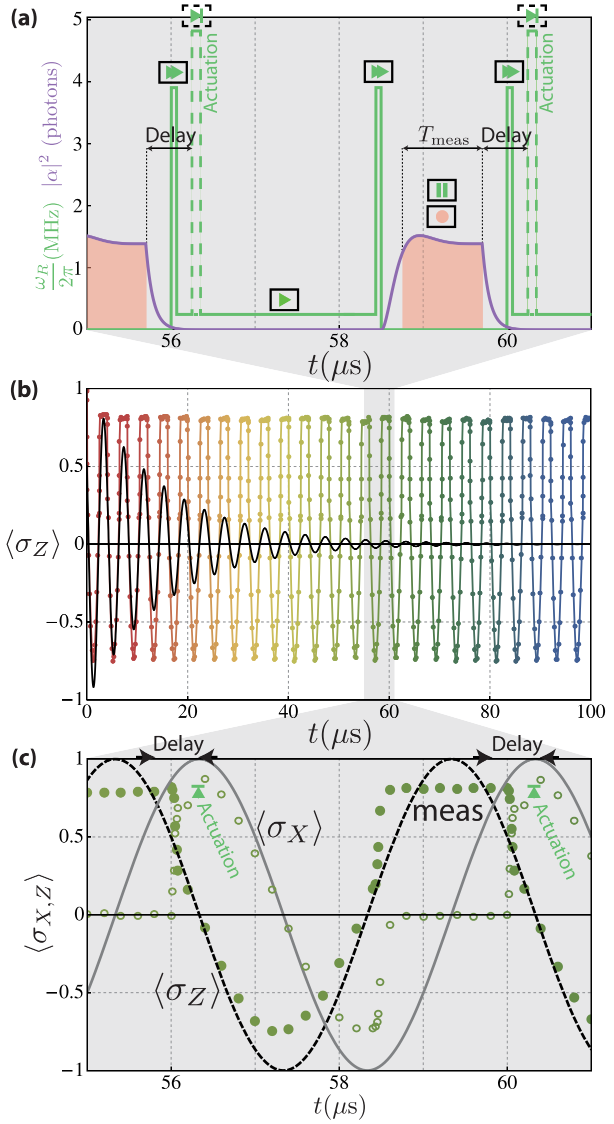

FIG. 3. (a) Pulse sequence for stabilizing Rabi oscillations. For a typical period of 4 μs, the green line represents the drive amplitude and the purple line the expected occupation of the cavity. The complex amplitude a of the measurement field is recorded only during the steady part of the occupation (red areas). When $\mathrm{Im}(a) > 0$, a fast π pulse is applied after a total delay of 500 ns (actuation). These steps are illustrated with the usual symbols for a media player. (b) The black line represents the decaying Rabi oscillation around σ_Y with frequency $\omega_R = 250$ kHz and measured decay time $T_R = 15.5$ μs. The dots on the line represent persistent Rabi oscillations measured using the pulse sequence described in (a). (c) Same measurement as in (b) shown on a smaller span for $\langle\sigma_Z\rangle$ (filled dots) and $\langle\sigma_X\rangle$ (open circles). The targeted Rabi trajectory is shown as two lines, a dashed black line for $\langle\sigma_Z\rangle$ and a solid gray one for $\langle\sigma_X\rangle$.

and averaging the outcomes over these two possibilities. The probability $P_{|e\rangle}$ for the qubit to be in state $|e\rangle$ is then measured following zero, one, or more resets by feedback. We found that starting from $P_{|e\rangle} = 50\%$, a single reset brings this level down to $P_{|e\rangle} = 3.6\%$, which would require it to thermalize during 110 μs without feedback. Yet, events where the qubit relaxes between the middle of the measurement pulse and the feedback pulse limit the efficiency of a single reset. Doing a second reset immediately after the first brings the qubit much closer to the ground state with $P_{|e\rangle} = 1.1\%$. This value does not improve with additional feedback and is limited mostly by the excitation of higher qubit states during the first reset [9]. These higher states are almost empty (0.06%) when starting from a thermalized qubit at $P_{|e\rangle} = 2.4\%$, and two consecutive resets by feedback cool the qubit further down to $P_{|e\rangle} = 0.6\%$. These results are summarized in Table I. Note that this reset allows us to prepare any state with similar purity by using rotations of the qubit once the qubit is in state $|g\rangle$ and to increase the repetition rates of quantum algorithms [26].

TABLE I. Error in the preparation of $|g\rangle$ using zero, one, or two resets by feedback when starting in the most entropic state or in the thermalized state (effectively at 46 mK).

Reset number	0	1	2
From $(|g\rangle\langle g| + |e\rangle\langle e|)/2$	50%	3.6%	1.1%
From thermalized state	2.4%	0.7%	0.6%

IV. STABILIZING A QUANTUM TRAJECTORY USING STROBOSCOPIC FEEDBACK

A. Ramsey oscillations

It is also possible to stabilize a state like $(|g\rangle + |e\rangle)/\sqrt{2}$, which is not an eigenstate of the measurement operator. First, a $\pi/2$ pulse is applied to the qubit, so as to prepare it in $(|g\rangle + |e\rangle)/\sqrt{2}$ with a drive frequency ω_{eg}. At any time t, it is possible to realize the full tomography of the qubit. Indeed, $\langle\sigma_Z\rangle$ is directly given by the average of the measurement outcomes, while $\langle\sigma_X\rangle$ (respectively, $\langle\sigma_Y\rangle$) is given by the same averaging, preceded by a rotation of the measurement axis using a 64-ns-long Rabi $\pi/2$ pulse around Y (respectively, X), where $\sigma_{X,Y,Z}$ are the Pauli matrices. In order to connect to the usual representation of Ramsey fringes at a given frequency ω_{Ry}, we can rotate the measurement axis linearly in time so that $\langle\sigma_X\rangle$ maps onto $\langle\cos(\omega_{\mathrm{Ry}}t)\sigma_X + \sin(\omega_{\mathrm{Ry}}t)\sigma_Y\rangle$ and $\langle\sigma_Y\rangle$ onto $\langle-\sin(\omega_{\mathrm{Ry}}t)\sigma_X + \cos(\omega_{\mathrm{Ry}}t)\sigma_Y\rangle$.

Without measurement-based feedback, the Bloch vector of the qubit decays exponentially both in Z and in the X, Y plane [Figs. 2(a) and 2(b)]. The decay in Z is described by time scale $T_1 = 28$ μs while the decay in X, Y is described by time scale $T_2 = 11.5$ μs. In order to stabilize persistent Ramsey oscillations, a measurement of the qubit is performed after a $\pi/2$ rotation every 4 μs. The rotation axis is chosen so that the measurement outcome should point to state $|g\rangle$ in the targeted trajectory and the qubit is rotated back to its original state by a $-\pi/2$ pulse. Each time the qubit is found to be in the $|e\rangle$ state, the FPGA controller performs a fast π pulse (actuation) with a delay of 500 ns after the measurement ends, which occurs after the $-\pi/2$ pulse. Using this stroboscopic measurement-based feedback, Ramsey oscillations are indeed preserved indefinitely [Figs. 2(c) and 2(d)]. Using optical Bloch equations [14], one can calculate the predicted qubit trajectory that corresponds to this protocol [Fig. 2(c)], which is consistent with the experiment. Deviations from the experiment likely originate from the change in measurement-induced dephasing when the JPC is turned off. The average purity $\mathrm{Tr}(\rho^2)$ of the density matrix ρ is calculated to be 85% from these simulations; the time-averaged fidelity $F = \overline{\langle\psi_{\mathrm{targ}}|\rho(t)|\psi_{\mathrm{targ}}\rangle}$ to the target trajectory $|\psi_{\mathrm{targ}}\rangle = (|g\rangle + e^{i\omega_{\mathrm{Ry}}t}|e\rangle)/\sqrt{2}$ is $F = 76\%$, and the average information quantity $1 - \mathrm{Tr}(-\rho\log\rho) = 0.60$ bit. Interestingly, the sole effect of stroboscopically measuring the qubit, without any measurement feedback, induces persistent Ramsey oscillations, except with less purity (52%), fidelity (56%), and information quantity (0.03 bit) [Figs. 2(e) and 2(f)]. This stabilization is due to the relaxation of the qubit during the measurement period toward state $|g\rangle$ that makes it more probable to reinitiate in state $(|g\rangle + |e\rangle)/\sqrt{2}$ than in state $(|g\rangle - |e\rangle)/\sqrt{2}$ after the measurement ends. It can be seen as a kind of reservoir engineering similar to Ref. [33], where the natural qubit decay is used as the dissipation source.

B. Rabi oscillations

In order to illustrate further the flexibility of stroboscopic projective measurement-based feedback, we have also stabilized Rabi oscillations. Although it is possible to perform this stabilization by using analog feedback on a weak, continuous measurement [8], we demonstrate here that discrete feedback events are more efficient [10]. Without feedback, a constant microwave signal at ω_{eg} induces a Rabi oscillation of the qubit around σ_Y with decay time $T_R = 15.5\ \mu\mathrm{s}$ [Fig. 3(b)] and frequency set to $\omega_R = 250$ kHz. In order to make the Rabi oscillations persistent, a measurement is performed each time the qubit is supposed to be in state $|g\rangle$ [Fig. 3(a)]. The FPGA controller then sends a fast correcting π pulse (actuation) at the qubit frequency ω_{eg} each time the measurement reveals that the qubit is in the excited state. In order to optimize the fidelity of the feedback-controlled trajectory to the targeted Rabi oscillation, the precession angle that is left idle during the measurement—with the Zeno effect freezing the trajectory anyway—is briefly accelerated before and after measurement to compensate exactly for that pause [see Fig. 3(a)]. As can be seen in Fig. 3(b), the Rabi oscillations are indeed stabilized permanently with this protocol. Their average fidelity to the targeted Rabi oscillation is $F = 85\%$, their average purity 80%, and their average information quantity 0.50 bit. The discrete correction events lead to visible discontinuities in the trajectories, restoring the purity lost during the last Rabi period because of decoherence.

V. CONCLUSION

The differences between continuous [8] and stroboscopic measurement feedback are enlightening. Although both methods allow the stabilization of a dynamical quantum state, continuous measurement exerts a constant dephasing rate, while stroboscopic measurement allows variations of this rate in time. For trajectories like Rabi oscillations that go through eigenstates of the measurement observable (poles of the Bloch sphere), we benefit here from the versatility of stroboscopic feedback by measuring only close to state $|g\rangle$, which is insensitive to measurement-induced dephasing, hence better preserving coherence over the whole trajectory. Besides, the stroboscopic method enables us to stabilize trajectories like Ramsey oscillations, which never reach measurement eigenstates, by periodically rotating the measurement basis.

This work illustrates the possibilities offered by measurement-based feedback for circuit quantum electrodynamics in the case of a single qubit in a cavity. We have shown here that fast digital electronics combined with efficient detection allow us to realize elaborate quantum control protocols on these systems. Future error-correction codes will benefit from the malleability of a numerical approach where complex filters need to be used to protect a quantum algorithm from errors. Extending these protocols to multiqubit architectures should enable the preparation and stabilization of more complex entangled states and trajectories.

ACKNOWLEDGMENTS

We thank Hanhee Paik for discussions, Nathanaël Cottet for help with electromagnetic field simulations, and Jack Olejnik and Richard Pescari for realizing mechanical parts. Nanofabrication has been made within the consortium Salle Blanche Paris Centre and in the Quantronics Group, which we also thank. We thank the LERMA for slicing our sapphire wafers. This work was supported by the EMERGENCES Program Contract of Ville de Paris and by the ANR Contract No. ANR-12-JCJC-TIQS.

---

[1] W. H. Zurek, *Decoherence, Einselection, and the Quantum Origins of the Classical*, Rev. Mod. Phys. **75**, 715 (2003).

[2] A. C. Doherty, S. Habib, K. Jacobs, H. Mabuchi, and S. M. Tan, *Quantum Feedback Control and Classical Control Theory*, Phys. Rev. A **62**, 012105 (2000).

[3] H. M. Wiseman and G. J. Milburn, *Quantum Measurement and Control* (Cambridge University Press, Cambridge, England, 2009).

[4] C. Sayrin, I. Dotsenko, X. Zhou, B. Peaudecerf, T. Rybarczyk, S. Gleyzes, P. Rouchon, M. Mirrahimi, H. Amini, M. Brune, J.-M. Raimond, and S. Haroche, *Real-Time Quantum Feedback Prepares and Stabilizes Photon Number States*, Nature (London) **477**, 73 (2011).

[5] X. Zhou, I. Dotsenko, B. Peaudecerf, T. Rybarczyk, C. Sayrin, S. Gleyzes, J. M. Raimond, M. Brune, and S. Haroche, *Field Locked to a Fock State by Quantum Feedback with Single Photon Corrections*, Phys. Rev. Lett. **108**, 243602 (2012).

[6] M. H. Devoret and J. M. Martinis, *Implementing Qubits with Superconducting Integrated Circuits*, Quantum Inf. Process. **3**, 163 (2004).

[7] J. Clarke and F. K. Wilhelm, *Superconducting Quantum Bits*, Nature (London) **453**, 1031 (2008).

[8] R. Vijay, C. Macklin, D. H. Slichter, S. J. Weber, K. W. Murch, R. Naik, A. N. Korotkov, and I. Siddiqi, *Stabilizing Rabi Oscillations in a Superconducting Qubit Using Quantum Feedback*, Nature (London) **490**, 77 (2012).

[9] D. Ristè, C. C. Bultink, K. W. Lehnert, and L. DiCarlo, *Feedback Control of a Solid-State Qubit Using High-Fidelity Projective Measurement*, Phys. Rev. Lett. **109**, 240502 (2012).

[10] M. Mirrahimi, B. Huard, and M. Devoret, in *Proceedings of the 51st IEEE Conference on Decision and Control, 2012* (IEEE, New York, 2012).

[11] N. Bergeal, R. Vijay, V. E. Manucharyan, I. Siddiqi, R. J. Schoelkopf, S. M. Girvin, and M. H. Devoret, *Analog Information Processing at the Quantum Limit with a Josephson Ring Modulator*, Nat. Phys. **6**, 296 (2010).

[12] N. Bergeal, F. Schackert, M. Metcalfe, R. Vijay, V. E. Manucharyan, L. Frunzio, D. E. Prober, R. J. Schoelkopf, S. M. Girvin, and M. H. Devoret, *Phase-Preserving Amplification near the Quantum Limit with a Josephson Ring Modulator*, Nature (London) **465**, 64 (2010).

[13] N. Roch, E. Flurin, F. Nguyen, P. Morfin, P. Campagne-Ibarcq, M. H. Devoret, and B. Huard, *Widely Tunable, Nondegenerate Three-Wave Mixing Microwave Device Operating near the Quantum Limit*, Phys. Rev. Lett. **108**, 147701 (2012).

[14] See Supplemental Material at http://link.aps.org/supplemental/10.1103/PhysRevX.3.021008 for technical details, calibration procedures, and simulation protocols.

[15] R. Barends *et al.*, *Minimizing Quasiparticle Generation from Stray Infrared Light in Superconducting Quantum Circuits*, Appl. Phys. Lett. **99**, 113507 (2011).

[16] A. D. Córcoles, J. M. Chow, J. M. Gambetta, C. Rigetti, J. R. Rozen, G. A. Keefe, M. B. Rothwell, M. B. Ketchen, and M. Steffen, *Protecting Superconducting Qubits from Radiation*, Appl. Phys. Lett. **99**, 181906 (2011).

[17] D. I. Schuster, A. Wallraff, A. Blais, L. Frunzio, R.-S. Huang, J. Majer, S. M. Girvin, and R. J. Schoelkopf, *ac Stark Shift and Dephasing of a Superconducting Qubit Strongly Coupled to a Cavity Field*, Phys. Rev. Lett. **94**, 123602 (2005).

[18] F. R. Ong, M. Boissonneault, F. Mallet, A. Palacios-Laloy, A. Dewes, A. C. Doherty, A. Blais, P. Bertet, D. Vion, and D. Esteve, *Circuit QED with a Nonlinear Resonator: ac-Stark Shift and Dephasing*, Phys. Rev. Lett. **106**, 167002 (2011).

[19] J. Gambetta, A. Blais, D. I. Schuster, A. Wallraff, L. Frunzio, J. Majer, M. H. Devoret, S. M. Girvin, and R. J. Schoelkopf, *Qubit-Photon Interactions in a Cavity: Measurement-Induced Dephasing and Number Splitting*, Phys. Rev. A **74**, 042318 (2006).

[20] H. Paik, D. I. Schuster, L. S. Bishop, G. Kirchmair, G. Catelani, A. P. Sears, B. R. Johnson, M. J. Reagor, L. Frunzio, L. I. Glazman, S. M. Girvin, M. H. Devoret, and R. J. Schoelkopf, *Observation of High Coherence in Josephson Junction Qubits Measured in a Three-Dimensional Circuit QED Architecture*, Phys. Rev. Lett. **107**, 240501 (2011).

[21] A. A. Houck, J. A. Schreier, B. R. Johnson, J. M. Chow, J. Koch, J. M. Gambetta, D. I. Schuster, L. Frunzio, M. H. Devoret, S. M. Girvin, and R. J. Schoelkopf, *Controlling the Spontaneous Emission of a Superconducting Transmon Qubit*, Phys. Rev. Lett. **101**, 080502 (2008).

[22] S. E. Nigg, H. Paik, B. Vlastakis, G. Kirchmair, S. Shankar, L. Frunzio, M. H. Devoret, R. J. Schoelkopf, and S. M. Girvin, *Black-Box Superconducting Circuit Quantization*, Phys. Rev. Lett. **108**, 240502 (2012).

[23] C. M. Caves, J. Combes, Z. Jiang, and S. Pandey, *Quantum Limits on Phase-Preserving Linear Amplifiers*, Phys. Rev. A **86**, 063802 (2012).

[24] J. E. Johnson, C. Macklin, D. H. Slichter, R. Vijay, E. B. Weingarten, J. Clarke, and I. Siddiqi, *Heralded State Preparation in a Superconducting Qubit*, Phys. Rev. Lett. **109**, 050506 (2012).

[25] D. Ristè, J. G. van Leeuwen, H.-S. Ku, K. W. Lehnert, and L. DiCarlo, *Initialization by Measurement of a Superconducting Quantum Bit Circuit*, Phys. Rev. Lett. **109**, 050507 (2012).

[26] D. Ristè, C. C. Bultink, M. J. Tiggelman, R. N. Schouten, K. W. Lehnert, and L. DiCarlo, *Millisecond Charge-Parity Fluctuations and Induced Decoherence in a Superconducting Qubit*, arXiv:1212.5459v1.

[27] D. P. DiVincenzo, *The Physical Implementation of Quantum Computation*, Fortschr. Phys. **48**, 771 (2000).

[28] S. O. Valenzuela, W. D. Oliver, D. M. Berns, K. K. Berggren, L. S. Levitov, and T. P. Orlando, *Microwave-Induced Cooling of a Superconducting Qubit*, Science **314**, 1589 (2006).

[29] M. Grajcar, S. H. W. van der Ploeg, A. Izmalkov, E. Il'ichev, H.-G. Meyer, A. Fedorov, A. Shnirman, and G. Schön, *Sisyphus Cooling and Amplification by a Superconducting Qubit*, Nat. Phys. **4**, 612 (2008).

[30] M. D. Reed, B. R. Johnson, A. A. Houck, L. DiCarlo, J. M. Chow, D. I. Schuster, L. Frunzio, and R. J. Schoelkopf, *Fast Reset and Suppressing Spontaneous Emission of a Superconducting Qubit*, Appl. Phys. Lett. **96**, 203110 (2010).

[31] M. Mariantoni, H. Wang, T. Yamamoto, M. Neeley, R. C. Bialczak, Y. Chen, M. Lenander, E. Lucero,

A. D. O'Connell, D. Sank, M. Weides, J. Wenner, Y. Yin, J. Zhao, A. N. Korotkov, A. N. Cleland, and J. M. Martinis, *Implementing the Quantum von Neumann Architecture with Superconducting Circuits*, Science **334**, 61 (2011).

[32] K. Geerlings, Z. Leghtas, I. M. Pop, S. Shankar, L. Frunzio, R. J. Schoelkopf, M. Mirrahimi, and M. H. Devoret, *Demonstrating a Driven Reset Protocol for a Superconducting Qubit*, Phys. Rev. Lett. **110**, 120501 (2013).

[33] K. W. Murch, U. Vool, D. Zhou, S. J. Weber, S. M. Girvin, and I. Siddiqi, *Cavity-Assisted Quantum Bath Engineering*, Phys. Rev. Lett. **109**, 183602 (2012).

Superconducting quantum node for entanglement and storage of microwave radiation

E. Flurin, N. Roch, J.D. Pillet, F. Mallet, and B. Huard*
Laboratoire Pierre Aigrain, Ecole Normale Supérieure,
CNRS (UMR 8551), Université P. et M. Curie,
Université D. Diderot 24, rue Lhomond, 75231 Paris Cedex 05, France
(Dated: January 22, 2014)

Superconducting circuits and microwave signals are good candidates to realize quantum networks, which are the backbone of quantum computers. We have realized a universal quantum node based on a 3D microwave superconducting cavity parametrically coupled to a transmission line by a Josephson ring modulator. We first demonstrate the time-controlled capture, storage and retrieval of an optimally shaped propagating microwave field, with an efficiency as high as 80 %. We then demonstrate a second essential ability, which is the timed-controlled generation of an entangled state distributed between the node and a microwave channel.

Microwave signals are a promising resource for quantum information processing. Coupled to various quantum systems [1–4] they could realize quantum networks, in which entangled information is processed by quantum nodes and distributed through photonic channels [5, 6]. The quantum nodes should generate and distribute microwave entangled fields while controlling their emission and reception in time. Superconducting circuits are able to generate entanglement [7–10] and quantum memories provide control in time as demonstrated in emerging implementations in the microwave domain using spin ensembles [11–13], superconducting circuits [14, 15] or mechanical resonators [16, 17]. Here, we present a superconducting device both able to store and generate entangled microwave radiations shared between a memory and a propagating mode. It is based on the Josephson ring modulator [18, 19] that enables to switch dynamically on or off the coupling between a low-loss cavity and a transmission line by frequency conversion. We demonstrate the time-controlled capture, storage and retrieval of a propagating coherent state in a long lived electromagnetic mode. Exploiting the versatility of this circuit, we then demonstrate the timed-controlled generation of an Einstein-Podolsky-Rosen (EPR) state distributed between the quantum memory and a propagating wavepacket. These new capabilities pave the way for complex quantum communication and quantum computing protocols by means of photonic channels in the microwave domain.

The superconducting node is made of three components: a memory, a buffer and a parametric coupler linking them. The memory is the fundamental mode $\hat{m}$ at frequency $f_m = 7.80$ GHz of a low-loss 3D superconducting cavity cooled down to 40 mK (Fig. 1). The buffer is the fundamental mode $\hat{a}$ at frequency f_a of an on-chip resonator and is the only component directly coupled to the network channels with propagating modes $\hat{a}_{in/out}$. The large coupling rate $\kappa_a = (20\text{ ns})^{-1}$ between buffer and channel ensures fast communication compared to decoherence. The memory and buffer are parametrically coupled through a ring of four Josephson junctions pumped with a classical control field p at fre-

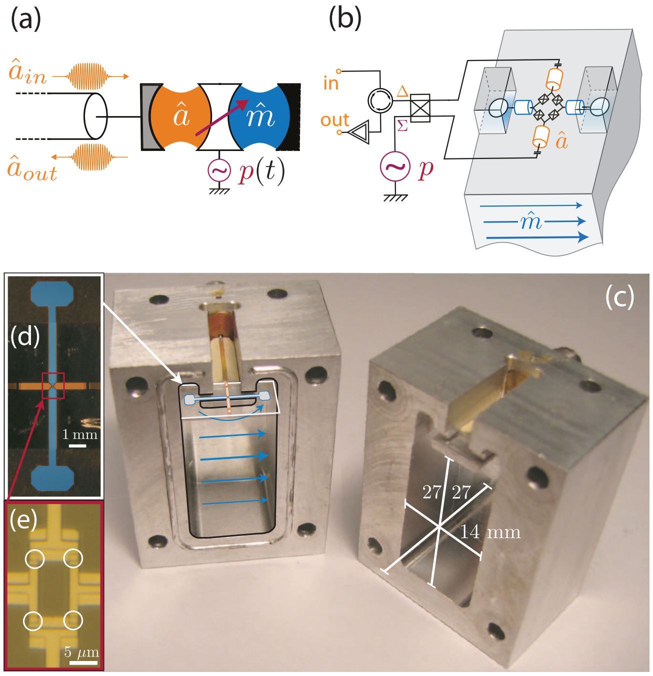

Figure 1: (a) Schematic of the experimental setup. A high-Q memory mode $\hat{m}$ is parametrically coupled to a low-Q buffer mode $\hat{a}$, hence to input/output propagating modes $\hat{a}_{in}$ and $\hat{a}_{out}$, depending on the pump amplitude p. (b),(c) Schematics and picture of the device. The on-chip circuit couples to a 3D superconducting cavity via antennas. The blue arrows represent the polarization of the fundamental mode TE 110 in the cavity. The Josephson ring and buffer resonator are on-chip. The differential mode (Δ) couples with the buffer mode while the common mode (Σ) is used for addressing the pump. (d) Picture of the aluminum circuit fabricated on a c-plane sapphire substrate. The antennas (blue) and the buffer microstrip resonator (orange) are highlighted in false color. (e) Optical microscope image of the Josephson ring at the crossing between antennas and buffer resonator. The Josephson junctions are circled in white.

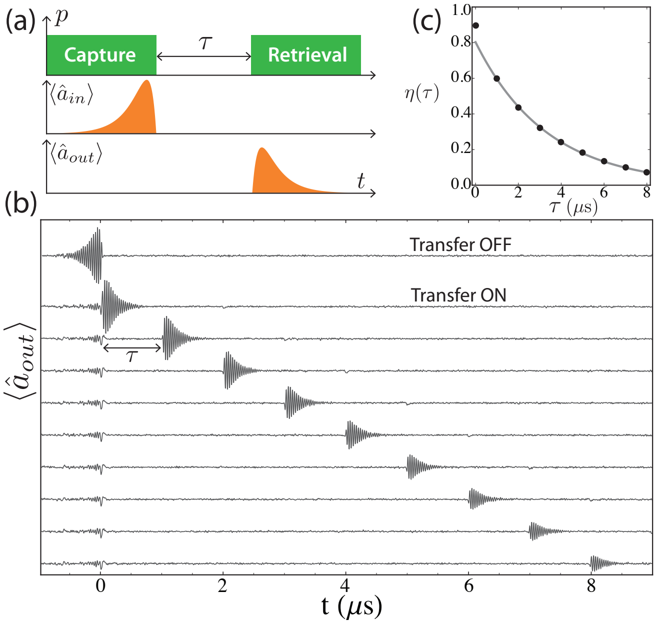

Figure 2: (a) Capture, store and release protocol. Pulse sequences for the pump field p (green) at the difference frequency $f_p = f_a - f_m$, the input field a_{in} and the resulting output field a_{out} (orange). The temporal shape of the input field is chosen in order to optimize the capture efficiency. (b) Time traces of the amplitude of the output field down converted to 40MHz and averaged 6×10^4 times. The top trace is measured without pump and reveals the optimized input signal. The following traces correspond to the sequence of (a) with increasing delay τ between capture and retrieval from 0 μs to 8 μs. (c) Dots: retrieval efficiency η as function of delay τ. η is defined as the ratio of the retrieved energy normalized to the input energy. Plain line: exponential decay $\eta_0 e^{-\tau/\tau_m}$ characterizing the memory lifetime. Best fit obtained for $\eta_0 = 80$ % and $\tau_m = 3.3$ μs.

quency f_p. The magnetic flux through the ring allows to tune f_a between 8.7 and 9.6 GHz. As described in previous works [20], the ring performs three-wave-mixing and $H_{mix} = \hbar\chi(\hat{a}+\hat{a}^\dagger)(\hat{m}+\hat{m}^\dagger)(p+p^*)$. The device can be operated in two distinct ways depending on the pump frequency. For $f_p = |f_a - f_m|$, the device operates as a converter [18, 21]. In the rotating wave approximation (RWA) and with $p > 0$ the term $H_{conv} = \hbar\chi p(\hat{a}^\dagger\hat{m}+\hat{a}\hat{m}^\dagger)$ provides a tunable coupling rate χp with frequency conversion between the buffer and memory modes. Conversely, for $f_p = f_a + f_m$, the RWA leads to the parametric down-conversion Hamiltonian $H_{pd} = \hbar\chi p(\hat{a}^\dagger\hat{m}^\dagger+\hat{a}\hat{m})$. The device then operates as an entanglement generator [9]. Starting from the vacuum state, an EPR state is distributed between the propagating mode $\hat{a}_{out}$ and memory mode $\hat{m}$. These properties offer a striking resemblance with memories based on mechanical resonators whose input/output rates and frequencies are two to three orders of magnitude smaller [16, 17].

In order to demonstrate the performances of the memory, one can first capture and retrieve a propagating classical field. Depending on its temporal shape, the pump amplitude has to be shaped appropriately in order to maximize the capture efficiency [22]. In this experiment, we used the dual approach of optimizing the temporal shape of an incoming coherent state so that it is captured by a square pump pulse turning off at time $t = 0$ (Fig. 2a). The optimal shape corresponds almost to the time-reverse of a signal retrieved from an initially occupied memory [15, 23]. It depends on the input/output rate γ_{io} as [23] $a_{in}(t) \propto \theta(-t)(e^{\gamma_{io}t/2} - e^{(\kappa_a-\gamma_{io})t/2})$. The first term ensures absorption without reflection, while the second term permits the complete transfer of the absorbed pulse from the buffer to the memory cavity. The amplitude of the pump pulse was chosen in order to maximize the input/output rate to γ_{io}^0. Indeed, for large enough pump powers such that $\chi p > \kappa_a/2$ the modes $\hat{a}$ and $\hat{m}$ hybridize and the input/output rate saturates to [23] $\gamma_{io}^0 = \kappa_a(1 - \sqrt{1-(2\kappa_c/\kappa_a)^2})/2 \approx (110\text{ ns})^{-1}$. Note that it corresponds to the fully hybridized input/output rate $\kappa_a/2$ reduced by the antenna coupling rate κ_c, which is defined by the exit rate $\kappa_c \approx (50\text{ ns})^{-1}$ of the 3D mode if the antennas are directly connected to a transmission line through Δ port (Fig. 1). It is worthwhile to note that, although the memory has a finite lifetime, the frequency conversion between modes m and a ensures that the input/output rate is exactly zero $\gamma_{io} = 0$ when the pump is turned off, leading to an infinite on/off ratio. Besides, the device being non-resonant with the conversion operating frequency $f_p = f_a - f_m \approx 1.5$ GHz, the transfer rate can be varied much faster than κ_a.

The amplitude $\langle\hat{a}_{out}\rangle$ of the mode coming back from the device is measured for several pump pulse sequences (Fig. 2b). In a first control measurement (top trace), the pump is kept turned off such that the measurement corresponds to the directly reflected incoming pulse. Note that there are about 10 photons on average in the incoming wavepacket. In the following measurements (traces below) the pump is turned on before time 0 and after time τ (Fig. 2a). Only 5 % of the incoming pulse energy is reflected while it is sent at $t < 0$ indicating the efficient absorption of this pulse shape. When the pump is turned back on after a delay τ, the device releases the captured state back in the transmission line as can be seen in Fig. 2b. Note that the chosen temporal shape of the incoming signal is indeed the time reverse of these pulses up to an amplitude rescaling, which corresponds to the efficiency of the memory. Calculating the memory efficiency η, which is the ratio between the retrieved pulse energy and the incoming pulse energy leads to an exponential decay as a function of delay time $\eta(\tau) = \eta_0 e^{-\tau/\tau_m}$ (Fig. 2c). The memory lifetime $\tau_m = 3.3$ μs is much larger than γ_{io}^{-1} but limited by unidentified losses in the 3D cavity coupled to the antennas. The much smaller decay rates achieved in similar 3D cavities [24] leave room for improvement in the future. Note that the anomalously large efficiency at zero delay $\eta(0) > \eta_0 = 80$ % can be explained by a still occupied buffer cavity at time $t = 0$. Besides the outgoing phase is identical to that of the incoming pulse, demonstrating that the memory preserves phase coherence. Finally, the number of operations that can be performed by the memory within its lifetime is limited by the time-bandwidth product $\gamma_{io}\tau_m = 30$. This combination of large memory efficiency and time-bandwidth product makes this device a state of the art quantum memory [25].

Promisingly, the device cannot only be used as a memory but also as an entanglement generator. In a second experiment, we demonstrate the generation of an EPR state distributed between the propagating mode $\hat{a}_{out}$ and the memory mode. Note that this experiment has been performed during another cooldown of the same device for which the memory lifetime was slightly degraded to $\tau_m = 2.3$ μs. Starting from the vacuum state both in the memory and in the mode $\hat{a}_{out}$, a pulse at pump frequency $f_p = f_a + f_m = 17.28$ GHz produces a two-mode squeezed vacuum state $|Sq\rangle = e^{iH_{pd}\tau/\hbar}|0\rangle_a|0\rangle_m = \cosh(r)^{-1}\sum \tanh(r)^n\,|n\rangle_a\,|n\rangle_m$ where the squeezing parameter r increases with the pump pulse amplitude [9]. The entanglement between memory and propagating modes can be demonstrated by measuring the correlations between the fluctuations of their mode quadratures, and showing that there is more correlation than allowed by classical physics [7, 8, 10]. The quadratures of both modes can be measured using the same detector on line a provided that the memorized field is released into the transmission line at a later time.

The pulse sequence used in the experiment (Fig. 3a) starts by a square pump pulse at $f_p = f_a + f_m = 17.28$ GHz during 500 ns that generates an EPR state. While one part of the pair is stored in the memory, the other part propagates in the transmission line, is amplified by a low-noise amplifying detection setup and recorded using fast digital heterodyne detection based on a Field Programmable Gate Array (FPGA) [8, 26]. After a delay $\tau = 200$ ns, a square pulse is applied on the pump field at $f_p = f_a - f_m$ with an amplitude such that the output rate is γ_{io} and lasting for 500 ns. This pulse releases the memory field which is then amplified and measured using the heterodyne detection setup. At the end of a sequence, the four mode quadratures $\hat{X}_a$, $\hat{P}_a$, $\hat{X}_m$ and $\hat{P}_m$ have been measured (defining $\hat{X}_m \equiv (\hat{m}+\hat{m}^\dagger)/2$ and $\hat{P}_m \equiv (\hat{m}-\hat{m}^\dagger)/2i$).

The correlations can be calibrated using the known variance of the single mode quadratures. Indeed, for mode a, the thermal state corresponds to amplified vacuum fluctuations with a power gain $\cosh(2r)$ resulting in a variance for both quadratures $\Delta X_a^2 = \Delta P_a^2 = \cosh(2r)/4$. Note that we assume that the field is in the vacuum at thermal equilibrium with the refrigerator temperature 45 mK $\ll hf/k_B \approx 0.4$ K. The calibration then comes down to determining the gain $\cosh(2r)$ precisely. This can be done by storing a small coherent field (about 1 photon on average) in the memory and measuring the output amplitudes with and without applying the entangling 500 ns pump tone at $f_p = 17.28$ GHz before release [9]. The entangling pulse effectively amplifies the coherent field with an amplitude gain $\cosh(r)$ which is here found to be equal to 1.51.

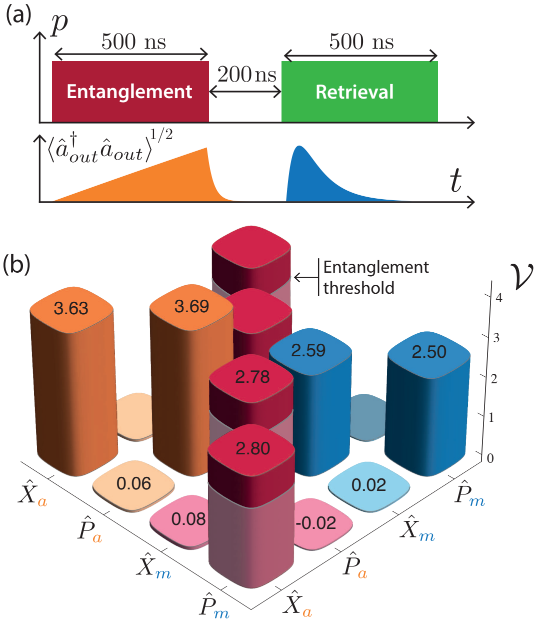

Figure 3: Entanglement between memory and propagating mode. (a) Scheme of the pulse sequence. Top: pump amplitude p is shown in red for $f_p = f_a + f_m$ and in green for $f_p = f_a - f_m$. Bottom: output noise amplitude in time. (b) Measured two-mode covariance matrix. The convention used is such that the vacuum state corresponds to the unity matrix. The 2×2 block-diagonal matrices in orange and blue represent the single mode $\hat{a}$ and $\hat{m}$ covariance matrices. The off-diagonal matrices in red represent the correlations between modes. Correlations go beyond the greyed regions which demonstrates entanglement.

One can then calculate the covariance matrix $\mathcal{V}$ of the two mode state (Fig. 3b), which fully characterizes the EPR state since it is Gaussian with zero mean [27]. The FPGA processes 4×10^7 pulse sequences in 5 minutes so that $\mathcal{V}$ is calculated with minimal post-processing [8, 23, 28]. In a coordinate system where $\mathbf{x} = \{\hat{X}_a, \hat{P}_a, \hat{X}_m, \hat{P}_m\}$, one defines $\mathcal{V}_{ij} = 2(\langle x_i x_j + x_j x_i\rangle - 2\langle x_i\rangle\langle x_j\rangle)$. Physically, it is meaningful to decompose it in four 2×2 block matrices.

$$\mathcal{V} = \begin{pmatrix} \boldsymbol{\alpha} & \boldsymbol{\chi} \\ \boldsymbol{\chi}^T & \boldsymbol{\mu} \end{pmatrix}. \tag{1}$$

The diagonal blocks $\boldsymbol{\alpha}$ and $\boldsymbol{\mu}$ are the single-mode covariance matrices for $\hat{a}$ and $\hat{m}$ respectively. Since an EPR state is thermal when disregarding the other mode, there is no correlation between quadratures X and P for a single mode and the variances ΔX^2 and ΔP^2 are almost

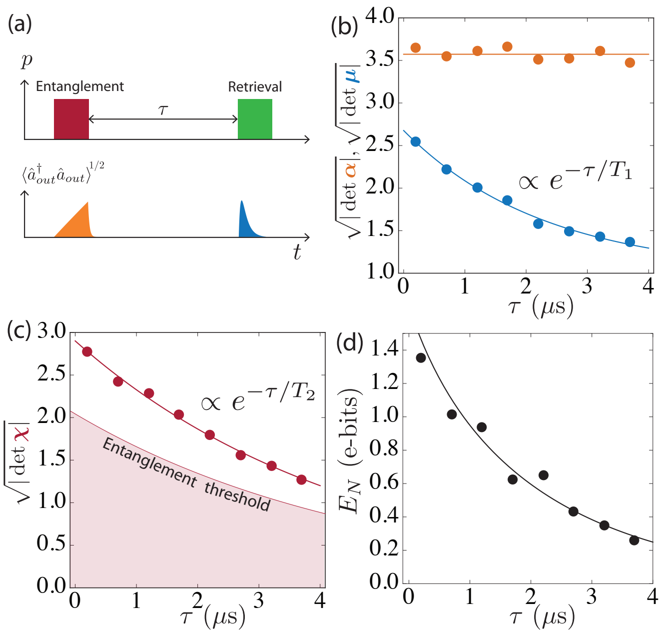

Figure 4: Covariance matrix and entanglement as a function of the storage time τ. (a) Pulse sequence with tunable storage time τ. (b) Dots: diagonal terms of the covariance matrix $\mathcal{V}$ giving the energy of each mode. Lines: average value (for α) and exponential fit (for β). The decay rate of the terms in β gives the energy relaxation time $T_1 = 2.3 \pm 0.1$ μs. (c) Dots: Off-diagonal amplitudes in $\mathcal{V}$ representing the coherence between memory and propagating modes. Line: exponential fit, whose rate sets the decoherence time $T_2 = 4.5 \pm 0.1$ μs. Correlations above the entanglement threshold ($E_N = 0$) demonstrate entanglement between memory and propagating modes. (d) Dots: Logarithmic negativity E_N measuring the entanglement between modes. Line: prediction [23].

equal. For mode a, by definition of the calibration process, one gets $\mathcal{V}_{11} \approx \mathcal{V}_{22} \approx \cosh(2r)/4 = 3.66$ (Fig. 3b). The memory mode is less occupied because of losses at a rate τ_m^{-1} during the entanglement pulse and the waiting time $\tau = 200$ ns so that $\mathcal{V}_{33} \approx \mathcal{V}_{44} \approx 2.55$. Conversely, the off-diagonal blocks $\boldsymbol{\chi}$ correspond to the correlations between modes. In each block, the phase of the pump field was optimized to put all the weight of the correlations in the two terms $\mathcal{V}_{14} \approx \mathcal{V}_{23} \approx 2.79$. The amount of entanglement in the two mode state can be measured by the logarithmic negativity E_N. It corresponds to an upper bound for distillable entanglement [28]. Here, the memory and the propagating modes share $E_N = 1.36$ entangled bits (e-bits), which indeed demonstrates the ability of the device to generate and preserve entanglement between modes.

The experiment was repeated for various storage times τ (Fig. 4a). The typical amplitude $\sqrt{|\det\boldsymbol{\mu}|}$ of the memory mode terms in $\mathcal{V}$ decrease exponentially with τ (Fig. 4b) as expected from the experiment with coherent states in Fig. 2c. This leads to a relaxation time for the memory of $T_1 = 2.3 \pm 0.1$ μs in agreement with the memory lifetime τ_m measured using coherent states in the same cool down of the device. The small variations in the amplitude of the propagating mode $\sqrt{|\det\boldsymbol{\alpha}|}$ with τ give a sense of the measurement uncertainty (Fig. 4b). Interestingly, the two-mode correlations also decay exponentially (Fig. 4c). The corresponding characteristic time is the decoherence time $T_2 = 4.5 \pm 0.1$ μs of the memory. The fact that $T_2 \approx 2T_1$ demonstrates that energy relaxation dominates all decoherence mechanisms during the storage of a quantum state. The logarithmic negativity also decreases with τ as shown in Fig. 4d.

In conclusion, we have realized quantum node based on an hybrid 2D/3D superconducting circuit. The efficient capture, storage and retrieval of a coherent state was demonstrated. Moreover, the device permits the generation and storage of entangled states distributed between the node and photonics channels. The versatility of the device paves the way for complex quantum communication protocols in the microwave domain such as continuous variable quantum teleportation. Besides, it provides a useful resource for 3D cavities where the on-demand extraction of a field quantum state was needed. This could be used to implement readout and feedback in cavity networks or even quantum computation with the memory field itself [29]. Finally, superconducting qubits can easily be embedded in this device, which could lead to protected quantum memories [4] and even protected quantum computing with microwave fields [29, 30].

We thank Michel Devoret, Vladimir Manucharyan, Mazyar Mirrahimi and Pierre Rouchon for enlightening discussions and Landry Bretheau and Philippe Campagne-Ibarcq for proofreading. Nanofabrication has been made within the consortium Salle Blanche Paris Centre. This work was supported by the Emegences program from Ville de Paris under the grant QUMOTEL and by Paris Sciences Lettres under the grant TOCOSUQI.

---

[*] corresponding author: `benjamin.huard@ens.fr`

[1] S. Haroche and J. Raimond. Exploring the Quantum: Atoms, Cavities, and Photons. *Oxford Graduated Text* 616 (2006).
[2] R. J. Schoelkopf and S. M. Girvin. Wiring up quantum systems. *Nature* **451**, 664–9 (2008).
[3] Z.-L. Xiang, S. Ashhab, J. Q. You and F. Nori. Hybrid quantum circuits: Superconducting circuits interacting with other quantum systems. *Reviews of Modern Physics* **85**, 623–653 (2013).
[4] M. H. Devoret and R. J. Schoelkopf. Superconducting circuits for quantum information: an outlook. *Science (New York, N.Y.)* **339**, 1169–74 (2013).
[5] J. Cirac, P. Zoller, H. Kimble and H. Mabuchi. Quantum State Transfer and Entanglement Distribution among Distant Nodes in a Quantum Network. *Physical Review Letters* **78**, 3221–3224 (1997).
[6] H. J. Kimble. The quantum internet. *Nature* **453**, 1023–

30 (2008).

[7] C. M. Wilson, G. Johansson, A. Pourkabirian, M. Simoen, J. Johansson, T. Duty, F. Nori and P. Delsing. Observation of the dynamical Casimir effect in a superconducting circuit. *Nature* **479**, 376–379 (2012).

[8] C. Eichler, D. Bozyigit, C. Lang, M. Baur, L. Steffen, J. M. Fink, S. Filipp and A. Wallraff. Observation of Two-Mode Squeezing in the Microwave Frequency Domain. *Physical Review Letters* **107**, 113601 (2011).

[9] E. Flurin, N. Roch, F. Mallet, M. H. Devoret and B. Huard. Generating Entangled Microwave Radiation Over Two Transmission Lines. *Physical Review Letters* **109**, 183901 (2012).

[10] E. P. Menzel, R. Di Candia, F. Deppe, P. Eder, L. Zhong, M. Ihmig, M. Haeberlein, A. Baust, E. Hoffmann, D. Ballester, K. Inomata, T. Yamamoto, Y. Nakamura, E. Solano, A. Marx and R. Gross. Path Entanglement of Continuous-Variable Quantum Microwaves. *Physical Review Letters* **109**, 250502 (2012).

[11] H. Wu, R. E. George, J. H. Wesenberg, K. Mø lmer, D. I. Schuster, R. J. Schoelkopf, K. M. Itoh, A. Ardavan, J. J. L. Morton and G. A. D. Briggs. Storage of Multiple Coherent Microwave Excitations in an Electron Spin Ensemble. *Physical Review Letters* **105**, 140503 (2010).

[12] Y. Kubo, I. Diniz, a. Dewes, V. Jacques, a. Dréau, J.-F. Roch, a. Auffeves, D. Vion, D. Esteve and P. Bertet. Storage and retrieval of a microwave field in a spin ensemble. *Physical Review A* **85**, 012333 (2012).

[13] S. Saito, X. Zhu, R. Amsüss, Y. Matsuzaki, K. Kakuyanagi, T. Shimo-Oka, N. Mizuochi, K. Nemoto, W. J. Munro and K. Semba. Towards Realizing a Quantum Memory for a Superconducting Qubit: Storage and Retrieval of Quantum States. *Physical Review Letters* **111**, 107008 (2013).

[14] Y. Yin, Y. Chen, D. Sank, P. J. J. OMalley, T. C. White, R. Barends, J. Kelly, E. Lucero, M. Mariantoni, A. Megrant, C. Neill, A. Vainsencher, J. Wenner, A. N. Korotkov, A. N. Cleland and J. M. Martinis. Catch and Release of Microwave Photon States. *Physical Review Letters* **110**, 107001 (2013).

[15] J. Wenner, Y. Yin, Y. Chen and R. Barends. Catching Shaped Microwave Photons with 99.4% Absorption Efficiency. *arXiv preprint arXiv: . . .* **1** (2013).

[16] T. a. Palomaki, J. W. Harlow, J. D. Teufel, R. W. Simmonds and K. W. Lehnert. Coherent state transfer between itinerant microwave fields and a mechanical oscillator. *Nature* **495**, 210–4 (2013).

[17] T. a. Palomaki, J. D. Teufel, R. W. Simmonds and K. W. Lehnert. Entangling Mechanical Motion with Microwave Fields. *Science (New York, N.Y.)* **710** (2013).

[18] N. Bergeal, F. Schackert, M. Metcalfe, R. Vijay, V. E. Manucharyan, L. Frunzio, D. E. Prober, R. J. Schoelkopf, S. M. Girvin and M. H. Devoret. Phase-preserving amplification near the quantum limit with a Josephson ring modulator. *Nature* **465**, 64 (2010).

[19] N. Bergeal, R. Vijay, V. E. Manucharyan, I. Siddiqi, R. J. Schoelkopf, S. M. Girvin and M. H. Devoret. Analog information processing at the quantum limit with a Josephson ring modulator. *Nature Physics* **6**, 296–302 (2010).

[20] B. Abdo, A. Kamal and M. Devoret. Nondegenerate three-wave mixing with the Josephson ring modulator. *Physical Review B* **87**, 014508 (2013).

[21] B. Abdo, K. Sliwa and F. Schackert. Full coherent frequency conversion between two microwave propagating modes. *arXiv preprint arXiv: . . .* (2012).

[22] I. Novikova, A. V. Gorshkov, D. F. Phillips, A. S. Sø rensen, M. D. Lukin and R. L. Walsworth. Optimal Control of Light Pulse Storage and Retrieval. *Physical Review Letters* **98**, 243602 (2007).

[23] No Title. *Supplementary Material* .

[24] H. Paik, D. I. Schuster, L. S. Bishop, G. Kirchmair, G. Catelani, a. P. Sears, B. R. Johnson, M. J. Reagor, L. Frunzio, L. I. Glazman, S. M. Girvin, M. H. Devoret and R. J. Schoelkopf. Observation of High Coherence in Josephson Junction Qubits Measured in a Three-Dimensional Circuit QED Architecture. *Physical Review Letters* **107**, 240501 (2011).

[25] C. Simon *et al.* Quantum memories. *The European Physical Journal D* **58**, 1–22 (2010).

[26] Eichler, Bozyigit and Wallraff. Characterizing quantum microwave radiation and its entanglement with superconducting qubits using linear detectors. *Physical Review A* (2012).

[27] Braunstein and van Loock. Quantum information with continuous variables. *Reviews of Modern Physics* **77**, 513–577 (2005).

[28] G. Adesso and F. Illuminati. Gaussian measures of entanglement versus negativities: Ordering of two-mode Gaussian states. *Physical Review A* **72**, 032334 (2005).

[29] Z. Leghtas, G. Kirchmair, B. Vlastakis, R. J. Schoelkopf, M. H. Devoret and M. Mirrahimi. Hardware-Efficient Autonomous Quantum Memory Protection. *Physical Review Letters* **111**, 120501 (2013).

[30] M. Mirrahimi, Z. Leghtas, V. V. Albert, S. Touzard, R. J. Schoelkopf, L. Jiang and M. H. Devoret. Dynamically protected cat-qubits: a new paradigm for universal quantum computation 1312.2017 (2013).

Observing interferences between past and future quantum states in resonance fluorescence

P. Campagne-Ibarcq,[1, *] L. Bretheau,[1, *] E. Flurin,[1] A. Auffèves,[2] F. Mallet,[1] and B. Huard[1]

[1] *Laboratoire Pierre Aigrain, Ecole Normale Supérieure,*
CNRS (UMR 8551), Université P. et M. Curie,
Université D. Diderot 24, rue Lhomond, 75231 Paris Cedex 05, France
[2] *CNRS and Université Grenoble Alpes, Institut Néel, 38042 Grenoble, France*

(Dated: March 3, 2014)

The fluorescence of a resonantly driven superconducting qubit is measured in the time domain, providing a weak probe of the qubit dynamics. Prior preparation and final, single-shot measurement of the qubit allows to average fluorescence records conditionally on past and future knowledge. The resulting interferences reveal purely quantum features characteristic of weak values. We demonstrate conditional average that exceed the classical range and probing of a non-hermitian operator. The experimental results are remarkably captured by a recent theory, which generalizes quantum mechanics to open quantum systems whose past and future are known.

In quantum physics, measurement results are random but their statistics can be predicted assuming some knowledge about the system in the past. Additional knowledge from a future measurement [1] deeply changes the statistics in the present and leads to purely quantum features [2, 3]. In particular conditioned average outcomes of a weak measurement, revealing the so-called weak values, were shown to go beyond the conventional range and give a way to directly measure complex quantities [4]. Recently, these concepts have been considered in the general case of open quantum systems where decoherence occurs [5–7]. Then, what are the properties of weak values for the unavoidable measurement associated to decoherence, the one performed by the environment? Here, we answer this question in the simplest open quantum system: a quantum bit in presence of a relaxation channel. We continuously monitor the fluorescence emitted by a superconducting qubit driven at resonance. Conditioned on initial preparation and final single shot measurement outcome of the qubit state, we probe weak values displaying all the above properties. The fluorescence signal exhibits interferences between oscillations associated to past and future quantum states [5–7]. The measured data are in complete agreement with theory.

A two-level system irradiated at resonance undergoes Rabi oscillations between ground state $|g\rangle$ and excited state $|e\rangle$. Conversely, these oscillations leave a footprint in the emitted fluorescence field. In the spectral domain, two side peaks appear around resonance frequency, constituting the Mollow triplet [8]. They were first observed in quantum optics and more recently in the microwave range [9]. If the detection setup allows monitoring fluorescence in the time domain, one gets a weak probe of the qubit. To access weak values of the associated qubit operator, one additionally needs to post-select the experiments depending on qubit state, which therefore needs to be measured in a single-shot manner. Superconducting qubits in cavity are fit for this task [10–12]. The principle of our experiment is described in Fig. 1. A transmon qubit with frequency $\nu_q = 5.19$ GHz is enclosed in a non-resonant superconducting 3D cavity [13], connected to two transmission lines. Line a is coupled as weakly as the internal cavity losses with a rate $\Gamma_a = 2$ kHz. It is used as a channel for resonant driving of the qubit. Since the fundamental cavity mode is far detuned from the qubit frequency by $\nu_c - \nu_q = 2.57$ GHz, almost all the resonant incoming signal is reflected. The cavity is coupled more strongly to line b, with a rate $\Gamma_b = 0.25$ MHz. With such an asymmetric coupling, most of the resonance fluorescence is emitted in the outgoing mode b_{out} and the fluorescence signal is not blinded by the large incoming drive.

Fluorescence is due to transitions from excited $|e\rangle$ to ground state $|g\rangle$. The amplitude of the emitted field is then proportional to the average of the lowering operator $\sigma_- = |g\rangle\langle e|$ of the qubit. Using the input/output formalism and eliminating the non resonant intracavity field operator, one can show [14] that the average field outgoing on line b is given by

$$\langle b_{out}\rangle = \langle b_{out}\rangle_0 - \sqrt{\gamma_{1b}}\langle\sigma_-\rangle. \tag{1}$$

The first term does not depend on qubit state and oscillates at the resonant drive frequency ν_q. In the experiment, it is mostly due to an external parasitic cross-talk (-50 dB) dominating the expected finite transmission of the cavity at frequency ν_q. The second term corresponds to the field radiated by the qubit, whose amplitude oscillates at the Rabi frequency ν_R (see Fig. 1). The prefactor γ_{1b} is the spontaneous emission rate into line b set by Purcell effect and is estimated to be of the order of $(0.1\text{ ms})^{-1}$ [15].

The fluorescence signal was measured using a heterodyne detection setup (see [15]). It records in time two voltage traces $V_{\mathrm{Re}}(t)$ and $V_{\mathrm{Im}}(t)$ that are respectively proportional to the quadratures of the outgoing field on line b at frequency ν_q. In Fig. 2a, the average traces are plotted

---

[*] These two authors contributed equally to this work

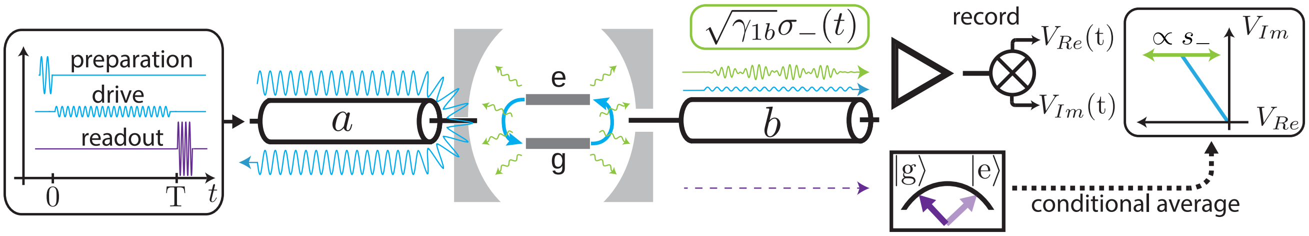

Figure 1: **Principle of the experiment.** A resonant field (blue on line a) drives a qubit via a weakly coupled line a. While the off-resonant cavity reflects most of the driving field back on line a, the fluorescence signal (green) mostly exits through the strongly coupled line b with an amplitude proportional to σ_-, and oscillating at the Rabi frequency ν_R. Due to nonzero transmission from line a, it is displaced by a resonant field independent of the qubit state (blue on line b). This signal is then measured at time t with a heterodyne detection setup including a phase-preserving quantum limited amplifier (triangle). At final time T, the qubit state is measured with high fidelity using a pulse at the bare cavity frequency (purple), enabling conditional averaging of the fluorescence signal depending on the measured state. In the quadrature phase space rotating at ν_q (right panel), resonance fluorescence is revealed by the time oscillation (green) of the voltage V_{Re}, shifted by a constant value (blue).

in the Fresnel plane for three different drive amplitudes, with initial qubit states either in the ground $|g\rangle$ (purple line) or excited state $|e\rangle$ (orange line). As expected from Eq. (1), the measured amplitude is the sum of a time-independent offset proportional to the drive amplitude and of a fluorescence term oscillating at the Rabi frequency. With our choice of phase reference, it oscillates along the real quadrature only. The fluorescence signal $s_-(t) \propto V_{\mathrm{Re}}(t) - V_{\mathrm{Re}}^0$ can now be defined as the oscillating part of the real quadrature (Fig. 2b). A single proportionality factor is fixed for the whole set of measurements so that the average $\overline{s_-}(t)$ matches in amplitude the predicted value of $\langle\sigma_-(t)\rangle$, which is here a real number. Note that the finite bandwidth 1.6 MHz of the phase-preserving amplifier needs to be taken into account when calculating the fluorescence signal from the predicted time trace of $\langle\sigma_-\rangle$ (plain lines in Fig. 2c), resulting in a temporally deformed version of the theory, which matches well the measured $\overline{s_-}$ (Fig. 2b). In addition to the measurement of the fluorescence signal, a complementary probing of the qubit dynamics can be realized by the measurement of the qubit population $\langle\sigma_z\rangle$. The corresponding time trace taken in a separate measurement is shown in Fig.2c. It is obtained using the high-power readout technique [16, 17], which uses a final microwave tone at the bare cavity resonance frequency. As expected, initial preparation in ground $|g\rangle$ (purple line) or excited state $|e\rangle$ (orange line) lead to opposite modulations at the Rabi frequency $\nu_R = 1$ MHz. Note that the reduced contrast of the oscillations is due to a finite thermal population of the qubit, leading to $p_0 = 15.4\%$ in state $|g\rangle$ when preparing state $|e\rangle$ [15]. Thus, two non-commutating qubit operators can be probed using the fluorescence signal and the conventional qubit population measurement. While the latter is a single-shot, discrete measurement, s_- is a weak, continuous measurement whose strength can be characterized [18] by the measurement rate γ_{1b}, which is of the order of 0.1 % of the detector bandwidth.

According to Eq. (1), the observed fluorescence traces can be predicted by calculating the real part of the average value $\mathrm{Tr}\,[\rho(t)\sigma_-]$ of the lowering operator, where ρ is the density operator of the qubit. Its evolution can be predicted from the preparation $\rho(0) = (1-p_0)|e\rangle\langle e| + p_0|g\rangle\langle g|$ and using the master equation in the Lindblad form [19]

$$\frac{d\rho}{dt} = -\frac{i}{\hbar}\,[H,\rho] + \gamma_1\left(\sigma_-\rho\sigma_+ - \frac{1}{2}\,[\sigma_+\sigma_-\rho + \rho\sigma_+\sigma_-]\right). \tag{2}$$

The first term describes the Hamiltonian evolution of the qubit in presence of a drive, with $H = h\nu_q\sigma_z/2 + h\nu_R\sigma_y/2$. We use the standard Pauli operators $\sigma_z = |e\rangle\langle e| - |g\rangle\langle g|$, $\sigma_x = (\sigma_- + \sigma_+)$ and $\sigma_y = i\,(\sigma_- - \sigma_+)$. The second term takes into account relaxation with a rate $\gamma_1 = (16\ \mu\mathrm{s})^{-1}$, part of which is due to the spontaneous emission rate γ_{1b} introduced in Eq. (1). The excellent agreement between these predictions (lower half) and data (upper half) is shown in Fig. 2d, where the average fluorescence signal $\overline{s_-}$ is represented as a function of both time and Rabi frequency, for a qubit prepared at time 0 close to the excited state. The Rabi oscillations of the qubit are apparent both in time and drive amplitude. Here, relaxation only leads to a slight fading of the oscillation contrast since the duration $T = 2.5\ \mu$s of the experiment is much smaller than γ_1^{-1}.

Figure 2d represents the fluorescence signal averaged on a large set of experiments with identical initial state at time 0. Dually, one can perform the averaging on all experiments where the qubit is measured at time T in an identical final state, given by the outcome of σ_Z. One can ensure that there is no prior knowledge by preparing the qubit in the maximally entropic state, half experiments starting with the qubit in the ground state and half in the excited state. Such an averaging conditioned on the future only is shown in Fig. 2e for a qubit post-selected in the ground state at time T. Clearly, Fig. 2e is the time-reversed of Fig. 2d which reflects the duality between preparation and postselection.

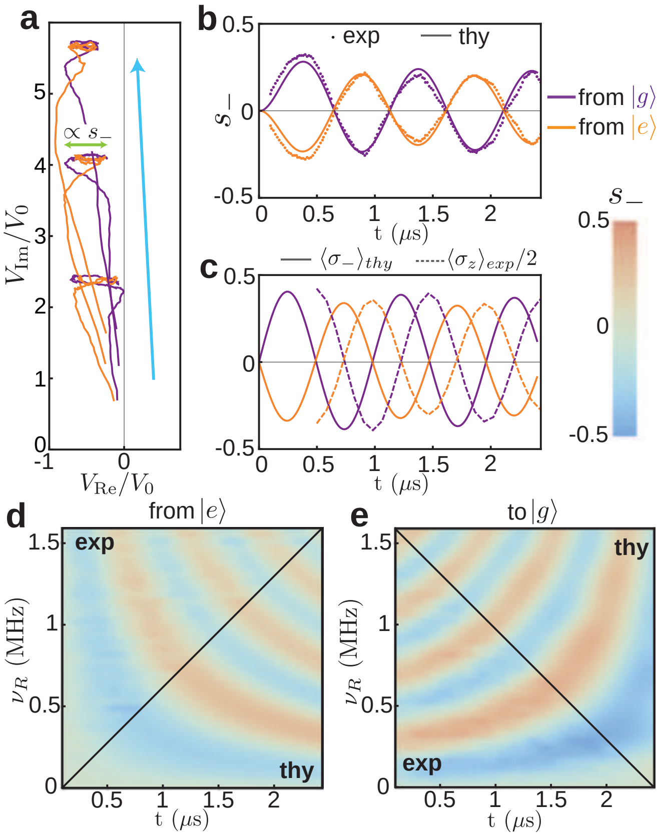

Figure 2: **Resonance fluorescence in time domain. a,** Average time traces of the heterodyned outgoing field on line b represented in the Fresnel plane $(V_{\rm Re}, V_{\rm Im})$, for driving amplitudes corresponding to $\nu_R = 0.6$ MHz, 1 MHz and 1.4 MHz (blue arrow represents increasing drive amplitudes). The unit of voltage V_0 corresponds to an average emitted photon rate equal to γ_{1b}. Purple (resp. orange) lines correspond to a qubit prepared in $|g\rangle$ (resp. $|e\rangle$) at $t = 0$. Each trace is the sum of a term proportional to the drive amplitude and an oscillating part in $V_{\rm Re}$ which corresponds to the resonance fluorescence. The finite bandwidth (1.6 MHz) of the detection setup deforms the time traces (finite rise time and diminished oscillation amplitude). **b,** Dots: Average fluorescence signal s_- as a function of time t for a Rabi frequency $\nu_R = 1$ MHz. Lines: corresponding predicted fluorescence signal filtered by detection setup. **c,** Dashed lines: measured values of $\langle\sigma_z\rangle$ for $\nu_R = 1$ MHz. Plain lines: predicted $\langle\sigma_-\rangle$ leading to plain lines in (b). **d,e,** Average value of the fluorescence signal s_- as a function of both time and Rabi frequency, for a qubit either prepared in $|e\rangle$ (d) or post-selected in $|g\rangle$ (e). Both measured and predicted averages of s_- are shown in separate regions. Absolute values remain well bellow 0.5, as expected for the measurement of $\mathrm{Re}\left[\langle\sigma_-\rangle\right] = \langle\sigma_x\rangle/2$.

The final measurement outcome used as a post-selection criterion can be modeled by a positive operator valued measure $E(T)$ [20]. For instance, when the measurement of σ_z indicates that the qubit is in the ground state, $E(T) = (1-p_T)|g\rangle\langle g| + p_T|e\rangle\langle e|$, where $p_T \ll 1$ takes into account the imperfection of the measurement. The post-selected average value of the lowering operator is then given at any time t before T by $\mathrm{Tr}\left[E(t)\sigma_-\right]/\mathrm{Tr}\left[E(t)\right]$ [5–7]. Here, we have used a time dependent post-selection operator $E(t)$, which obeys a similar equation to Eq. (2) valid for times $t \leq T$

$$\frac{dE}{dt} = -\frac{i}{\hbar}[H, E] - \gamma_1\left(\sigma_+ E\sigma_- - \frac{1}{2}\left[\sigma_+\sigma_- E + E\sigma_+\sigma_-\right]\right). \tag{3}$$

The corresponding prediction for the post-selected average value of s_- is in perfect agreement with the measured one as shown in Fig. 2e. Note that the slightly better contrast of the post-selected oscillations compared to the preselected ones is explained by a more efficient measurement than preparation ($p_0 > p_T$).

How are time traces of fluorescence modified when using knowledge of both past and future? The conditional average of the fluorescence signal is represented in Fig. 3 for both a preparation in excited state (as in Fig. 2d) and a postselection in ground state (as in Fig. 2e). This fluorescence signal, which probes the weak values $\langle\sigma_-\rangle_w$, is dramatically changed. Schematically, Fig. 3a exhibits interferences between the oscillations of Fig. 2d and of Fig. 2e, with the appearance of negative (blue) and positive (red) pockets. There are times t and Rabi frequencies ν_R in these pockets for which the weak values go beyond the conventional range of unconditional averages, set by $|\mathrm{Re}(\langle\sigma_-\rangle)| \leq 1/2$. In Fig. 3, plain lines represent the contours within which this boundary is violated. Quantitatively, the largest weak value we could obtain is 2.6 times larger than the unconditional average. This purely quantum effect, first predicted in 1988 [2] and observed already in quantum optics in 1991 [21], is a complementary evidence to the irrelevancy of macro realism [22]. In superconducting circuits, out of bound weak values have already been demonstrated in connection with the Leggett-Garg inequalities on the autocorrelation spectrum of $\sigma_z(t)$ [11] and for discrete weak measurements performed by another artificial atom [12].

Special features develop when past and future information disagree, which is for Rabi frequencies such that the qubit rotates by an even amount of π in a time T (Fig. 3). There, the weak values go to zero but a small shift in Rabi frequency results in a dramatic change of the signal as evidenced in Fig. 3b, where the conditioned average of the fluorescence signal is shown as dots as a function of ν_R at times $t = 0.99$ μs and $t = 1.44$ μs. At the sign change, the slope of the weak value is much stiffer than the one of the unconditional signal (dashed line), which is characteristic of the amplifying abilities of weak values [23, 24]. This curve was the most sensitive way to determine the measurement fidelity of the qubit population at time T in our experiment. Note that it does not mean that other post-processing techniques than the conditional average would not result in an even better parameter estimation [25–28].

The conditional average of fluorescence signals can be quantitatively understood using the same formalism as described above. The weak value for σ_- at any time t can indeed be obtained from the operators $\rho(t)$ from the

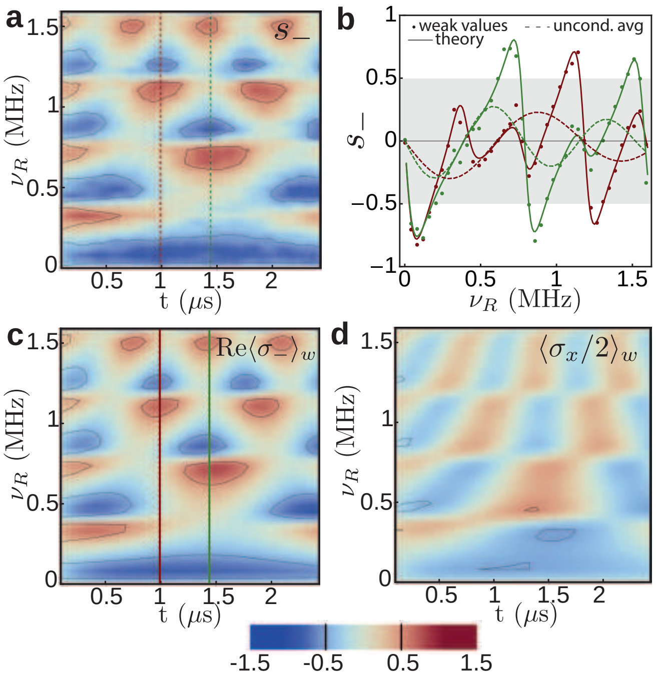

Figure 3: **Interferences between past and future states.** **a,** Average value of the measured fluorescence signal s_- as a function of both time and Rabi frequency, for a qubit prepared in $|e\rangle$ and post-selected in $|g\rangle$. Plain lines surround regions with weak values beyond the range allowed by macro realism. **b,** Dots: cuts of **a** as a function of ν_R for times $t = 0.99$ μs (green) and $t = 1.44$ μs (red). Plain lines: prediction for the same curves using Eq (4). Dashed lines: cuts of Fig. 2d at the same times. The gray region delimits the range of possible unconditional average values, like the contours in (a). **c,** Theoretical counterpart of **a** assuming that the average of s_- is a measure of $\mathrm{Re}(\langle\sigma_-\rangle_w)$ and using Eq. 4. **d,** Theoretical counterpart of **a** assuming that the average of s_- is a measure of $\langle\mathrm{Re}\sigma_-\rangle_w)$.

past and $E(t)$ from the future, and is given by [5–7].

$$\langle\sigma_-\rangle_w = \mathrm{Tr}(\tilde{\rho}\sigma_-), \text{ where } \tilde{\rho}(t) = \frac{\rho(t)E(t)}{\mathrm{Tr}(\rho(t)E(t))}. \quad (4)$$

The experiment offers a quantitative test of this simple expression, since the post-selected fluorescence signal is given by $\mathrm{Re}(\langle\sigma_-\rangle_w)$. As can be seen on Fig. 3b, the resulting prediction (plain lines) agrees well with the data (dots). The agreement is good for all measurements as can be seen between Figs. 3a and 3c where both prediction and measurements are compared as a function of time t and Rabi frequency ν_R. The predicted contours surrounding the regions where macro realism is violated are represented as plain lines and they indeed match well their experimental counterpart. The agreement was excellent for any conditions we considered on preparation and post-selection [15].

Interestingly, the operator σ_- probed by the conditional averaged s_- is not an observable as it is not hermitian. This illustrates the ability of conditional averages of weak measurements to probe complex quantities [29]. Here, the measured observable leading to s_- is the field quadrature $\mathrm{Re}(b_{out}) = (b_{out}^\dagger + b_{out})/2$. For averages with either pre-selection or post-selection only, Eq. (1) leads to $\overline{s_-} = \mathrm{Re}\langle\sigma_-\rangle$ or $\overline{s_-} = \langle\mathrm{Re}\sigma_-\rangle = \langle\sigma_x/2\rangle$, which are formally identical. This is not the case anymore for pre and post-selected measurements for which $\mathrm{Re}\langle\sigma_-\rangle_w$ and $\langle\sigma_x/2\rangle_w$ differ and indeed give very different predictions as can be seen in Figs 3c and 3d. It is clear that the experiment matches only the prediction associated with $\mathrm{Re}\langle\sigma_-\rangle_w$, which cannot be interpreted as the weak value of the observable $\sigma_x/2$.

In conclusion, we demonstrated that detecting resonance fluorescence radiated by a superconducting qubit out of a cavity corresponds to a weak continuous monitoring of the σ_- operator of the qubit. Using conditional averaging on the fluorescence signal depending on the measured final state of the qubit, we observed interferences between Rabi oscillations associated to past and future states. The experiment offers a quantitative demonstration of the accuracy of recent theoretical works [5–7] able to predict the conditional average of continuous recording in open quantum systems. Fluorescence tracking illustrates several key aspects of weak values: violation of macro realism, improvement of parameter estimation and non-hermitian operator measurement. Besides, by recording efficiently the fluorescence signal, one should be able to fully estimate the qubit trajectory. It may be a way to correct for relaxation in real time by feedback [30–33] as long as decoherence is limited by emission into a transmission line.

Acknowledgments

We thank Michel Devoret, Vladimir Manucharyan, Mazyar Mirrahimi, Pierre Rouchon, Benoit Douçot, Klaus Mølmer, Brian Julsgaard, Pascal Degiovanni, Daniel Valente and Patrice Bertet for enlightening discussions. Nanofabrication has been made within the consortium Salle Blanche Paris Centre. This work was supported by the ANR contracts ANR-12-JCJC-TIQS and ANR-13-JCJC-INCAL. LB acknowledges support from Direction Générale de l'Armement.

---

[1] Y. Aharonov, P. Bergmann and J. Lebowitz. Time Symmetry in the Quantum Process of Measurement. Physical Review **134**, B1410–B1416 (1964).

[2] Y. Aharonov, D. Albert and L. Vaidman. How the result of a measurement of a component of the spin of a spin-1/2 particle can turn out to be 100. Physical Review Letters

60, 1351–1354 (1988).

[3] Y. Aharonov, S. Popescu and J. Tollaksen. A time-symmetric formulation of quantum mechanics. Physics Today **63**, 27 (2010).

[4] J. Dressel, M. Malik, F. M. Miatto, A. N. Jordan and R. W. Boyd. Understanding Quantum Weak Values: Basics and Applications. arxiv **1305.7154** (2013).

[5] H. Wiseman. Weak values, quantum trajectories, and the cavity-QED experiment on wave-particle correlation. Physical Review A **65**, 032111 (2002).

[6] M. Tsang. Optimal waveform estimation for classical and quantum systems via time-symmetric smoothing. Physical Review A **80**, 033840 (2009).

[7] S. Gammelmark, B. Julsgaard and K. Mølmer. Past Quantum States of a Monitored System. Physical Review Letters **111**, 160401 (2013).

[8] B. Mollow. Power Spectrum of Light Scattered by Two-Level Systems. Physical Review **188**, 1969–1975 (1969).

[9] O. Astafiev, A. M. Zagoskin, A. A. Abdumalikov, Y. A. Pashkin, T. Yamamoto, K. Inomata, Y. Nakamura and J. S. Tsai. Resonance fluorescence of a single artificial atom. Science (New York, N.Y.) **327**, 840–3 (2010).

[10] A. A. Houck, D. I. Schuster, J. M. Gambetta, J. A. Schreier, B. R. Johnson, J. M. Chow, L. Frunzio, J. Majer, M. H. Devoret, S. M. Girvin and R. J. Schoelkopf. Generating single microwave photons in a circuit. Nature **449**, 328–331 (2007).

[11] A. Palacios-laloy, F. Mallet, F. Nguyen, P. Bertet, D. Vion, D. Esteve and A. N. Korotkov. Experimental violation of a BellÕs inequality in time with weak measurement. Nature Physics **6**, 442–447 (2010).

[12] J. P. Groen, D. Ristè, L. Tornberg, J. Cramer, P. C. de Groot, T. Picot, G. Johansson and L. DiCarlo. Partial-Measurement Backaction and Nonclassical Weak Values in a Superconducting Circuit. Physical Review Letters **111**, 090506 (2013).

[13] Paik, D. Schuster, Bishop, G. Kirchmair, G. Catelani, Sears, Johnson, Reagor, Frunzio, Glazman, Girvin, Devoret and Schoelkopf. Observation of High Coherence in Josephson Junction Qubits Measured in a Three-Dimensional Circuit QED Architecture. Physical Review Letters **107**, 240501 (2011).

[14] D. Valente, S. Portolan, G. Nogues, J. P. Poizat, M. Richard, J. M. Gérard, M. F. Santos and a. Auffèves. Monitoring stimulated emission at the single-photon level in one-dimensional atoms. Physical Review A **85**, 023811 (2012).

[15] Supplementary information.

[16] M. D. Reed, L. DiCarlo, B. R. Johnson, L. Sun, D. I. Schuster, L. Frunzio and R. J. Schoelkopf. High-Fidelity Readout in Circuit Quantum Electrodynamics Using the Jaynes-Cummings Nonlinearity. Physical Review Letters **105**, 173601 (2010).

[17] L. S. Bishop, E. Ginossar and S. M. Girvin. Response of the Strongly Driven Jaynes-Cummings Oscillator. Physical Review Letters **105**, 100505 (2010).

[18] A. A. Clerk, M. H. Devoret, S. M. Girvin, F. Marquardt and R. J. Schoelkopf. Introduction to quantum noise, measurement, and amplification. Reviews of Modern Physics **82**, 1155–1208 (2010).

[19] G. Lindblad. On the generators of quantum dynamical semigroups. Communications in Mathematical Physics **48**, 119–130 (1976).

[20] S. Haroche and J. Raimond. Exploring the Quantum: Atoms, Cavities, and Photons. Oxford Graduated Text (2006).

[21] N. Ritchie, J. Story and R. Hulet. Realization of a measurement of a weak value. Physical Review Letters **66**, 1107–1110 (1991).

[22] N. Williams and A. Jordan. Weak Values and the Leggett-Garg Inequality in Solid-State Qubits. Physical Review Letters **100**, 026804 (2008).

[23] O. Hosten and P. Kwiat. Observation of the spin hall effect of light via weak measurements. Science (New York, N.Y.) **319**, 787–90 (2008).

[24] P. Dixon, D. Starling, A. Jordan and J. Howell. Ultrasensitive Beam Deflection Measurement via Interferometric Weak Value Amplification. Physical Review Letters **102**, 173601 (2009).

[25] G. Knee, G. Briggs, S. Benjamin and E. Gauger. Quantum sensors based on weak-value amplification cannot overcome decoherence. Physical Review A **87**, 012115 (2013).

[26] C. Ferrie and J. Combes. Weak Value Amplification is Suboptimal for Estimation and Detection. Physical Review Letters **112**, 040406 (2014).

[27] S. Tanaka and N. Yamamoto. Information amplification via postselection: A parameter-estimation perspective. Physical Review A **88**, 042116 (2013).

[28] G. C. Knee and E. M. Gauger. When amplification with weak values fails to suppress technical noise arxiv **1306.6321** (2013).

[29] J. S. Lundeen, B. Sutherland, A. Patel, C. Stewart and C. Bamber. Direct measurement of the quantum wavefunction. Nature **474**, 188–91 (2011).

[30] R. Vijay, C. Macklin, D. H. Slichter, S. J. Weber, K. W. Murch, R. Naik, A. N. Korotkov and I. Siddiqi. Stabilizing Rabi oscillations in a superconducting qubit using quantum feedback. Nature **490**, 77–80 (2012).

[31] D. Ristè, C. Bultink, K. Lehnert and L. Dicarlo. Feedback Control of a Solid-State Qubit Using High-Fidelity Projective Measurement. Physical Review Letters **109**, 240502 (2012).

[32] P. Campagne-Ibarcq, E. Flurin, N. Roch, D. Darson, P. Morfin, M. Mirrahimi, M. H. Devoret, F. Mallet and B. Huard. Persistent Control of a Superconducting Qubit by Stroboscopic Measurement Feedback. Physical Review X **3**, 021008 (2013).

[33] G. de Lange, D. Ristè, M.J. Tiggelman, C. Eichler, L. Tornberg, G. Johansson, A. Wallraff, R.N. Schouten and L. Dicarlo. Reversing Quantum Trajectories with Analog Feedback. Physical Review Letters **112**, 080501 (2014).